國立臺灣大學電機資訊學院光電工程學研究所

博士論文

Graduate Institute of Photonics and Optoelectronics

College of Electrical Engineering and Computer Science

National Taiwan University

Doctoral Dissertation

超寬頻掃頻摻鈦藍寶石晶體光纖雷射研究

Study of ultra-broadband Ti:sapphire crystal fiber based wavelength-swept laser

林裕展

Yu-Chan Lin

指導教授：黃升龍 博士

Advisor: Sheng-Lung Huang, Ph.D.

中華民國 111 年 8 月

August 2022

doi:10.6342/NTU202203086

國立臺灣大學博士學位論文
口試委員會審定書

超寬頻掃頻摻鈦藍寶石晶體光纖雷射研究
Study of ultra-broadband Ti:sapphire crystal fiber based wavelength-swept laser

本論文係林裕展君（學號 D98941007）在國立臺灣大學光電工程學研究所完成之博士學位論文，於民國 111 年 8 月 31 日承下列考試委員審查通過及口試及格，特此證明

口試委員：

（指導教授）

所　長

誌謝

首先，非常感謝我的指導教授黃升龍博士這五年來的指導與陪伴，如果沒有老師的陪伴與支持，我想我很難堅持到今天，第一次寫信給老師已經是八年前了，感謝老師當年沒有任何猶豫就收我當學生，給了當時充滿迷惘的我很大的安全感，同時也願意給我時間處理家裡的事物以及克服心理的障礙，才讓五年前的我有勇氣回來重新完成我的博士學位，這五年來老師對於實驗的態度就是實事求是，沒有任何的妥協，在透過每一次與老師的討論，讓我慢慢意識到自身的問題，藉由這樣的引導讓我成長非常多，我的研究方向、期刊論文、博士論文以及論文口試投影片都在老師的引導下變得更加的完善，過程中我也常常因為不瞭解而灰心，但老師總是有耐心的等我自己思考並適時的引導，以及陪伴我走到了每一個目標終點，再回頭看就會知道當初自己有多麼地不成熟，同時也很開心自己成長了，在這樣的扎實訓練下，我才能完成目前世界上解析度最好的掃頻雷射，老師的恩情學生會一輩子銘記於心。

感謝延垠在我剛進實驗室時給予我的鼓勵與支持，感謝祐維教我認識實驗室的晶體光纖及架設雷射系統，感謝昱彤、庭瑋、游鈐陪伴及解答我對於 OCT 的疑問，還有跟昱彤在會議結束時一起游泳運動的時光，感謝冠鳴跟我解答 AI 的問題，以及陪伴我一起唱歌跟運動。感謝奕勳把鍍膜機研究的這麼透徹，並不藏私的教我，還有平時一起討論雷射的研究、出遊、泡咖啡以及品嚐麥芽發酵的風味。感謝柏彥跟家沛陪伴一起跑跑程式舒壓，感謝安荷平日裡跟我分享美食資訊及互相支援咖啡，並總在我忙碌時適時的簡訊關心，感謝淑雯適時的鼓勵跟支持、畢業後還分享台南美食及好聽的歌曲。感謝修羽陪伴我唱歌、打球、延續 FDML 的研究，感謝

doi:10.6342/NTU202203086

雅鈞的信任、努力以及幫忙準備口試餐點，感謝豫萱帶著非常好的研究精神學習，並延續掃頻雷射的研究，感謝以佳幫忙準備口試餐點，感謝柏辰努力維護好 OCT 系統及陪伴最後的口試。感謝雅婷姐在實驗室帳務上的協助，以及平日陪伴一起喝咖啡的時光，感謝群玲在晶體光纖製備上的幫忙。還有很多在這過程中遇到的學弟妹以及過客，也祝福你們一切順心平安。

特別感謝孝祖這一年多來的信任、支持、陪伴，感謝你這麼信任我這個學長，特別感謝好友 Manu，在平日的互動裡，讓我有機會練習我的英文口說，並且不吝修正我的英文及教我西班牙文，且只要我需要討論一定撥空給我，即使我們現在時差 7 小時，相距 13244 公里遠，也排除萬難來幫我，Gracias mi amigo!要特別感謝騰毅，在我剛進入實驗室時不藏私地教會我如何長晶以及晶體光纖的知識，也總在我需要的時候排出時間來幫我，只要我有需要他一定出現相挺，博士論文也是透過不斷跟騰毅討論，才讓我的思路變得如此清晰，最終完成我自己滿意的論文，有太多的感謝沒辦法完全用文字表達，想跟騰毅說未來你的身旁也一定有我陪伴。

最後，要非常感謝我的老婆懷萱，陪伴我走過博士階段，感謝妳這些年的支持及陪伴，以及把家裡、穎達跟穎政照顧的無微不至，讓我能全力去追逐我的夢想，沒有妳就沒有今天的我，這些年真的辛苦妳了，愛妳。

doi:10.6342/NTU202203086

中文摘要

掃頻雷射做為光源已經被廣泛的應用在光學同調斷層掃描術上，由於其掃頻速度極限跟增益介質的輻射生命期及雷射腔體的往返時間有關，因此，多數研究團隊利用輻射生命期為奈秒等級的半導體光放大器為掃頻雷射的增益介質。但由於半導體光放大器的波長多為紅外光區，且可調帶寬為 100 奈米附近，其所提供的縱向解析度很難達到細胞級解析度。本論文使用可調波長從 650 奈米到 1100 奈米的摻鈦藍寶石晶體光纖為增益介質，且摻鈦藍寶石的發射光譜處於低組織散射及水吸收較小的區域，加上其放光頻譜近似高斯，因此非常適用於光學同調斷層掃描術。由於晶體光纖結構擁有高度的表面積對體積的比例，可以有效提高散熱能力，憑藉此摻鈦藍寶石晶體光纖的低信號傳播損耗及高散熱能力，本論文成功實現掃頻重複率 1200 赫茲且掃頻帶寬為 250 奈米的超寬頻掃頻雷射。並藉由分析掃頻雷射的鬆弛震盪，可以計算出雷射腔體內的損耗，其數值與理論模擬結果符合。此掃描雷射可以產生 0.018 奈米的瞬時線寬，其對應當能量降為一半時的同調掃描深度為 7 毫米。如將這掃頻雷射使用於掃頻式光學同調斷層掃描時，將可以實現 1.8 微米的縱向解析度。然而，由於本實驗所使用的增益介質為多橫模的摻鈦藍寶石晶體光纖，因此所實現的掃頻雷射輸出模態為多橫模雷射，此特性將嚴重地影響其應用於各種系統的可行性，為此將單模光纖導入雷射腔內以消除高階橫模，本論文成功地實現單橫模輸出的超寬頻掃頻雷射。

關鍵字：掃頻雷射、摻鈦藍寶石晶體光纖、單模雷射輸出、光學同調斷層掃描術

doi:10.6342/NTU202203086

Abstract

Wavelength-swept lasers (WSLs) have been widely used as light source in optical coherence tomography (OCT). The wavelength tuning speed is mainly limited by the radiative lifetime of the gain media and the cavity round-trip time. Therefore, most researchers use the semiconductor optical amplifier (SOA) as the gain medium of WSL with nanosecond radiative lifetime. The gain bandwidth of a typical SOA lies around 100 nm in the infrared band, its axial resolution is very difficult to achieve cellular scale. Therefore, this dissertation uses Ti:sapphire crystal fiber (CF) with tuning ranges from 650 to 1100 nm as the gain medium. Ti:sapphire CF is very suitable for OCT because its emission spectrum lies in a region of low tissue scattering and low water absorption, as well as approximately Gaussian profile. Since the crystal fiber structure has a high surface area-to-volume ratio, it can effectively improve the heat dissipation capacity. With the low signal propagation loss and high heat dissipation of the CF, the WSL has a tuning bandwidth of 250 nm at a repetition rate of 1200 Hz. The steady-state and pulsed dynamics of the WSL were analyzed, the experimental result is fitted with the theoretical simulation. The 0.018-nm instantaneous linewidth corresponds to a 3-dB coherence roll-off of 7 mm. When using the laser for swept-source OCT, an estimated axial resolution of 1.8 μm can be achieved. However, the gain medium used in this experiment is a multi-transverse mode CF, the output mode of the WSL is also a multi-transverse mode. This characteristic will seriously affect the feasibility of its application. Therefore, the single-mode fiber is introduced into the laser cavity to eliminate the high-order transverse mode, the ultra-broadband WSL with single-transverse mode output is successfully realized.

Keywords: wavelength-swept laser, Ti:sapphire crystal fiber, single-mode output laser, optical coherence tomography

doi:10.6342/NTU202203086

Table of Content

doi:10.6342/NTU202203086

doi:10.6342/NTU202203086

doi:10.6342/NTU202203086

List of figures

doi:10.6342/NTU202203086

doi:10.6342/NTU202203086

doi:10.6342/NTU202203086

doi:10.6342/NTU202203086

doi:10.6342/NTU202203086

List of tables

doi:10.6342/NTU202203086

Chapter 1

Introduction

Wavelength-swept lasers (WSLs) have been widely used for sensing, spectroscopy [1], and particularly in optical coherence tomography (OCT) [2]. Various wavelength sweeping techniques and configurations have accomplished [3-4]. The wavelength tuning speed is mainly limited by the build-up time of the laser gain media and the cavity roundtrip time in a direct sweeping configuration [5]. Therefore, most researchers use the semiconductor optical amplifier (SOA) as the gain medium with high gain and nanosecond radiative lifetime. The gain bandwidth of a typical SOA lies around 100 nm [6]. Early studies have demonstrated tuning speeds from 100 Hz to several MHz with an OCT axial resolution of larger than 5.3 μm with a wavelength of 1060 nm to 1300 nm [7–10]. To increase the gain bandwidth, a parallel configuration of SOA with 228-nm bandwidth was implemented at the wavelength of 1060 nm [11], as shown in Fig. 1.1. However, the configuration inevitably leads to an intracavity Mach-Zehnder-like interferometer structure that would generate loss and excess noise via the spectral overlap.

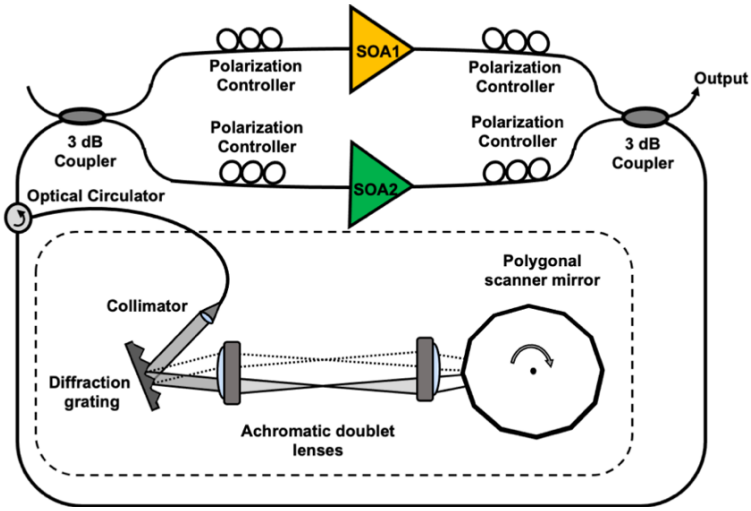

Fig. 1.1. The experimental setup of WSL with dual SOAs [11].

doi:10.6342/NTU202203086

The wavelength-swept lasers with different gain media are summarized in Table 1.1. In Table 1.1, the most widely employed gain medium for wavelength-swept lasers is SOA. However, the fluorescence band of SOA is mostly in the infrared band. The shorter central wavelength and the wider tuning bandwidth, it offers better axial OCT resolution. Application-wise, ultrahigh-resolution OCT with cellular imaging capability is advancing rapidly. Ti:sapphire is one of the most commonly used materials in broadband fluorescence and lasers, as shown in Fig. 1.2 [12]. Ti:sapphire lasers emit in the visible light and near-infrared light range with 400-nm bandwidth.

Table 1.1. Summary of wavelength-swept lasers with different gain media.

λ_c *(nm)*	$\Delta\lambda$ *(nm)*	f_{sweep} *(kHz)*	*Gain medium [ref.]*
532	15	342	SOA [13]
850	80	16	SOA [14]
1040	131	86	Dual SOA [15]
1057	70	600	MEMS-VCSELs [16]
1060	40	1150	VCSELs [17]
1060	100	200	SOA [18]
1060	120	20	SOA [19]
1060	228	1.8	Dual SOA [11]
1310	100	370	SOA [20]
1310	100	200	SOA [10]
1310	120	3520	SOA [21]
1310	125	240	SOA [22]
1310	140	100	SOA [23]
1310	170	20	SOA [19]
1315	160	100	SOA [24]
1550	58	11500	Er-doped fiber [25]
1550	102	44500	Er-doped fiber [26]
1550	160	183600	Er-doped fiber [27]
1550	115	110	SOA [28]
1550	120	3520	SOA [21]
2000	30	19000	Tm-doped fiber [29]
3070	360	1	Dy-doped fiber [30]

doi:10.6342/NTU202203086

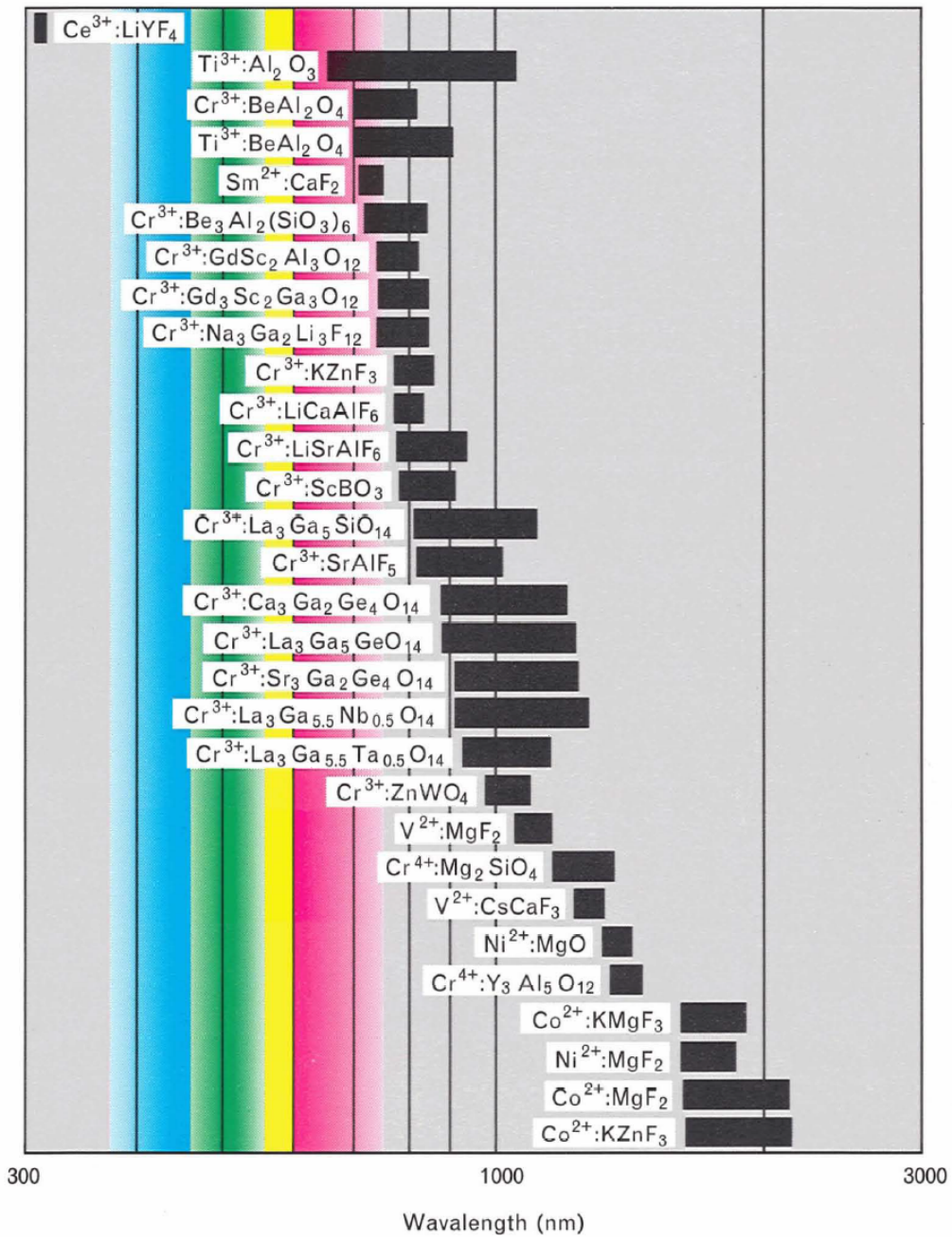

Fig. 1.2. Overview of broadband laser materials [12].

Ti:sapphire laser is very suitable for various biological measurements because its emission spectrum lies in a region of low tissue scattering and low water absorption [31], as shown in Fig. 1.3. In previous reports, a resolution of ~1 μm with a time-domain OCT system [32] and ~2 μm with a spectral-domain OCT (SD-OCT) [33] have been demonstrated by utilizing Ti:sapphire as the gain medium. The narrow instantaneous

doi:10.6342/NTU202203086

tissue penetration when compared with the SD-OCT.

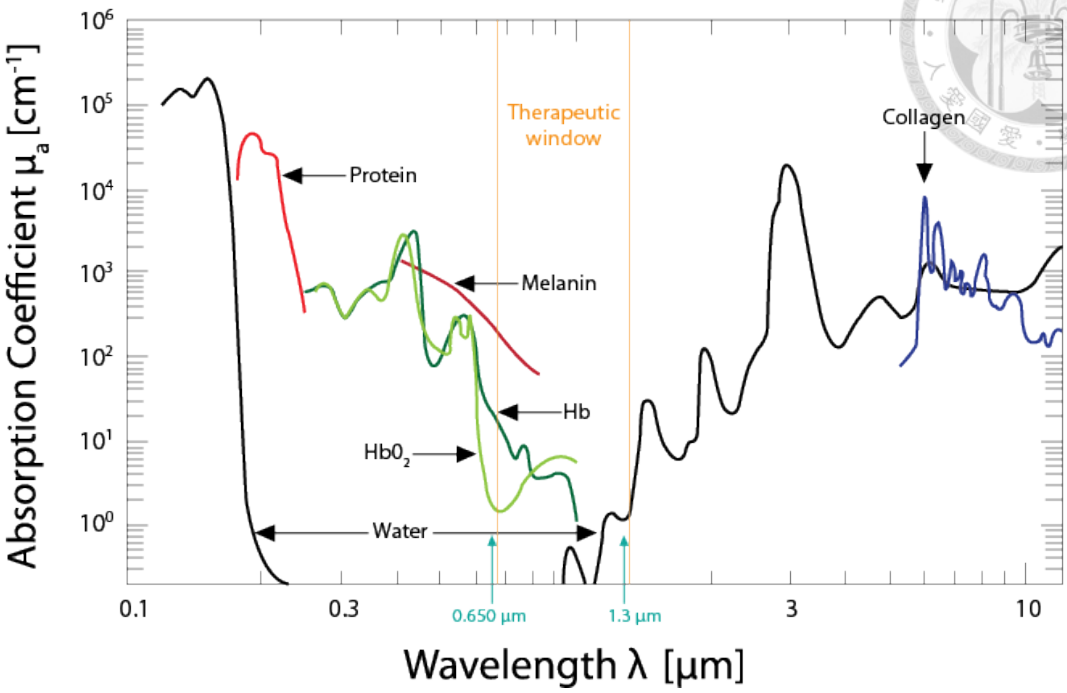

Fig. 1.3. Absorption spectra of several tissue molecules and aortic tissue [31].

WSLs with an axial resolution of larger than 10 µm have been demonstrated by using Ti:sapphire bulk crystal [34-35]. The low axial resolution is because the gain response time of bulk Ti:sapphire is unable to keep up with the sweeping wavelength for broadband emission. Though higher doping concentrations can raise the gain of bulk Ti:sapphire, heat dissipation becomes a challenge with high doping concentration. Ti:sapphire single-crystalline fiber (CF) grown by the laser-heated pedestal growth (LHPG) method significantly improves thermal dissipation and pump interaction length [36-37]. Furthermore, a Ti:sapphire crystal fiber waveguide with a propagation loss of 0.045 dB/cm was achieved to allow a low doping concentration [38]. The continuous tunability of the Ti:sapphie CF laser on a 180-nm wide wavelength range was demonstrated in 2019 [39]. In 2022, our group successfully demonstrated the ultra-broadband WSL by using Ti:sapphire CF [40]. Table 1.2 summarizes the wavelength-swept lasers by using the different structures of Ti:sapphire crystal as the gain medium.

doi:10.6342/NTU202203086

Table 1.2. Summary of wavelength-swept Ti:sapphire lasers.

Author	Year	Structure	λc (nm)	Tuning rate (Hz)	Bandwidth (nm)
S. Wada *et al.* [34]	1996	Bulk crystal	798	10	110 (743~853)
V. M. Kodach *et al.* [35]	2008	Bulk crystal	800	11000	10 (795~805)
Y.C. Lin *et al.* [40]	2022	Crystal fiber	808	1200	250 (683~933)

It should be noted that the relatively low sweeping frequency of this work may not be an issue for high-speed 3D image acquisition when the WSL is integrated with the FF-OCT configuration, as shown in Fig. 1.4. Several time-domain FF-OCT approaches have shown effective for early pre-cancer diagnosis of normal and abnormal cells [41–45]. The scanning speed is limited by the piezoelectric transducer movement. Using WSL can dramatically improve cross-sectional imaging speeds and detection sensitivities [46–48]. When the broadly swept Ti:sapphire laser is integrated with the full-field OCT configuration, high imaging speed and high resolution could be realized to meet the clinical needs of *in vivo* cellular resolution imaging on cancer diagnosis.

doi:10.6342/NTU202203086

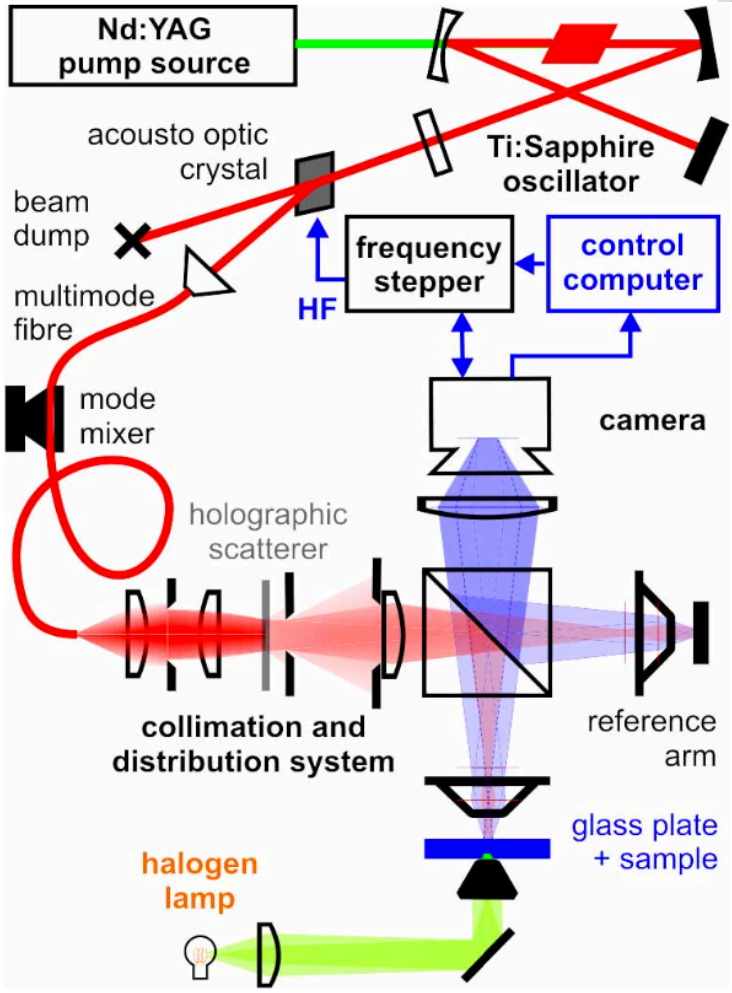

Fig. 1.4. Schematic drawing of the swept-source full-field setup [46].

The dissertation contains four main chapters. Chapter 2 presents the characterizations of glass-clad Ti:sapphire crystal fiber. The properties and numerical model of Ti:sapphire crystal were introduced first.

Chapter 3 describes the fabrication processes of glass-clad Ti:sapphire CF. The fabrication process includes single CF growth, furnace annealing, and glass cladding. The process of LHPG system for single CF growth is introduced first. The furnace annealing process was used for reducing the infrared absorption and enhancing the optical efficiency of the Ti:sapphire single CFs. The processes and results of glass-clad CF were described. The optical properties, propagation loss, refractive index, and fluorescence lifetime were

doi:10.6342/NTU202203086

measured and analyzed. The lowest propagation loss in Ti:sapphire waveguides was measured.

In chapter 4, the ultra-broadband wavelength-swept laser (WSL) was generated using glass-clad Ti:sapphire crystal fiber as the gain media. With the low signal propagation loss of the crystal fiber, the swept laser has a tuning bandwidth of 250 nm at a repetition rate of 1200 Hz. The steady-state and pulsed dynamics of the WSL were analyzed. The 0.018-nm instantaneous linewidth corresponds to a 3-dB coherence roll-off of 7 mm. When using the laser for swept-source optical coherence tomography, an estimated axial resolution of 1.8 μm can be achieved.

Chapter 5 analyzes the transverse modes and longitudinal modes of the WSL. By inserting a single-mode fiber into laser cavity, single-transverse mode WSL was demonstrated.

doi:10.6342/NTU202203086

Chapter 2

Characterizations and Modeling of Glass-clad Ti:sapphire Crystal Fiber

2.1 Fundamentals of Ti:sapphire Crystal

Sapphire (α-Al_2O_3) is a single crystal with a hexagonal (rhombohedral) crystal structure, which belongs to the ditrigonal-scalenohedral class of the trigonal symmetry D^6_{3d} – $R\bar{3}C(L_33L_23PC)$ [50]. A Ti^{3+} ion substitutes for an Al^{3+} ion at the octahedron center. The crystal structure of Ti:Al_2O_3 is shown in Fig. 2.1. The lattice constants of the sapphire are a = 4.758 Å, c = 12.991 Å, $\alpha = 90°$, $\beta = 90°$, and $\gamma = 120°$. The Ti^{3+} ions are located between two oxygen planes, displaced along the positive c axis from the midway position of the two planes. The octahedron surrounding the Ti^{3+} ion shows trigonal symmetry. The crystal structure of α-Al_2O_3 is drawn by CaRIne Crystallography software in Fig. 2.2 [51]. In the direction of the c-axis, the three distances Al–O is equal to 1.97 Å, and the other three distances are 1.87 Å. The Al–Al, and O–O spacings are 2.65 Å and 2.52–2.87 Å, respectively. The Ti^{3+} ions are located between two oxygen planes, displaced along the positive c-axis from the two planes midway position. The octahedron surrounding the Ti^{3+} ion shows trigonal symmetry. The ordinary and extraordinary refractive indices of sapphire crystal with different wavelengths [3] are shown in Fig. 2.3.

doi:10.6342/NTU202203086

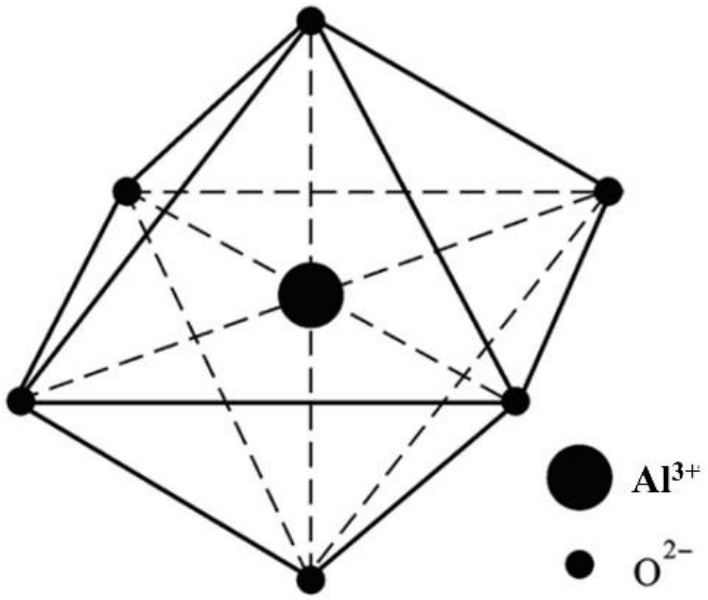

Fig. 2.1. Octahedron structure of a Ti:Al_2O_3 crystal unit cell. A Ti^{3+} ion substitutes for an Al^{3+} ion at the center.

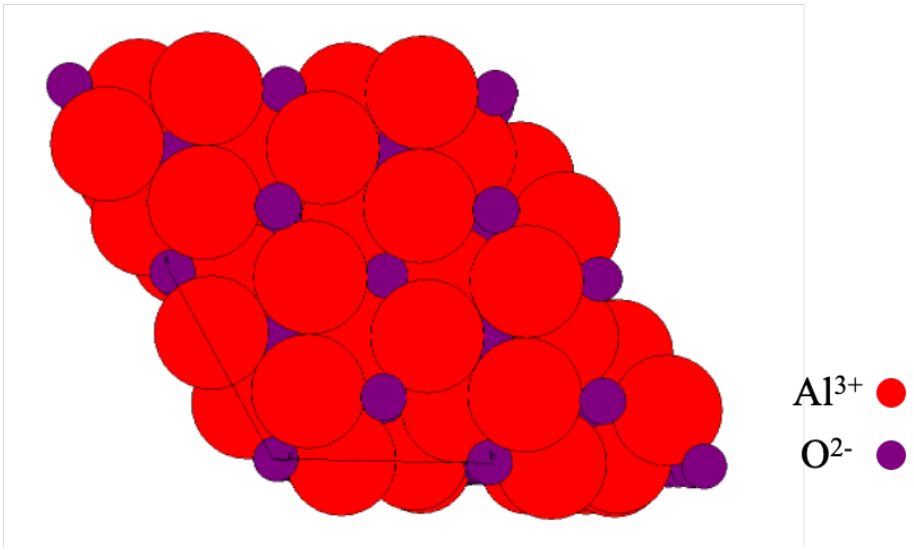

Fig. 2.2. Schematic of the arrangement of Al^{3+} between two layers of O^{2-} in the basal plan [51].

doi:10.6342/NTU202203086

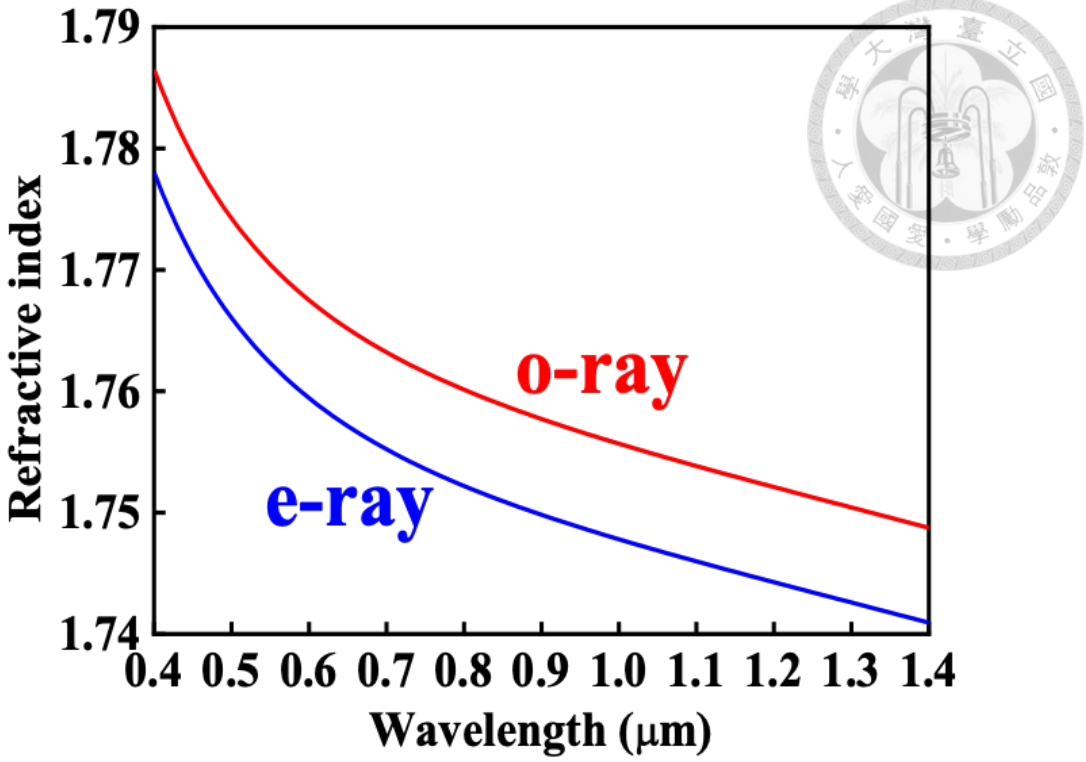

Fig. 2.3. Dispersion of α-Al_2O_3 crystal. The e-ray and o-ray are respectively defined for the polarization are parallel and perpendicular to the c-axis of the Al_2O_3 crystal [52].

Titanium belongs to the transition metal group. The electronic configuration of Ti is $1s^2 2s^2 2p^6 3s^2 3p^6 3d^2 4s^2$. There are two possible valence states of the titanium ions in Al_2O_3 crystal: trivalent (Ti^{3+}) and quadrivalent (Ti^{4+}). The Ti^{4+} ion has exactly the argon closed shell configuration. The Ti^{3+} ion has a single 3d electron outside the argon core. Ti^{4+} ions can only consume pump light but cannot generate light emission. The near-infrared emissions are generated from Ti^{3+} ions. The energy level diagram of Ti:Al_2O_3 crystal is shown in Fig. 2.4. The ^2D state of the free ion is split in the octahedron crystal field into a $^2T_2$ ground state and a ^2E excited state with a separation of 10 Dq (19,000

doi:10.6342/NTU202203086

cm^{-1}). The $^2T_2$ ground state is split into $^2A_1$ and ^2E in the trigonal symmetry. Spin-orbit interaction splits the ^2E_g state into $E_{1/2}$ and $E_{3/2}$ states. The Jahn-Teller effect removes the degeneracy of the excited state with a separation of 1850 cm^{-1}, which is the origin of the dual-peak pump absorption in the blue-green band. The energy levels of the Ti^{3+} ions have a strong coupling to the vibrations, which are broadened and called the vibrionic bands. Ti^{3+}:sapphire crystals have a four-level system effectively without unwanted excited-state absorptions, as shown in Fig. 2.5 [53].

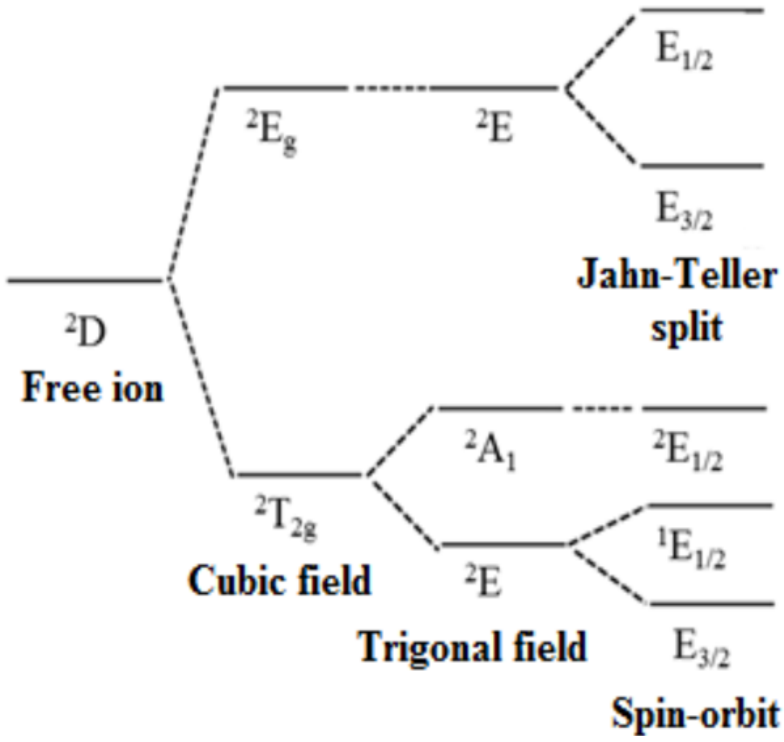

Fig. 2.4. Energy level diagram of Ti:Al_2O_3 crystal. Influence of the crystal field on the d-orbit electronic levels of the Ti^{3+} ion in sapphire crystal [54].

doi:10.6342/NTU202203086

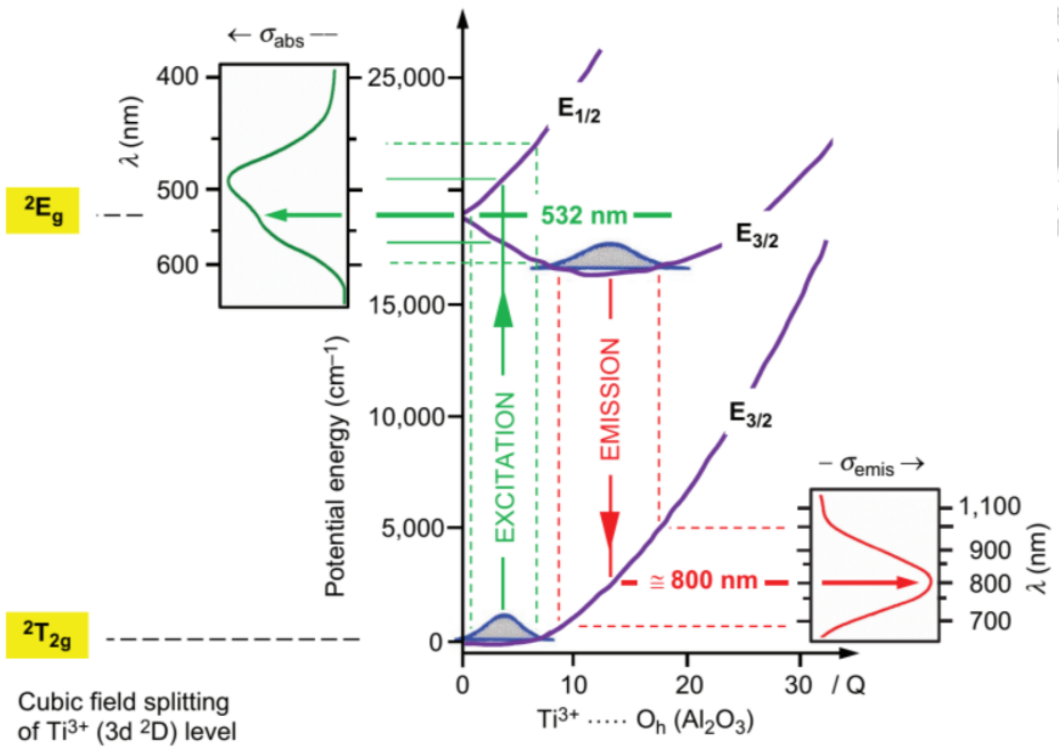

Fig. 2.5. Simplified energy level diagram [53].

The two-peak absorption is due to the Jahn-Teller splitting of the ^2E excited state. The Ti:Al_2O_3 lasers were usually pumped by the multiline Ar lasers in the past. Now they are pumped mainly by the compact and efficient frequency-doubled 520-nm solid-state lasers. π-polarization is the polarization parallel to the C-axis of the sapphire crystal. σ-polarization is defined as the polarization perpendicular to the C-axis. The absorption is more significant for the π-polarization than the σ-polarization. For efficient pumping of Ti:Al_2O_3 crystal, π-polarization should be used.

doi:10.6342/NTU202203086

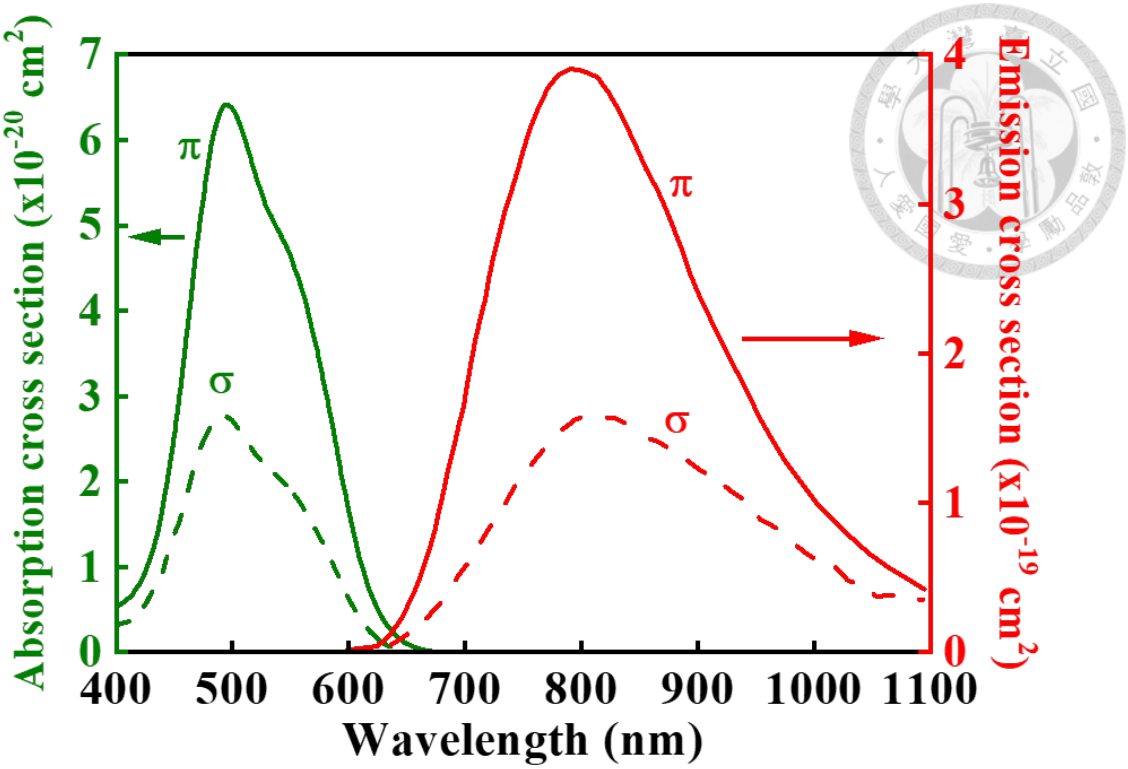

Fig. 2.6. Absorption cross-sections and emission cross-section for the $^2T_2$-^2E transition in Ti:Al_2O_3 for both polarizations [55].

By absorbing pump light, a ground-state electron was excited. The excited electron relaxes quickly to the lowest level of the ^2E_g state. The transition of the ^2E_g excited state to the $^2T_2$ ground state occurs by non-radiative and radiative, which generates a phonon by spontaneous emission or stimulated emission. Fluorescence centered at 790 nm with a 3-dB bandwidth of 180 nm generated from the ^2E_g excited state to the $^2T_2$ ground state. Figure 2.6 shows the fluorescence spectra and the calculated gain spectrum (red line), corresponding to the central wavelength of 795 nm. The peak of fluorescence is at 760 nm. The cross-section of π-polarization is larger than that of σ-polarization, as shown in Fig. 2.6. It implies that the best laser operation is π-polarization. The wavelength-

doi:10.6342/NTU202203086

tuning range of the Ti^{3+}:sapphire lasers is from 660 to 1100 nm, with a gain peak at around 800 nm, as shown in Fig. 2.7. The wavelength-tunning range is limited by the increased loss from the ground state absorption of Ti^{3+} ions and the lowered gain from reducing the emission cross-section.

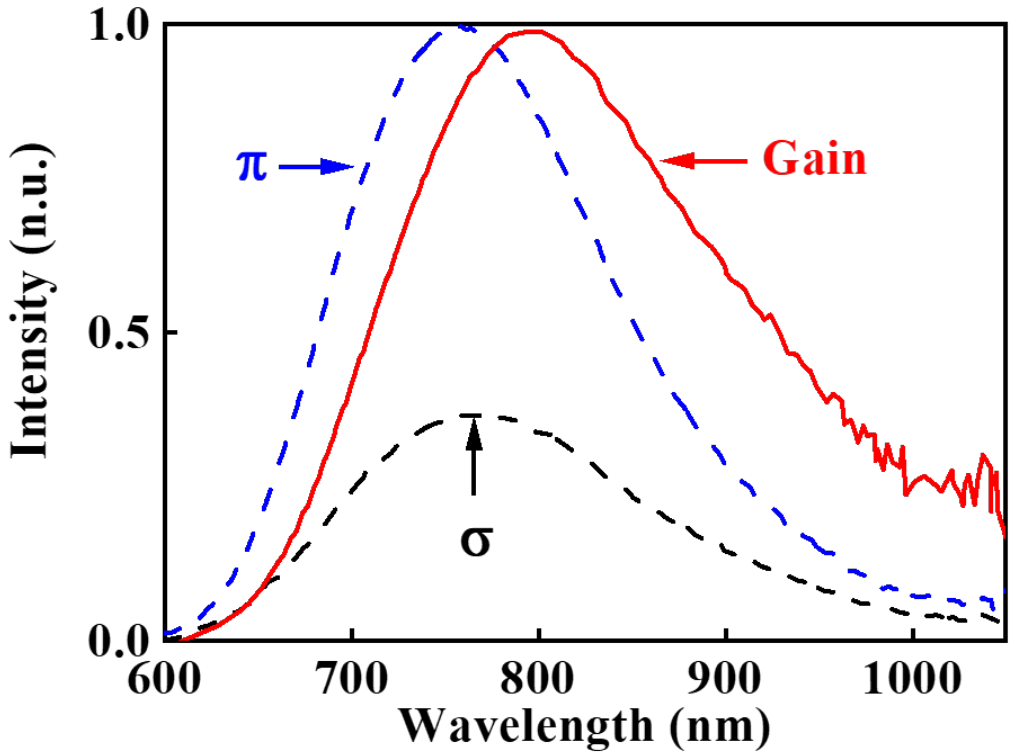

Fig. 2.7. Polarized fluorescence spectra and the calculated gain [55].

The Ti^{3+} ions were oxidized into Ti^{4+} ions with oxygen during the crystal growth process. The charge compensation is completed by forming an Al vacancy V_{Al}^{3-} with every three Ti^{3+} ions converted into Ti^{4+}. The oxidation reaction is written as follows [56]:

$$3Ti_{Al}^{3+} + \frac{3}{4}O_2 = 3Ti_{Al}^{4+} + V_{Al}^{3-} + \frac{3}{2}O \qquad (2.1)$$

Ti_{Al}^{3+} or Ti_{Al}^{4+} are a Ti^{3+} ion or Ti^{4+} ion substituting in an Al^{3+} ion at the

doi:10.6342/NTU202203086

octahedron center, respectively. The Ti^{4+} ion in the sapphire host can be excited by the UV light and produces a blue-green band emission [57].

When the Ti^{4+} ions are present in the Ti:Al_2O_3 crystal, the fluorescence from Ti^{3+} emission would be absorbed by Ti^{3+}-Ti^{4+} pairs. This phenomenon is associated with the residual absorption in the IR band is a cluster involving Ti^{3+} and Ti^{4+} ions with a neighboring Al^{3+} vacancy [6]. Figure 2.8 shows the polarized absorption spectra in the near-infrared region, which peaks between 800 and 850 nm, usually referred to as the residual absorption. The residual absorption at the π-polarization was smaller. The residual absorption is proportional to the Ti^{3+}–Ti^{4+} pairs' concentration and, consequently, the product of the Ti^{3+} and Ti^{4+} concentrations [56-58]. The residual absorption is a significant factor in the impairment of laser performance. Crystal quality is usually identified with a figure of merit (FOM), defined as the absorption constants' ratio at the pump and the lasing wavelengths. With the definition of FOM as $\alpha_{514nm}/\alpha_{820nm}$, the 0.1-wt.% Ti:$Al_2O_3$ crystal with a FOM as high as 1000 was reported [59]. α_{514nm} and α_{820nm} are 514 and 820 nm absorption coefficients, respectively. Considering larger emission cross-sections and smaller residual absorption, lasing operation in the π-polarization is favored.

doi:10.6342/NTU202203086

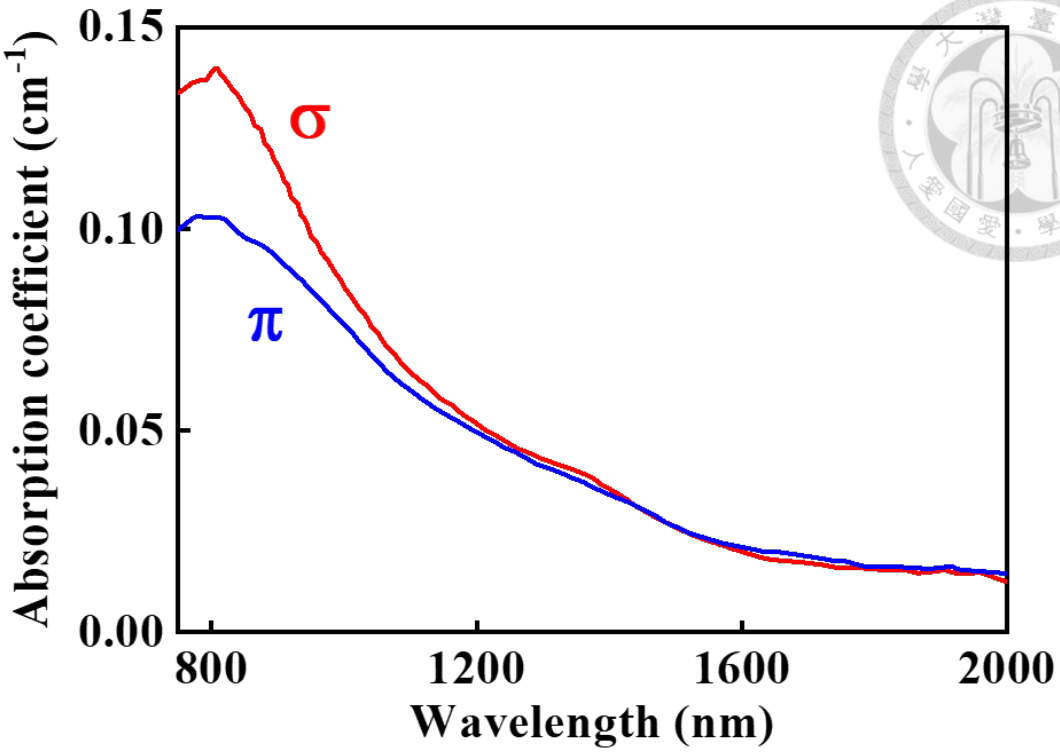

Fig. 2.8. Absorption spectra of Ti:sapphire in the near-infrared region for the σ and π polarizations (Ti concentration of 0.1 wt.%) [56].

The out-evaporation during the growth process is another reduction of the Ti^{3+} concentration. Titanium ions are diffused in the crystal cross-section during growth processes and then out-evaporated. That was caused by the ion radius mismatch with Al^{3+} ions (the radius of Al^{3+} ions and Ti^{3+} ions were 0.51 Å and 0.81 Å, respectively). The segregation coefficient k of the Ti^{3+} ion is defined as:

$$k = \frac{c^s}{c^L} \tag{2.2}$$

where c^s and c^L are the concentrations of the grown crystal and the melt, respectively. The segregation coefficient of the Ti^{3+} ions in the Ti:sapphire crystal was

doi:10.6342/NTU202203086

measured to be 0.14 to 0.20 [60]. To avoid heavy diffusions of Ti^{3+} ions, the reduction of the growth process was necessary. The optical and physical properties of Ti:sapphire crystal are summarized in Table 2.1.

Table 2.1. The optical and physical properties of the Ti:sapphire crystal.

Melting point	2040 °C
Boiling point	2980 °C
Mohr hardness	9
Density	3.97–3.99 g/cm^3
Ti concentration (0.1 wt.%)	3.33×10^{19} cm^{-3}
Thermal conductivity [50]	32.5 W/m·K (∥ c-axis) 30.3 W/m·K (⊥ c-axis)
Thermal optic coefficient	12.6×10^{-6} K^{-1}
Thermal expansion coefficient [50]	6.66×10^{-6} K^{-1} (∥ c-axis) @ 293–323 K 5×10^{-6} K^{-1} (⊥ c-axis) @ 293–323 K 7×10^{-6} K^{-1} (∥ c-axis) @ 310–670 K 7.7×10^{-6} K^{-1} (⊥ c-axis) @ 310–670 K
Lattice constant	a = b = 4.784 Å, c = 12.967 Å
3-dB fluorescence bandwidth	180 nm
Absorption cross-section [55]	6.4×10^{-20} cm^2 @ 490 nm (π) 2.8×10^{-20} cm^2 @ 490 nm (σ) 2.3×10^{-20} cm^2 @ 516 nm (π) 1.2×10^{-20} cm^2 @ 516 nm (σ)
Emission cross-section [61]	2.4×10^{-19} cm^2 @ 790 nm (π) 1.3×10^{-19} cm^2 @ 790 nm (σ)
Refractive index [52]	n_o = 1.773, n_e = 1.764 @ 520 nm n_o = 1.761, n_e = 1.753 @ 780 nm
Fluorescence lifetime [55,62]	3.85 μs @ 0 K 3.15 μs @ 300 K

doi:10.6342/NTU202203086

2.2 Modeling of Ti:sapphire Crystal Fiber

2.2.1 Energy Level System and Rate Equations

The energy level system of the Ti^{3+} ions in α-Al_2O_3 is a four-level system, as shown in Fig. 2.9. By absorbing pump phonons, Ti^{3+} ions in the ground state |0> are excited to the excited state |3> and relax fast to the meta-stable state |2> with non-radiative decay. Excited ions in the meta-stable state |2> return to the state |1> generating fluorescence phonons by either the spontaneous or stimulated emissions. Ions in the |1> relax to the ground state |0> with a very short lifetime.

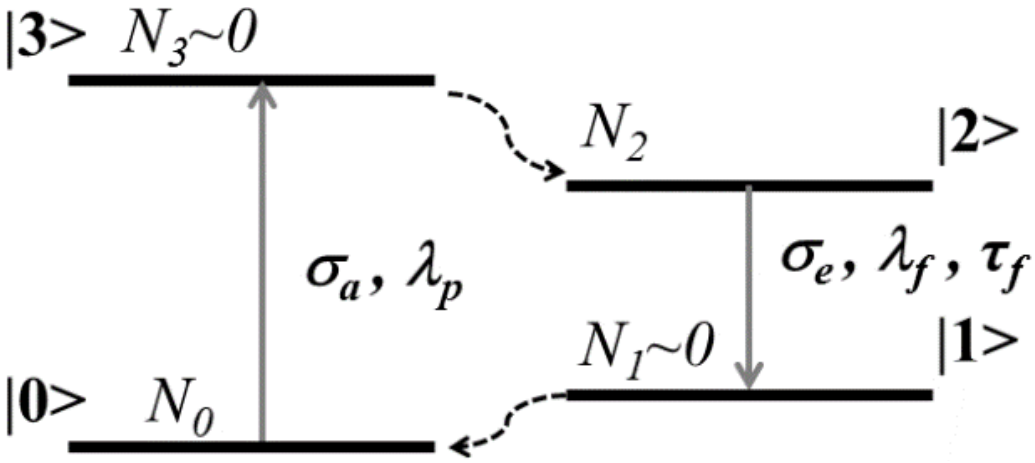

Fig. 2.9. Simplified energy level diagram of $Ti:Al_2O_3$ crystal.

Based on Fig. 2.9, the rate equation describing the dynamics of the excited state population density can be expressed as

$$\frac{dN_2(z)}{dt} = N_0(z)R_{03}(z) - N_2(z)W_{21}(z) - \frac{N_2(z)}{\tau_f} \tag{2.3}$$

$$N_0(z) = N_T - N_2(z) \tag{2.4}$$

where R_{03} is the transition probability of the ground state absorption, W_{21} is the

doi:10.6342/NTU202203086

transition probability of the stimulated emission, and τ_f is the fluorescence lifetime. The total ion density N_T is equal to the sum of the population density in the meta-stable state $N_2(z)$ and that in the ground state $N_0(z)$, since the population densities in other energy states are assumed to be negligible.

These parameters are defined as

$$R_{03}(z) = \frac{I_p(z)\sigma_a\lambda_p}{hc} \tag{2.5}$$

$$W_{21}(z) = \Sigma\frac{I_s(\lambda_i,z)\sigma_e(\lambda_i)\lambda_i}{hc} \tag{2.6}$$

where I_p is the pump intensity at the pump wavelength λ_p, and $I_s(\lambda_i)$ is the wavelength-dependent signal intensity.

From Eqs. (2.3) and (2.4), the steady-state equation is derived as

$$N_2(z) = N_T\frac{R_{03}(z)}{R_{03}(z)+W_{21}(z)+\frac{1}{\tau_f}} \tag{2.7}$$

The spectral density of the spontaneous emission intensity in the wavelength from v to $v + dv$ per one polarization can be expressed as [14]:

$$S_{sp}(v)dv = hv\frac{c}{n}\sigma_e(v)M(v)dv \tag{2.8}$$

where $S_{sp}(v)$ is the spectral power density of the spontaneous emission, and $M(v)$ is the density of the optical modes. The density of optical modes $M(v)$, the number of modes per unit volume of the resonator per unit bandwidth surrounding the frequency v. Overall, 301 wavelengths were simulated ranging from 650–950 nm. In a three-

doi:10.6342/NTU202203086

dimensional resonator, such as a bulk crystal, the optical mode density is expressed as [63]:

$$M_{3D}(\nu) = \frac{8\pi\nu^2}{c^3} \tag{2.9}$$

While in a one-dimensional resonator, such as a single-mode optical fiber, the mode density becomes [63]:

$$M_{1D}(\nu) = \frac{2n}{c} \cdot \frac{1}{A_{1D}} \tag{2.10}$$

The term A_{1D} is the cross-sectional area of the 1D resonator.

The crystal fibers are mostly highly multimode. The geometry of highly multimode fiber is similar to a 3D resonator with a narrow acceptance angle. Equation (2.8) describes the optical power emitted into the whole 4π solid angle.

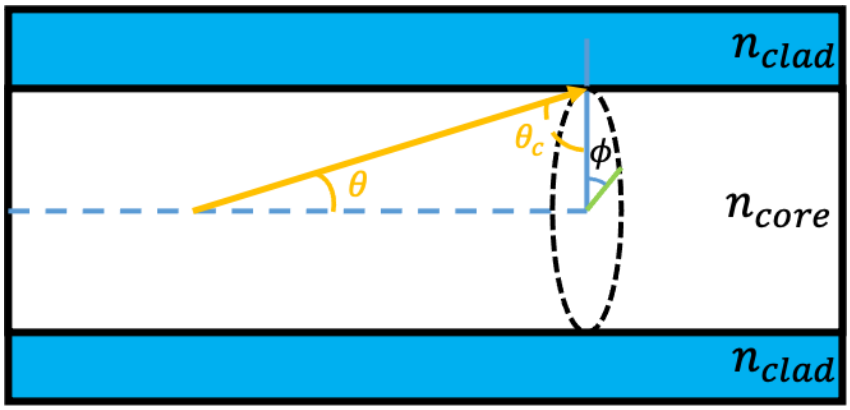

Fig. 2.10. Schematic of the inner solid angle of optical fiber.

In Fig. 2.10, the spontaneous emission of crystal fiber can only be captured within the solid angle (considering only forward direction):

$$\Omega = \int_0^{2\pi} \int_0^{90^o-\theta_c} sin\theta d\theta d\phi = 2\pi(1-sin\theta_c) \tag{2.11}$$

doi:10.6342/NTU202203086

$$sin\theta_c = \frac{n_{clad}}{n_{core}} \tag{2.12}$$

$$\Omega = 2\pi\left(1 - \frac{n_{clad}}{n_{core}}\right) \tag{2.13}$$

where n_{core} is the refractive index of the fiber core, n_{clad} is the refractive index of the fiber cladding and θ_c is the critical angle.

We can rewrite Eq. (2.8) in the wavelength domain with the use of Eq. (2.9) and Eq. (2.13):

$$S_{sp}(\lambda) = \frac{4\pi n_{core}(n_{core} - n_{clad})hc^2}{\lambda^5}\sigma_e(\lambda) \tag{2.14}$$

This is the spectral density of spontaneous emission intensity per active ion per polarization per direction in a highly multimode fiber.

For single-mode or few-mode crystal fibers, such as those cladding with high-index glass or ceramics, are similar to a 1D resonator. We can then rewrite Eq. (2.8) with Eq. (2.10) in the wavelength domain and divide it by 2 for considering only forward direction:

$$S_{sp}(\lambda) = \frac{2hc^2}{\lambda^3 A_{core}}\sigma_e(\lambda). \tag{2.15}$$

This is the spectral density of spontaneous emission intensity per active ion per polarization per direction in a single-mode or few-mode fiber. A_{core} is the cross-sectional area of a core.

doi:10.6342/NTU202203086

2.2.2 Evolution of Optical Powers in Crystal Fiber

The fluorescence generated by the crystal core emits in 4π radiation, and is captured by the glass-clad of the Ti:Al_2O_3 CF. The evolution of the spectrally resolved fluorescence power $P_f^{\pm}(z,\lambda_i)$ in the i_{th} wavelength slot at the axial position z is then:

$$\frac{dP_f^{\pm}(z,\lambda_i)}{dz} = \pm\{\sigma_e(\lambda_i)N_2(z) \mp \alpha_{pl}^f\}P_f^{\pm}(z,\lambda_i) + 2N_2(z)A_{core}S_{sp}(\lambda_i)\Delta\lambda_i \quad (2.18)$$

where $\Delta\lambda_i$ is the width of the i_{th} wavelength slot centered at λ_i, and α_{pl}^f is the propagation loss. The term $S_{sp}(\lambda_i)$ is the spectral power density of spontaneous emission per active ion per polarization per direction, as given by Eq. (2.14) for multimode crystal fibers and Eq. (2.15) for single-mode and few-mode crystal fibers.

The absorption mechanism of the pump only includes the ground-state absorption, no excited-state absorptions. The evolution of the pump power $P_p^{\pm}(z)$ along the fiber is described as:

$$\frac{dP_p^{\pm}(z)}{dz} = \mp[\sigma_a N_0(z) + \alpha_{pl}^p]P_p^{\pm}(z) \quad (2.19)$$

where α_{pl}^p is the propagation loss of the pump.

2.2.3 The Distributed Model for Ti:sapphire Crystal Fiber

The distributed model is based on the "relaxation method," which was extensively used in fiber lasers [64]. To solve the laser performance, boundary conditions must be

doi:10.6342/NTU202203086

met at both ends of the cavity. A general set of boundary conditions can be written as:

$$\begin{aligned} P_p^+(0) &= P_{p\_in}^+\left(1-R_1^p\right)T_{c1}^p + P_p^-(0)R_1^pT_{c1}^{p2} \\ P_s^+(\lambda_i,0) &= P_s^-(\lambda_i,0)R_1^s(\lambda_i)T_{c1}^{s2}(\lambda_i) \\ P_p^-(L) &= P_{p\_in}^-\left(1-R_2^p\right)T_{c2}^p + P_p^+(L)R_2^pT_{c2}^{p2} \\ P_s^-(\lambda_i,L) &= P_s^+(\lambda_i,L)R_2^s(\lambda_i)T_{c2}^{s\,2}(\lambda_i) \end{aligned} \tag{2.20}$$

where $P_{p\_in}^+$ and $P_{p\_in}^-$ are the input pump powers at the input and output faces, respectively. R is the cavity mirror reflectance, and T_c is the transmittance between the crystal fiber and the cavity mirrors. The number in the subscripts denote the end of the crystal fiber, 1 for the input end and 2 for the output end. An "s" in the superscript means the parameter is for signal light, and "p" is for the pump light. Because the signal is broadband, the reflectance and the transmittance are defined as the wavelength functions of the signal light. A schematic illustrating these parameters is shown in Fig. 2.11.

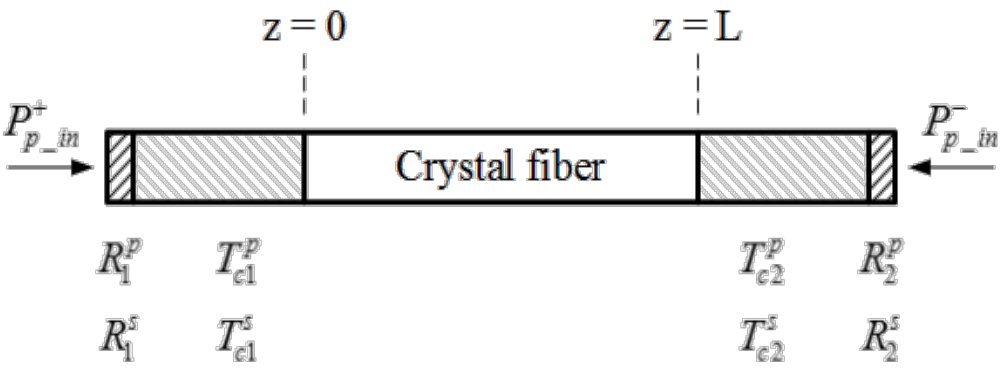

Fig. 2.11. Schematic of boundary conditions in crystal fiber laser modeling

In the relaxation method for laser modeling, the power revolution equations are

doi:10.6342/NTU202203086

numerically integrated back and forth iteratively until a stable solution is reached. At first, we assume pump distributions $P_p^{\pm}(z)$ with an exponential or linear decay along the distance. The shape of the pump distribution does not affect the final solution but only influences the time required for convergence. With the assumed pump distribution and zero signal power, we can solve $N_2(z)$ with Eq. (2.7). After $N_2(z)$ is known, the integrations of the forward powers in Eq. (2.18) and Eq. (2.19) are worked out from $z = 0$ to $z = L$, with the initial forward conditions determined from Eq. (2.20). The backward integration is carried out with updated initial backward conditions and $N_2(z)$. The integration is repeated back and forth iteratively, and after each integration, the initial conditions for the subsequent integration and $N_2(z)$ are updated. If N_2 is over-depleted in the one integration, then the subsequent integration in the opposite direction will lower the signal power and under-deplete N_2, similar to the relaxation oscillation in real lasers. The laser output spectrum gradually converges to a final solution during the iterations. The iteration is stopped when the largest error between two successive spectra is less than a given tolerance of 10^{-6}. For amplified spontaneous emission (ASE) simulation, the cavity mirror reflectance (R) is 0, and the transmittance between the crystal fiber and the cavity mirrors (T_c) is 1.

doi:10.6342/NTU202203086

Chapter 3

Fabrication Process and Analysis of Glass-clad Ti:sapphire Crystal Fiber

Ti:sapphire is a common crystal that can be grown through numerous methods such as the Czochralski method [65], Kyropoulos method [66-67], Verneuil method [68], heat exchanger method [69], and micro-pulling-down method [70–72]. To reduce the core diameter, the laser-heated pedestal growth (LHPG) was used in this thesis.

3.1 Laser-heated Pedestal Growth System

In this chapter, the single crystallin core fiber fabrication with the LHPG system is introduced. Finally, the cladding process was produced by the glass cladding process. CO_2 laser was used as the heating source to grow crystals by Stone and Burrus in 1975 [73]. Fejer *et al.* first developed the LHPG system in 1984 [74]. The LHPG method made it possible to grow single crystals with a few microns in diameter. The floating molten zone is supported by the source material so that contamination can be minimized.

The LHPG system setup is shown in Fig. 3.1. A CO_2 laser (C-30+, Coherent) is used as the heat source for melting the source crystals. A He-Ne laser (25-LHR-111-249, Melles Griot) is aligned with the CO_2 laser beam with a beam combiner to facilitate the adjustment of optic paths of the CO_2 laser for the LHPG system.

The CO_2 laser power can be changed by tuning the duty cycle of a radio frequency

doi:10.6342/NTU202203086

(RF) driving signal. To further adjust the laser power, we use a linear polarizer. The polarizer is a mechanical rotating linear polarizer (PAZ-10-AC, II-VI). The relative polarization angle between the CO_2 laser and the linear polarizer adjusts the CO_2 laser power. The power of the CO_2 laser is detected with a power meter (PM) by using a beam splitter before CO_2 laser beam expansion. A LabVIEW feedback program controls the rotating linear polarizer angle to adjust and stabilize the power of the CO_2 laser.

To control the whole LHPG system, we use the same LabVIEW program mentioned above. The beam diameter of the CO_2 laser is expanded from 4 mm to 30 mm with a pair of convex ZnSe lenses (ZNSE PO/CX LENS 2.0”DIA 7.5”FL and 0.5”DIA 1.0”FL, II-VI) before entering the growth chamber. Two stereo microscopes with long-working distance parfocal objective lenses (SZX7, Olympus) are set next to the growth chamber to observe the melting zone.

doi:10.6342/NTU202203086

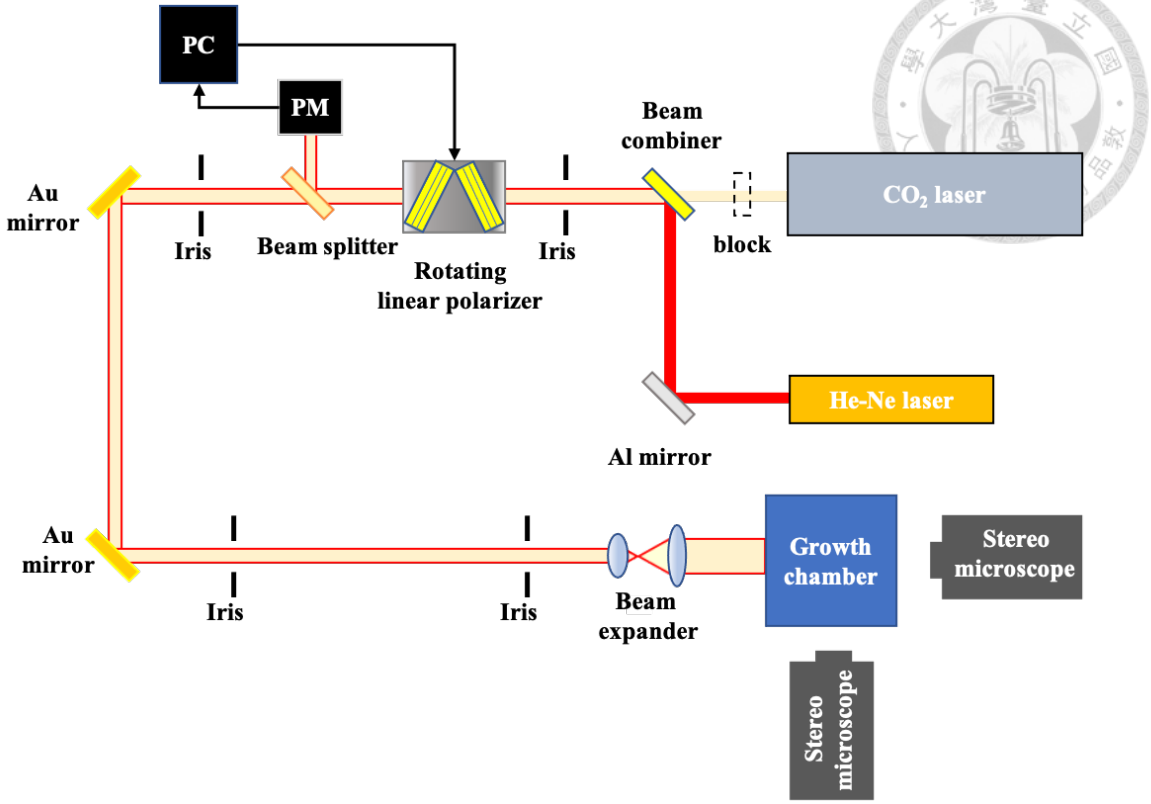

Fig. 3.1. The setup of the LHPG system. PM: power meter. PC: the personal computer.

A schematic diagram of the growth chamber and the side view are shown in Fig. 3.2. The CO_2 laser beam is transformed into a toroidal-shaped beam with a reflaxicon (US-120-169176-01 and US-120-169282-01, II-VI). The beam is reflected upwards by a 45° planar mirror and then focused by a paraboloidal mirror with a focal length of 25 mm. There is circular clearance at the center of the planar mirror and the paraboloidal mirror to let the source material and the seed crystal go through. A side-view photo of the growth chamber is shown in Fig. 3.3.

doi:10.6342/NTU202203086

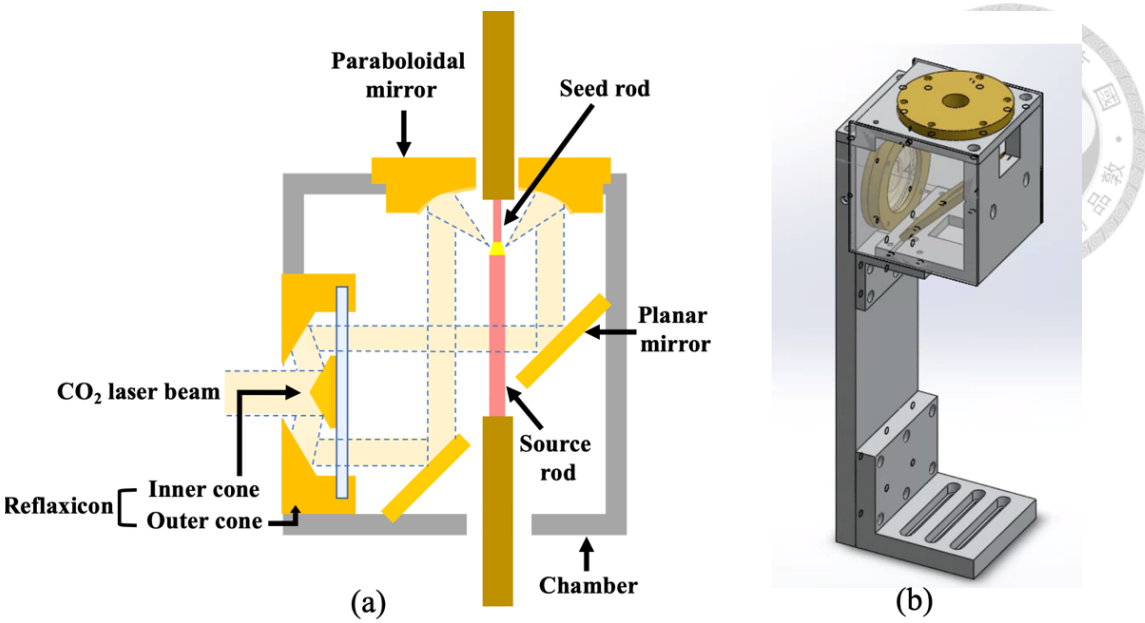

Fig. 3.2. (a) A schematic of the growth chamber. (b) A 3D view of the growth chamber created with SolidWorks. The CO_2 laser beam after the reflaxicon is a toroidal-shaped beam instead of two split beams [75].

Fig. 3.3. A photo of the growth chamber, illustrating the paraboloidal mirror and the focused CO_2 beam on the source rod.

doi:10.6342/NTU202203086

3.2 Single-Crystal Fiber Growth

Figure 3.4 shows the single crystal fiber growth process. The source crystal and the seed crystal are held with metal grips, similar to those in mechanical pencils, fixed to brass rods with a diameter of 6.35 mm. Each yellow brass rod is mounted on a 5-axis manual stage to align the crystal source and the seed crystals, whereas two motorized stages control the distance between them on the vertical axis for feeding the source material rod upward and drawing the grown crystal fibers from the melting zone. The top of the source rod is placed at the laser focal position in the growth chamber.

The seed crystal rod is pushed downward to the melting zone, as shown in the left part of Fig. 3.4. Surface tension confined the molten zone on the vertical source rod [4]. The growing crystal fiber diameter can be adjusted by tuning the laser power and the speeds of the two motorized stages. After touching the melting zone, the seed crystal rod is pulled upwards for crystal fiber growth, and the source crystal is fed upwards to supply the materials into the melting zone. The crystal seed rod pulls the melting zone upwards and provides directional cooling in the vertical direction. Therefore, the growing crystal's crystallographic orientation follows that of the seed rod.

doi:10.6342/NTU202203086

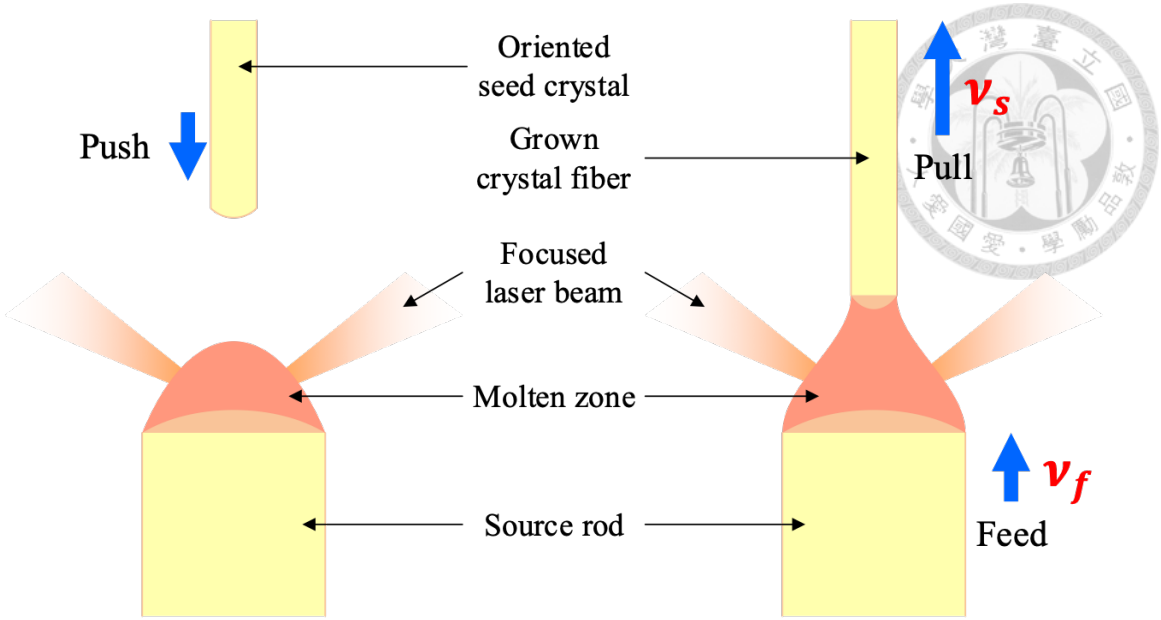

Fig. 3.4. Single-crystal fiber growth process. Left: before the crystal fiber growth. Right: during the crystal fiber growth.

To create a crystal fiber with a uniform diameter along its axes, an excellent and stability melting zone is needed [76]. The molten source rod's mass sent into the melting zone must equal that brought away by the growing crystal fiber. In the steady-state, the ratio between the cross-sectional area of the crystal fiber, A_f, and that of the source rod, A_s, can then be determined by the following equation:

$$\frac{A_f}{A_s} = \frac{\rho_s v_s}{\rho_f v_f} \tag{3.1}$$

where ρ_s and ρ_f are the molten source rod's volumetric mass densities and the grown crystal, respectively. v_s and v_f are the moving speeds of the source rod and the grown crystal fiber, respectively. A schematic view of the melting zone can be seen in Fig. 3.5, where D_f and D_s are the diameters of the growing crystal and source rod, h is the height

doi:10.6342/NTU202203086

of the melting zone, and φ is the growth angle, measured between the growth axis and the tangent to the meniscus.

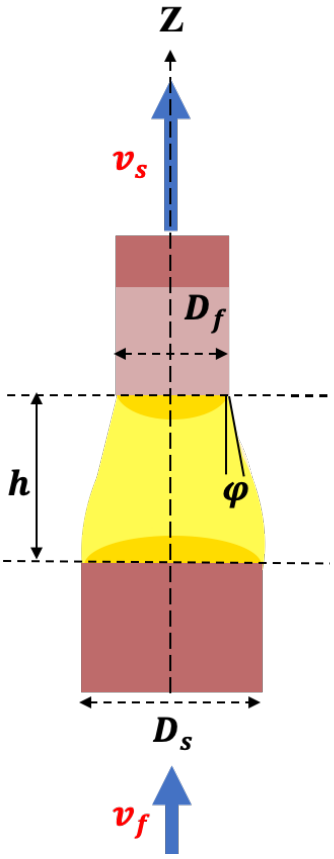

Fig. 3.5. Molten zone [76].

Because the source rod and seed rod materials are the same, ρ_s and ρ_f are also the same. If both the source rod and the crystal fiber have circular cross-sectional areas, the ratio between their diameters will be:

$$\frac{D_f}{D_s} = \sqrt{\frac{v_s}{v_f}} \tag{3.2}$$

The heat flux's stability in the growing crystal, which moves away from the melting zone, consists of two parts: first is the heat flux from the melting zone toward the upper melting zone interface. The second is the latent heat of crystallization. Surface

doi:10.6342/NTU202203086

tension and gravity are the only active forces during the growth process. The angle between the meniscus and the growth axis, φ, and the height-to-width ratio of the melting zone must be controlled to ensure the growing crystal's quality. φ is related to the surface tension of the melt and its ability to wet the crystal. φ_0, a stabilized growing angle, is a material constant independent of the fiber growth rate, diameter, and zone length, but not independent of the crystallographic orientation. The relevant relationships can be expressed as $\cos\varphi_0 = \sigma_{sg}^2 + \sigma_{lg}^2 - \frac{\sigma_{sl}^2}{2\sigma_{sg}\sigma_{lg}}$ [76], where σ_{sg}, σ_{lg}, and σ_{sl} are the interfacial free energies between interfaces of solid-gas, liquid-gas, and solid-liquid, respectively. Perturbations in the length or volume of the melting zone lead to diameter variations of grown crystals. Therefore, perturbations in the melting zone, which are environmental vibrations and CO_2 power variations, endanger crystal fibers' uniformity. Nonuniform fibers exhibit increased Rayleigh scattering loss.

In practice, it is easy to control the melting zone when its height is smaller than half of the diameter of the source rod, $h \leq \frac{D_s}{2}$. The shape of the melting zone becomes unstable if the diameters D_s and D_f differ too much. Therefore, the $\frac{D_s}{D_f}$ ratio was controlled to be less than 4.5 in the present work. If the $\frac{D_s}{D_f}$ ratio is higher than 4.5, the fiber growth would be tough. The target diameter of the Ti:sapphire single crystal fiber is 16 μm. A bulk Ti:sapphire crystal (Casix) was cut into rectangular rods with a 500 μm × 500 μm cross-section to serve as the source material. The rectangular rod was first

doi:10.6342/NTU202203086

grown into a crystal fiber with a 290-μm diameter. The 290-μm crystal fiber was then used as the source rod to grow a 68-μm crystal fiber. Finally, the 68-μm crystal fiber was grown into the 16-μm crystal fiber. The photos of the molten zones for the growth of 290, 68, and 16 μm Ti:sapphire single-crystal fibers are shown in Fig. 3.6. For the 290 μm fiber growth, the ratio of the height to the width of the molten zone was about 1.5.

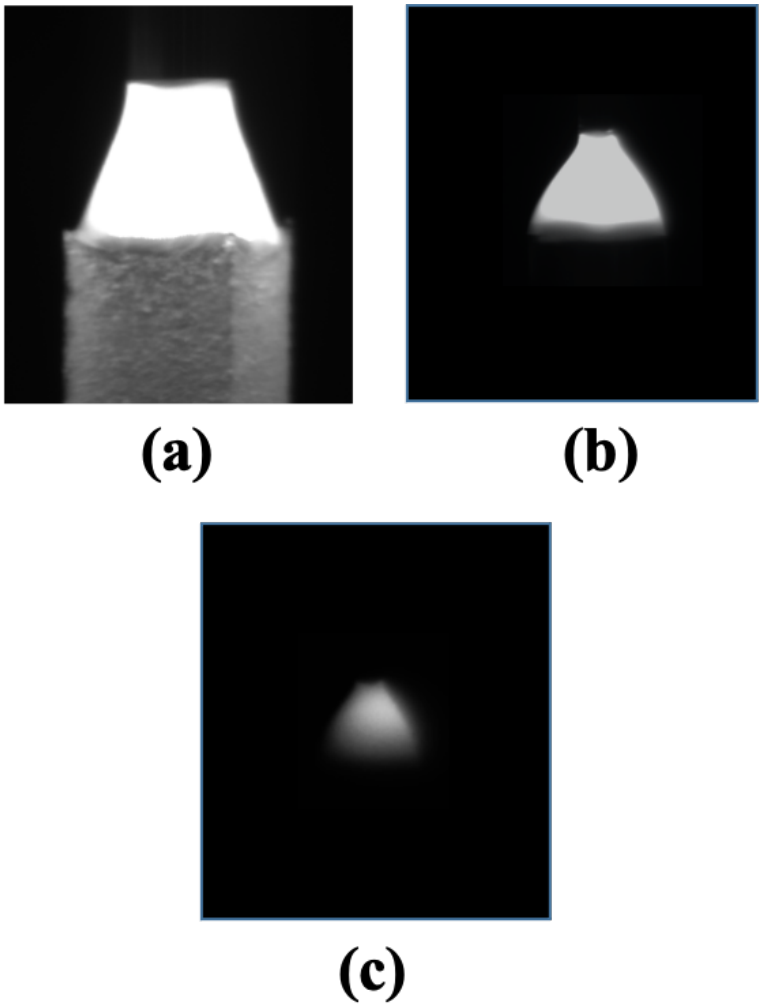

Fig. 3.6. Photos of the molten zone of Ti:sapphire single-crystal fiber growth: (a) 290 μm fiber growth from rectangular rod (500 μm), (b) 68 μm fiber growth from 290 μm rod, and (c) 16 μm fiber growth from 68 μm rod.

doi:10.6342/NTU202203086

3.3 Reduction Annealing Process

During crystal-fiber growth, Ti^{3+} ions are oxidized to Ti^{4+} ions, and Ti^{3+}-Ti^{4+} or Ti^{4+}-Ti^{4+}pairs form, which heavily reduces the fluorescence efficiency of Ti^{3+} ions. Therefore, a reduction process after single crystal core fiber is necessary. Previous researchers reported that hydrogen could be used as an effective reducing atmosphere [77-80].

A high-temperature furnace (LTF-18, Lenton) was used in the reduction annealing process. Figure 3.7 shows the reduction annealing setup. Crystal fibers grown by the LHPG process were placed on a pure boron nitride boat and inserted into the furnace. The chamber had an exhaust tube leading to a conical flask with a stopper connected to another conical flask with a tube submerged in water. That tube was inserted underwater to keep the chamber's pressure slightly higher than atmospheric pressure and prevent O_2 from entering the chamber during the annealing process. This is important to avoid explosive reactions from happening due to a mixture of O_2 and H_2. During the annealing process, a gas mixture of 5% H_2 and 95% Ar was continually pumped into the chamber to provide H_2 for the reduction reaction.

The gas flow was 150 mL/min (sccm) and the sintering temperature was 1600 °C for 18 hours. The fluorescence efficiency of the annealed fiber was 100 times higher than that of the non-annealed single-crystal fiber.

doi:10.6342/NTU202203086

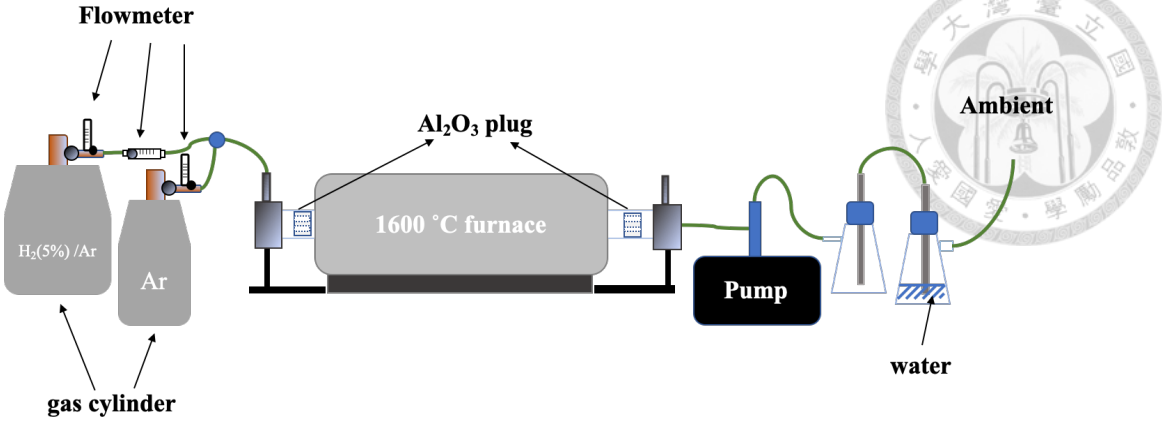

Fig. 3.7. Schematic view of the setup for the reduction annealing process [81].

3.4 Glass-cladding Process

Compared to the single-crystal fiber, the glass-clad crystal fiber provides a more robust structure and better light confinement. The guiding properties of the crystal core are sensitive to environmental perturbation, such as the changes in temperature or mechanical stress. Therefore, fibers can be covered by thermal grease or metal, but this results in a non-homogeneous refractive index surrounding the core and increases the extinction coefficient. The core can be cladded with glass to overcome this problem, reducing the propagation losses of the crystal fiber.

In the present work, we introduce two different cladding processes for the fabrication of glass-cladded crystal fibers: a laser heating method [80, 82-84] and a micro furnace method. The borosilicate capillary made of Corning 7740 was adopted. It is widely known as the Pyrex borosilicate glass. A borosilicate glass consists of 80.6 wt.% SiO_2, 13.0 wt.% B_2O, 4.0 wt.% Na_2O, 2.3 wt. % Al_2O_3, and other impurities.

doi:10.6342/NTU202203086

The properties of borosilicate glass are low thermal expansion coefficient, high resistance to thermal shock, nearly colorless clear appearance, and high elasticity and mechanical strength. The softening temperature of the borosilicate glass is 821 °C.

3.4.1 Microfurnace Heating Process

Compared to the laser heating process, the micro furnace process provides some advantages to improve the packaging process. The microfurnace was not sensitive to the sample alignment, which was stable for a capillary package process. The residual strain was reduced with a larger heating region, which provided a slower cooling rate. The microfurnace (Microtube THM-200, MXI) was constructed with a 10-mm diameter $MoSi_2$ heating coil, a commercial heating element with a maximal temperature of 1900 °C. The furnace is entirely ceramic with a volume of 2.87 × 2.87 × 5 cm^3 (W × D × H). The temperature sensor is a B-type thermocouple. The mechanism of indirectly heating glass capillaries in a furnace is different from that of laser heating, which transforms absorbed CO_2 laser power to soften the glass directly, providing a more stable temperature.

Figure 3.8 depicts the different parts of a micro furnace. Because of the larger heating area (10-mm diameter and 10-mm length), this microfurnace was not sensitive to the sample alignment, suitable for capillary packaging. Furthermore, the residual strain is reduced with a larger heating length and a ceramic containment device that

doi:10.6342/NTU202203086

provides a slower cooling rate. Lower residual strain can improve the quality of glass-clad Ti:sapphire crystal fibers. The microfurnace includes an additional B-type thermocouple that facilitates the control of the heating temperature. Thus, it prevented overheating and insufficient heating.

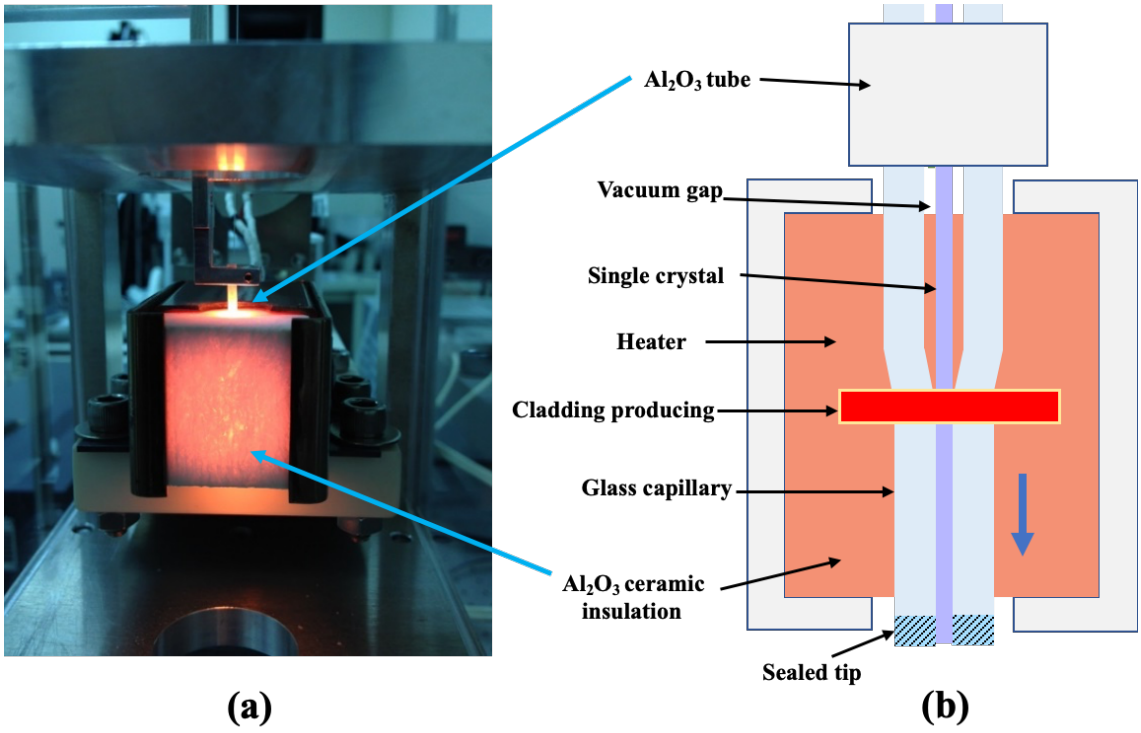

Fig. 3.8. (a) Photo of our microfurnace glass-cladding process setup and (b) schematic of the fiber-filled capillary during growth [75].

After the glass cladding process, the crystal fibers were placed in an aluminum holder and molten tin was poured into the holder to fix the crystal fiber. This tin packaging method improves the thermal dissipation of the crystal fiber. The packaged fibers were then cut into pieces with the desired lengths. Both ends of each section of the crystal fiber were ground and polished to have smooth surfaces, so the output light

doi:10.6342/NTU202203086

is perpendicular to the fiber's surfaces for later optical measurement, as shown in Fig. 3.9.

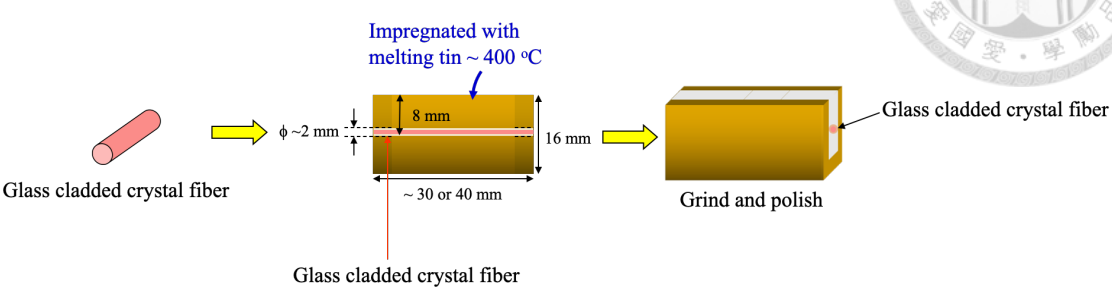

Fig. 3.9. The tin packaging steps [75].

3.5 Optical Property of Glass-clad Ti:sapphire Crystal Fiber

3.5.1 Measurement of Propagation Loss

Using the cut-back method and fitted, the waveguide's attenuation coefficients with crossed polarization directions were obtained, as shown in Fig. 3.10. The waveguide's attenuation coefficient includes a propagation loss and an absorption coefficient (absorbing from Ti^{3+} ions or Ti^{3+}-Ti^{4+} ion pairs). Table 3.1 summarizes the absorption and loss measurements at various exciting wavelengths. At 780 nm, the signal loss of glass-clad Ti:Al_2O_3 CF was 0.073 dB/cm, which includes the propagation loss and re-absorption of the Ti^{3+}–Ti^{4+} pair. The loss was markedly lower than that of the Ti:sapphire waveguides in the literature [85-91], which were typically approximately 0.65–3.498 dB/cm, as shown in Table 3.2. Distinguishing the polarization dependency is difficult because of the low re-absorption loss of the Ti^{3+}–

doi:10.6342/NTU202203086

Ti^{4+} pair. Based on the propagation loss of the glass-clad un-doped (pure) sapphire CF, the calculated absorption at 520 nm of glass-clad Ti:sapphire CF was 3.845 dB/cm (π) and 2.287 dB/cm (ρ), and the re-absorption of the Ti^{3+}–Ti^{4+} pair was 0.013 dB/cm. With the results, the figure of merit could be calculated as the following:

$$FOM\left(\frac{\alpha_{520}}{\alpha_{780}}\right) = \left(\frac{\alpha_{520}^{Ti} - \alpha_{520}^{Pu}}{\alpha_{780}^{Ti} - \alpha_{780}^{Pu}}\right) = \frac{4.1-0.26}{0.073-0.06} = 295.3 \quad (3.3)$$

α_{520}^{Ti} and α_{780}^{Ti} are the attenuation coefficients of glass-clad Ti:Al_2O_3 CF at 520 nm and 780 nm, respectively. α_{520}^{Pu} and α_{780}^{Pu} are the propagation loss coefficients of glass-clad pure Al_2O_3 CF at 520 nm and 780 nm, respectively. The figure of merit ($\alpha_{520}/\alpha_{780}$) was calculated higher than 250. By calculating with absorption coefficient at 520 nm (α_{520}), the 0.049 wt.% Ti^{3+} concentration of glass-clad Ti:Al_2O_3 CF was obtained. At the 0.049 wt.% Ti^{3+} concentration, the absorption cross section and emission cross section were similar to those of the commercial bulk material [55, 59, 61], but the figure of merit is still smaller than 1000 at the 0.1 wt.% Ti^{3+} concentration that in the literature [59].

doi:10.6342/NTU202203086

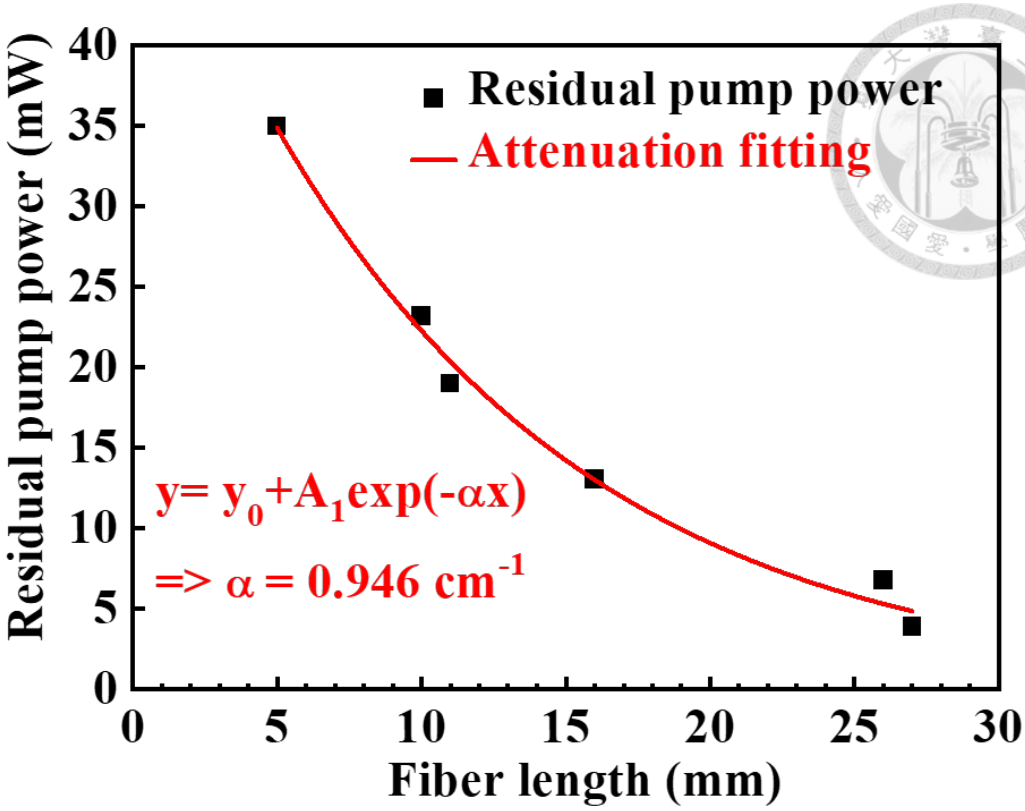

Fig. 3.10. Profiles of experiment and fitted profiles of residual pump power profile at 520-nm and π-polarization exciting [81].

Table 3.1. Attenuation coefficients of the glass-clad Ti:sapphire CF [84].

Attenuation coefficient (dB/cm)		Wavelength	
		520 nm	780 nm
Pure sapphire		0.26	0.06
Ti:sapphire CF	π-pol	4.1	0.073
	σ-pol	2.55	0.073

doi:10.6342/NTU202203086

Table 3.2. Propagation losses of Ti:sapphire waveguides at 780 nm [18].

Author	Year	Structure	Fabrication process	Propagation loss (dB/cm)
L. Wu *et al.* [78]	1995	Single CF	LHPG	3.5
A. A. Anderson *et al.* [86]	1997	Planar	Pulsed laser deposition	1.8
A. Crunteanu *et al.* [88]	2002	Rib	Reactive ion etching	3
C. Grivas *et al.* [92]	2004	Rib	Ar^{+}-Milled	1.7
L. Laversenne *et al.* [93]	2004	Buried	Proton implantation	0.7
V. Apostolopoulos *et al.* [94]	2004	Channel	Femtosecond-irradiation	2.3
L. M. B. Hickey *et al.* [88]	2004	Channel	Thermal-diffusion	0.7
C. Grivas *et al.* [89]	2005	Rib	PLD-grown	1.2
C. Grivas *et al.* [90]	2006	Buried-channel	Proton implantation	1
C. Grivas *et al.* [91]	2012	Channel	Written with pulse laser	0.65
S. C. Wang *et al.* [84]	2015	Glass-clad CF	LHPG	0.073

doi:10.6342/NTU202203086

3.5.2 Measurement of Ti:sapphire Lifetime

Because of its high surface-to-volume ratio of a fiber structure, a CF has a good heat dissipation. The fiber laser operation can be stable without any active cooling devices, which is evidenced by our Cr^{4+}:YAG CF laser [95]. The fluorescence lifetime of glass-clad Ti:sapphire CF is measured with different power and analyze the heat dissipation capability of the glass-clad CF.

A frequency-doubled CW 532-nm Nd:YVO_4 laser was employed as the pump source. The pump power is tuned via a half-wave plate and a polarization beam splitter, and the power is monitored with a beam sampler reflecting a small amount of the pump laser. Then, 16× aspheric lens pairs (5720-a, New Focus) and a mechanical chopper (MC1000A, Thorlabs) are used to modulate the pump beam at a 1-kHz rate. The 10-slot blade (MC1F10, Thorlabs) is placed at the focal plane to achieve a fall time of 90 ns. Nine of the 10 slots are blocked with aluminum foil to achieve the duty cycle of 5%. The beam sampler is used to divide a small amount of the modulated pump light into PD2 (DET10A/M, Thorlabs) as a trigger source of digital oscilloscope (TDS320, Tektronix). The polarization of pump light is tuned with a half-wave plate to become π-polarization. The 16× aspheric lens (5720-a, f = 16 mm, NA = 0.25, New Focus) is coupling lens, and a 60× aspheric lens (5720-b, f = 2.8 mm, NA = 0.65, New Focus) is collimating lens. The residual pump is blocked with a dichroic filter (LPD01-633RS-

doi:10.6342/NTU202203086

25, Semrock). A high-speed Si photodiode (DET200, Thorlabs) is the fluorescent detector, as shown in Fig. 3.11. The time-resolved fluorescence is shown in Fig. 3.12.

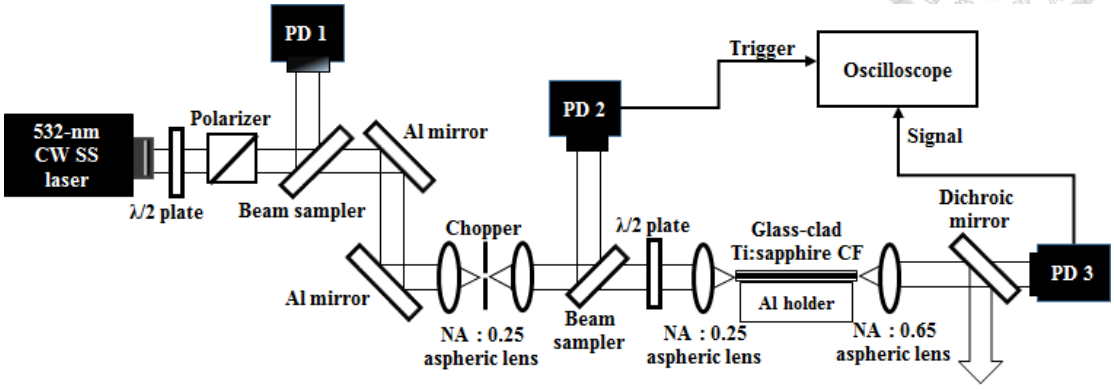

Fig. 3.11. Lifetime measurement setup. PD: photon detector [81].

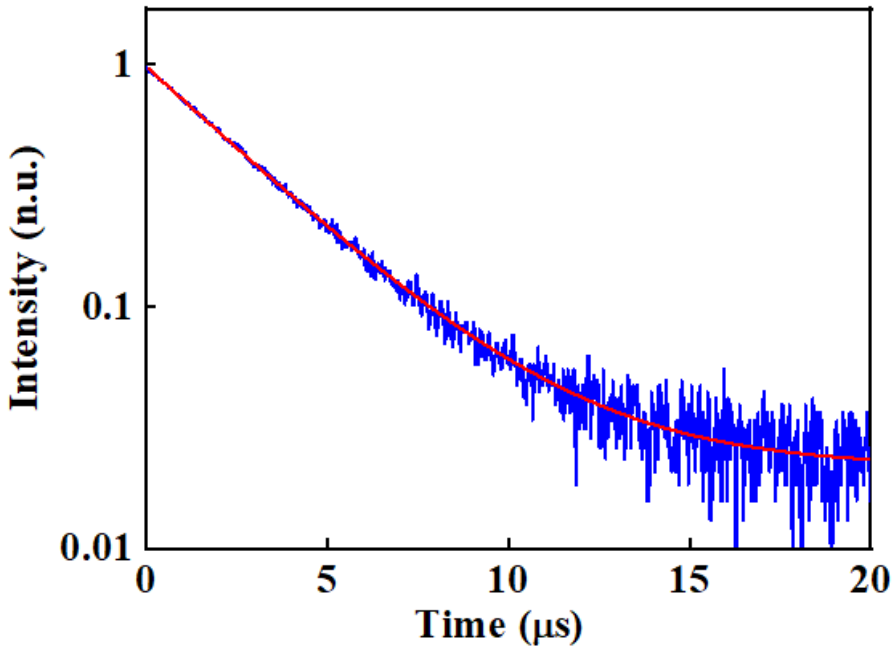

Fig. 3.12. Time-resolved fluorescence of Ti:sapphire CF. Blue line is fluorescence signal. Red line is fitting curve [81].

We measured the lifetime τ of Ti:sapphire CF at pump power of 94 mW. The fluorescent decays with an exponential time dependence exp(-t/τ), with τ = 3.12 μs,

doi:10.6342/NTU202203086

which is consistent with the 3.1–3.15 μs found in previous studies [55, 96]. However, the lifetime decreases with the increasing pump power due to the thermal effect. The relationships between lifetime and temperature are reported in [95, 97]. The lifetime is 3.15 μs at a room temperature of 300 K. The linear relationship assumption is $\tau_f = \tau_{f0} - \tau_{fT}(T - T_r)$, where T and T_r are temperature of the CF and room temperature, respectively; τ_f and τ_{f0} are the lifetime of the CF at T and T_r, respectively; τ_{ft} is the thermal lifetime coefficient, which is about -0.33 μs /W in our CF, as shown in Fig. 3.13.

With the measured lifetimes, temperatures of crystal core can be estimated with different absorbed pump powers. The maximum temperature of crystal core is only up to 329 K with 1.6-W full pump power, and lifetime is 2.67 μs. It proves that the glass-clad CF has high heat dissipation capability.

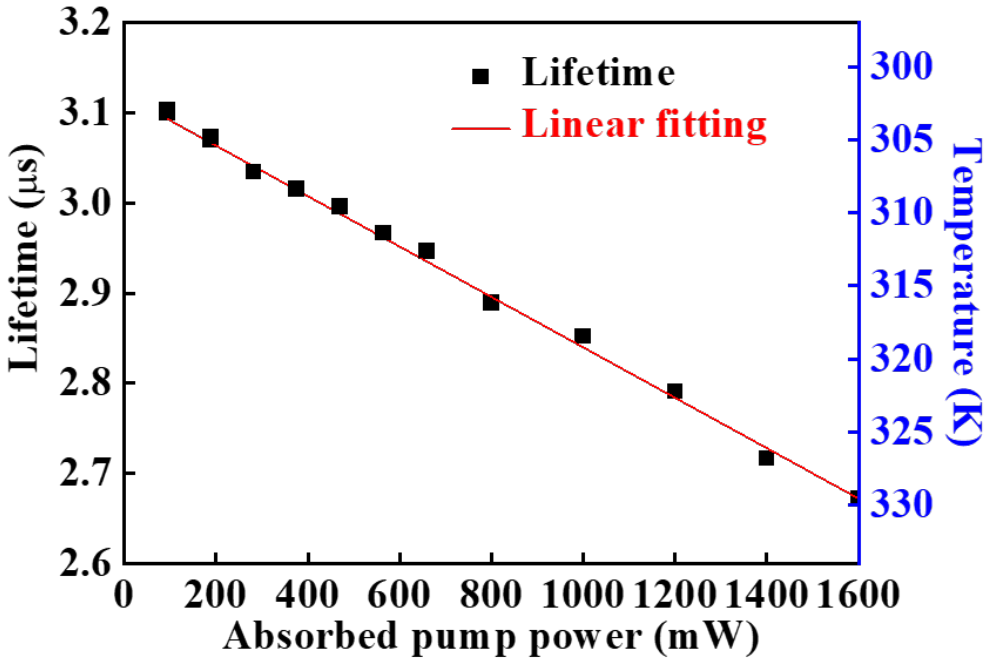

Fig. 3.13. Lifetime and temperature charges with different pump powers [81].

doi:10.6342/NTU202203086

3.6 Wavelength-tuning component

3.6.1 Diffraction Grating

Diffraction grating is an optical element that uses the periodic structure on the substrate to modulate the phase of reflected or transmitted light to achieve wavelength-tunning effect. Such elements are often used in monochromators and spectrum analyzers, using gratings for wavelength selection. The grating can be divided into reflection grating or transmission grating according to its own design. It can be divided into blazed grating (Sawtooth grooves) or holographic grating (Sinusoidal grooves) structure according to the periodic structure of grating.

A blazed grating is designed to optimize the maximal grating efficiency in a given diffraction order

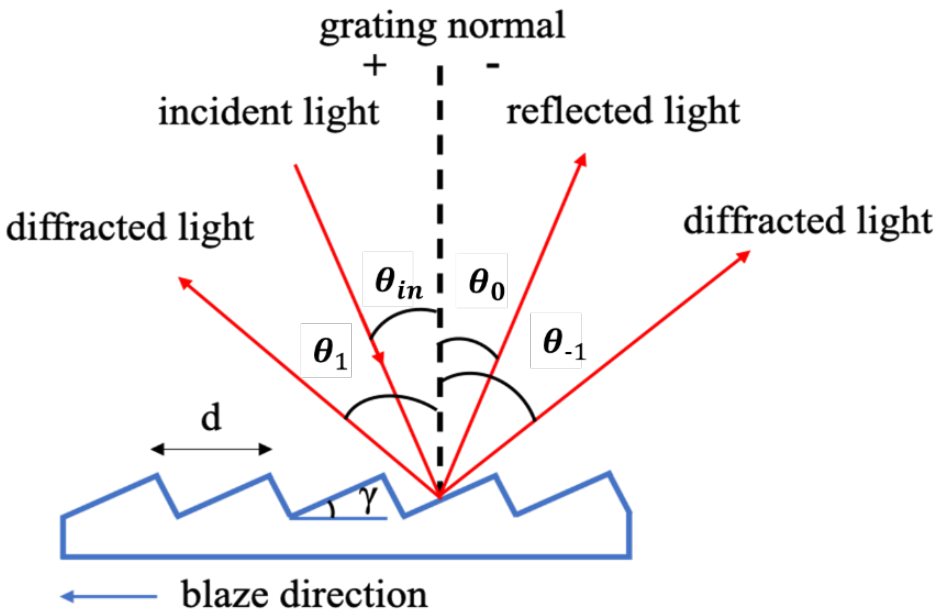

Fig. 3.14. The schematic of a blazed grating.

doi:10.6342/NTU202203086

The dispersion of a grating is governed by the grating equation, usually written as:

$$d(sin\,\theta_{in} + sin\,\theta_m) = m\lambda \tag{3.4}$$

where λ is the diffracted wavelength, m is the order of diffraction, d is the grating constant (the distance between successive grooves), θ_{in} is the angle of incidence measured from the normal and θ_m is the angle of diffraction measured from the normal.

Most energy of diffracted light is concentrated into m-th order light, when it satisfies the condition:

$$\gamma = \frac{\theta_{in}+\theta_m}{2} \tag{3.5}$$

The grating equation can be presented:

$$m\lambda = 2d\sin(\gamma)\cos(\theta_{in}-\gamma) \tag{3.6}$$

If we want the energy of diffracted lights focused on first order diffracted light, it can be designed as Littrow configuration $\gamma = \theta_{in} = \theta_1$.

$$\lambda = 2d\sin(\theta_{in}) \tag{3.7}$$

doi:10.6342/NTU202203086

Chapter 4

Ultra-broadband Wavelength-swept Ti:sapphire Crystal Fiber Laser

We used the green laser diodes (LDs) as the pump sources of Ti-doped sapphire crystal, although the output mode of LD is poor compared to the traditional 532 nm double-frequency solid-state laser. However, it is easy to use and has the potential to simplify the experimental setup. Due to the short fluorescent lifetime and low absorption cross-section of Ti:sapphire crystal, it is difficult to achieve low threshold and high-efficiency output power. In our studies, the waveguide structure of glass-clad crystal fiber (CF) was used to increase the efficiency of the pump and decrease propagation loss. As the result, our previous work successfully produces a lower threshold than the minimum threshold recorded in the literature [39]. This chapter mainly introduces the wavelength-swept laser, and the ultra-broadband swept laser. It is suitable for biological image acquisition and medical diagnoses such as optical coherence tomography (OCT).

4.1 Double 520-nm Laser-diodes Pumped Ti:sapphire Crystal Fiber Laser

In this thesis, the 520-nm LD (NDG7475, Nichia) is used as the pump source. We combined two 520-nm LDs by using the polarizing beamsplitter cube (PBS). In Fig. 4.1, the polarization of LD_1 is P-polarization, and the LD_2 is S-polarization.

In order to maintain the stability of the output power, the LD is placed on the copper holder for heat dissipation, and the silver glue is spread between the LD and the copper holder. The output powers of the LDs are related to the driving current, as shown

doi:10.6342/NTU202203086

in Fig. 4.2. The total pump power of combined LDs is 1814 mW.

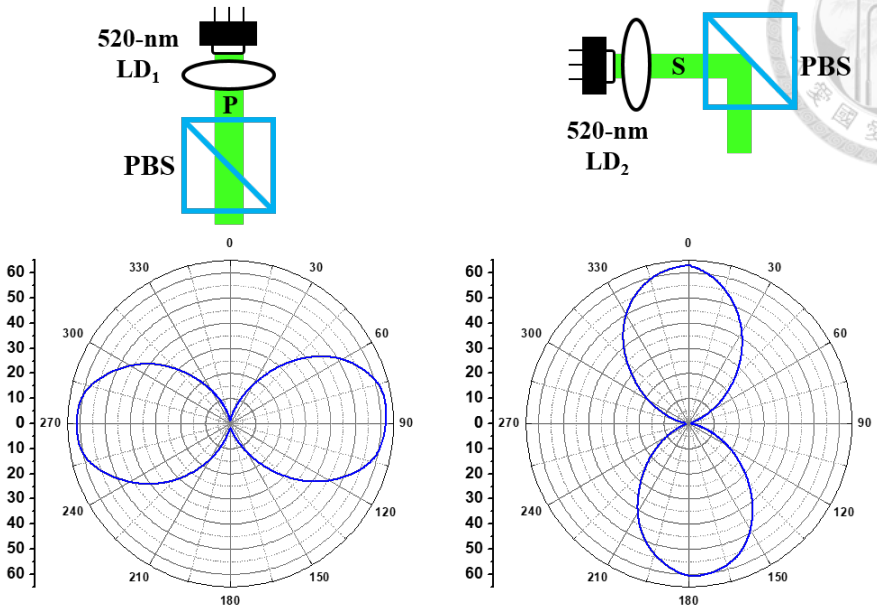

Fig. 4.1. The polarizations of LDs. PBS: polarizing beamsplitter.

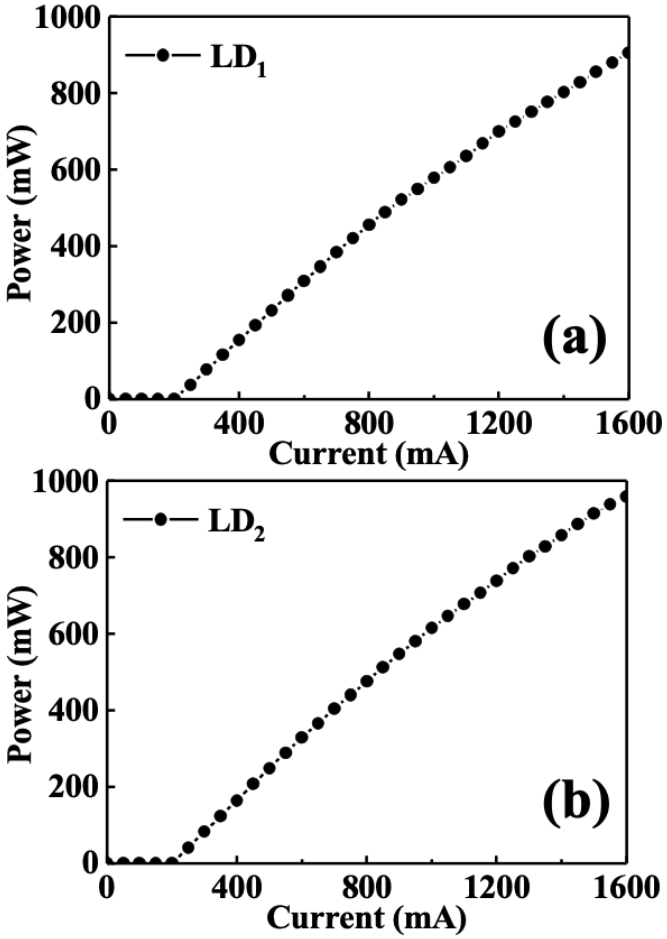

Fig. 4.2. (a) The P-I curve of LD_1. (b) The P-I curve of LD_2.

doi:10.6342/NTU202203086

Figure 4.3 shows the measurement setup for spontaneous emission (SE) power and residual pump power. A high numerical aperture lens (405-G-2, NA=0.6) was used to collimate the pump light. In order to achieve the bidirectional output of CF, the collimated laser light is reflected by a dichroic mirror (Di02-R532, Semrock). An aspherical lens (C392TME-B, NA=0.64, f=2.75 mm, Thorlabs) was used to couple the pump light to a CF and use an aspherical lens (C110TMD-B, NA=0.4, f=6.24 mm, Thorlabs) was used to collimate the SE and residual pump powers.

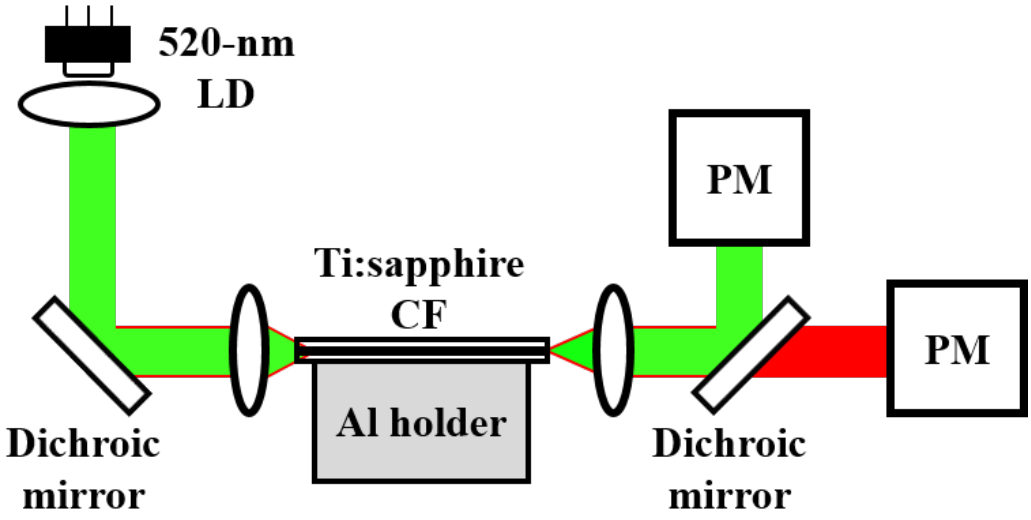

Fig. 4.3. The measurement setup for SE power and residual power. PM: power meter.

Table 4.1 presents the SE power and residual of four different CFs with a pump power of 905 mW. The best length of CF is 2.7 cm. This CF could have the biggest SE power and lower residual pump power. The CF has better absorption of pump power with a fiber length of 3 cm; however, the SE power is weaker because of the larger propagation losses with longer CF.

doi:10.6342/NTU202203086

Table 4.1. SE and residual powers of different Ti:sapphire CFs with a pump power of 905 mW.

	Fiber length (cm)	SE (mW)	Residual pump (mW)	SE efficiency (%)	Residual power (%)
A	3	8.5	20	1.03	2.2
B	2.7	9.6	25.4	1.06	2.8
C	2.4	8.7	34.7	0.96	3.8
D	2	4.12	60	0.45	6.6

doi:10.6342/NTU202203086

4.1.1 Continuous-Wave Ti:sapphire Crystal Fiber Laser with HR-AR Coatings

In order to build up an external-cavity crystal fiber laser, the input end-face of the crystal fiber was deposited with a highly reflective (HR) coating from 700 to 900 nm and the output end-face with anti-reflective (AR) coating from 650 to 1000 nm. The coating layers are SiO_2/TiO_2 stacks deposited by an E-gun deposition system.

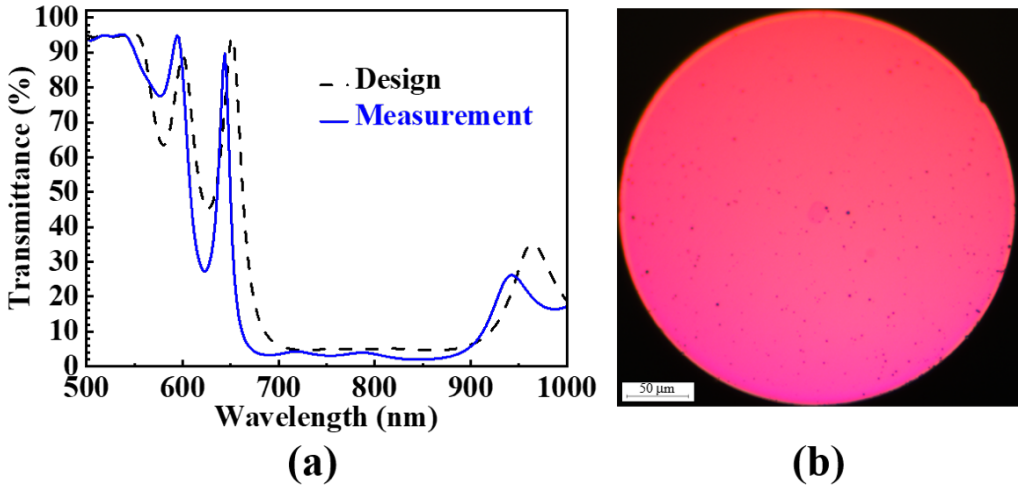

Fig. 4.4. (a) Transmission spectrum of the HR coating. (b) The input end of CF (HR).

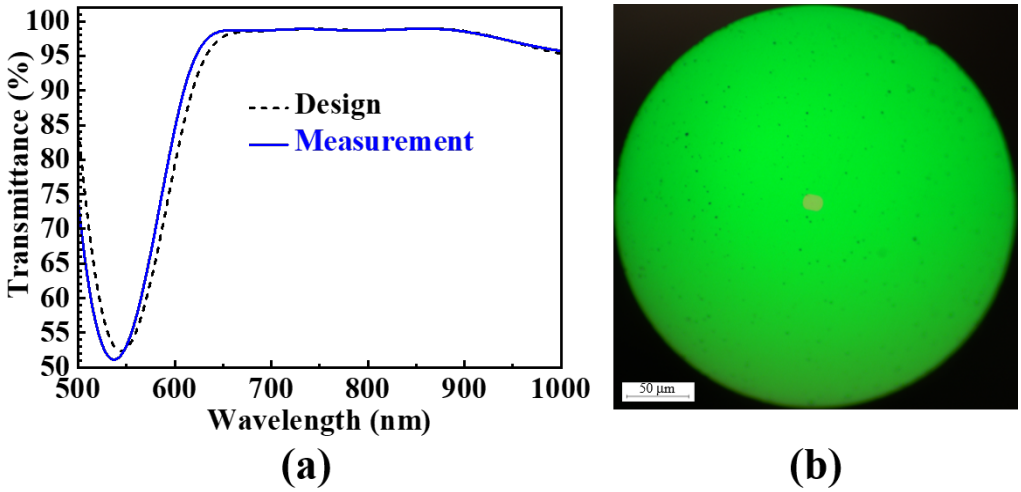

Fig. 4.5. (a) Transmission spectrum of the AR coating. (b) The output end of CF (AR).

doi:10.6342/NTU202203086

The spectra of the HR and AR coating on the CF end-faces are derived from the measured transmission spectra of the test glass plates, as shown in Fig. 4.4(a) and Fig. 4.5(a). The transmission of the HR coating at the 520-nm pump wavelength was as high as 94.9%, and the transmission in the 700 to 900 nm laser operation window was below 5%. The design and measurement of the spectrum have a lateral wavelength shift of about 14 nm, and the transmittance in the signal light band is 1.9~4.2%. The AR coating has a transmittance of 55.4% at 520 nm and above 98.6% in the 700 to 900 nm wavelength range. The microscope photos of the coated fiber end-faces are shown in Fig. 4.4(b) and Fig 4.5(b).

In Fig. 4.6, two 1-W 520-nm LDs (NDG7475, Nichia) were used as the pump light sources and combined by a polarizing beamsplitter cube (PBS). The pump was focused into a tin-packaged glass-clad a-cut Ti:sapphire CF with an aspheric lens (L_1, 5721-B-H, f = 2.8 mm, NA = 0.6, Newport). The length of Ti:sapphire CF is 2.7 cm. At the input end, it was HR coated at 520 nm and high-reflection coated with a broad wavelength coverage of 700 – 900 nm. At the output end, it was AR coated with a transmittance of greater than 98.6% from 700 to 900 nm. The output of the CF was collimated with another aspheric lens (L_2, C110TM D-B, f = 6.24 mm, NA = 0.4, Thorlabs). The output beam profile was recorded with a charge-coupled device (CCD) (STC-TB202USB-AS, Sentech). The lasing spectra were measured using an optical spectrum analyzer (Ocean Optics USB4000 NIR and Anritsu MS9740A) from the backward direction through a dichroic mirror (LPD01-633RS-25, Semrock) that reflected the pump power. Figure 4.7 presents the experimental and simulated results at a 520-nm diode pump, respectively. The threshold power and the slope efficiency were 120 mW and 3.3%, respectively. Table 4.2 presents the parameters of fitted experiment results and simulation.

doi:10.6342/NTU202203086

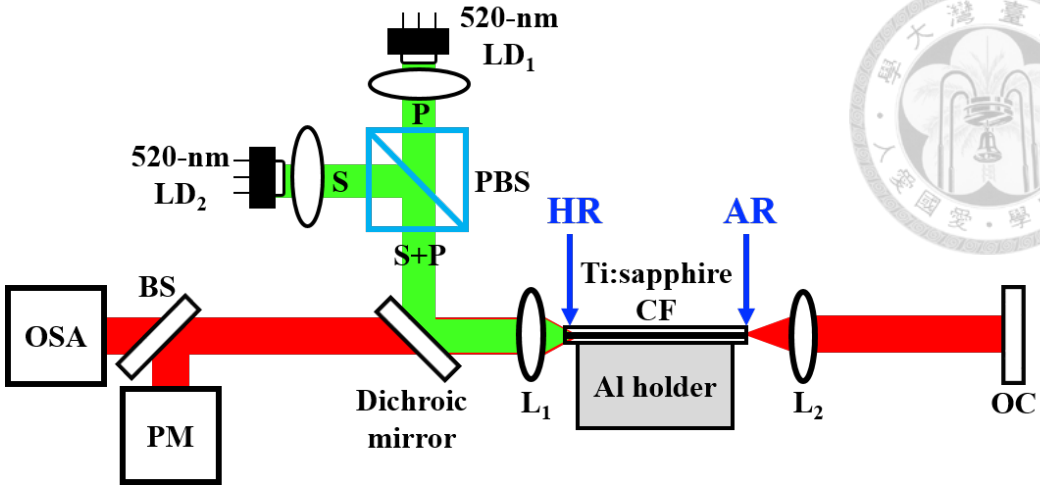

Fig. 4.6. Two 520-nm LDs pumped glass-clad Ti:sapphire CF laser scheme. PM: power meter. OSA: optical spectrum analyzer. BS: beam splitter. PBS: polarizing beamsplitter. OC: output coupler. $L_{1,2}$: aspheric lens.

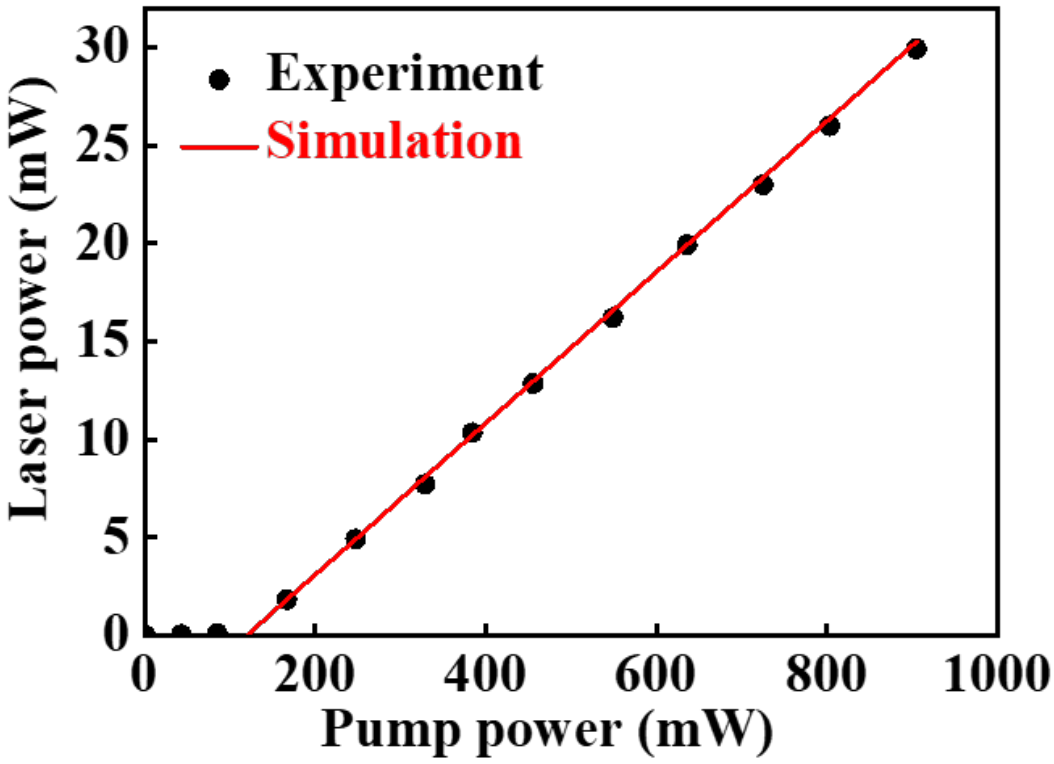

Fig. 4.7. L-I curve of two 520-nm LDs pumped glass-clad Ti:sapphire CF laser with HR-AR coatings.

Figure 4.8 shows the lasing spectrum with a single peak at low pump power. Figure 4.9 shows that the lasing spectrum has multi-peaks at high pump power caused by the

doi:10.6342/NTU202203086

high-order transverse modes and longitudinal modes. The relationship between longitudinal and transverse modes will be discussed in Ch. 5.

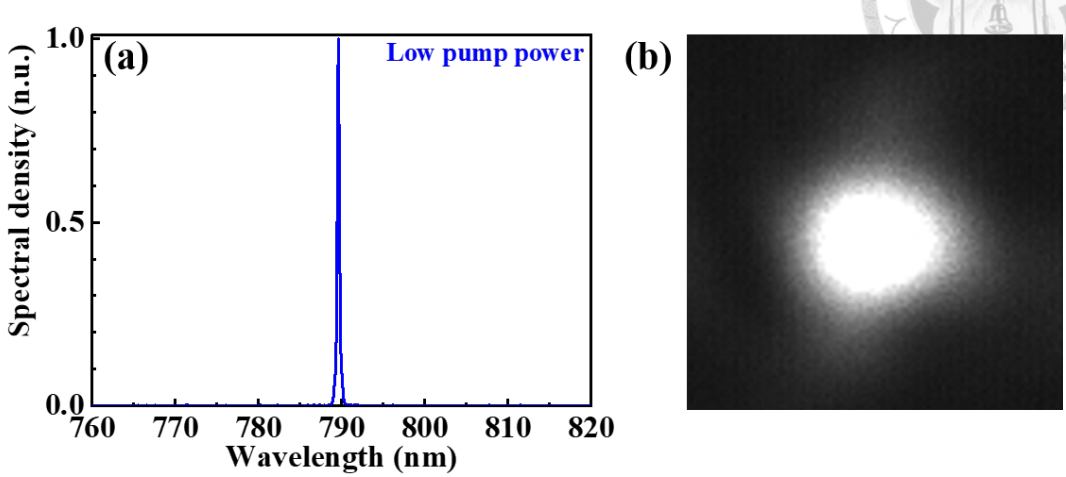

Fig. 4.8. (a) The lasing spectrum with low pump power of 247 mW. (b) fundamental transverse mode of two 520-nm LDs pumped glass-clad Ti:sapphire CF laser.

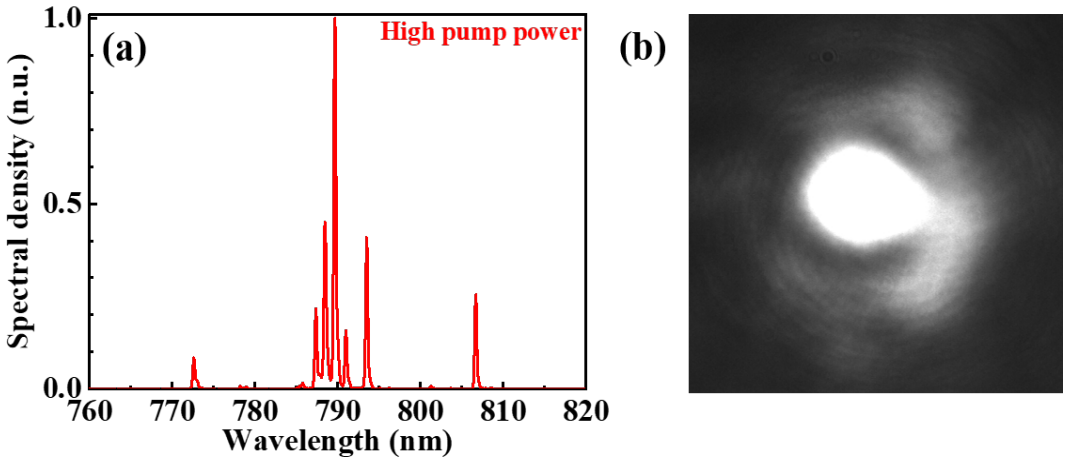

Fig. 4.9. (a) The lasing spectrum with high pump power of 905 mW. (b) high-order transverse modes of Ti:sapphire CF laser with high pump power.

doi:10.6342/NTU202203086

Table 4.2. Simulation parameters of fitted Ti:sapphire CF lasers with HR-AR coatings.

	This work
Absorption cross section at 520 nm (cm^2)	5.7×10^{-20}
Emission cross section at 790 nm (cm^2)	2.4×10^{-19}
Lifetime thermal decay (μs/W)	-0.33
Average fluorescence lifetime (μs)	2.67
Attenuation coefficient at 520 nm (dB/cm)	3.112
Coupling efficiency of CF at 520 nm (%)	88
Propagation loss at lasing wavelength (dB/cm)	0.073
Reflectance of HR coating at lasing wavelength (%)	95.3
Reflectance of OC at lasing wavelength (%)	98
Ti^{3+} doped concentration (wt.%)	0.049

doi:10.6342/NTU202203086

4.1.2 Continuous-Wave Ti:sapphire Crystal Fiber Laser with AR-AR Coatings

In order to comprehensively use our crystal fiber, we also designed anti-reflection coatings on both endfaces of CF, and set up a laser system with two output couplers (OCs).

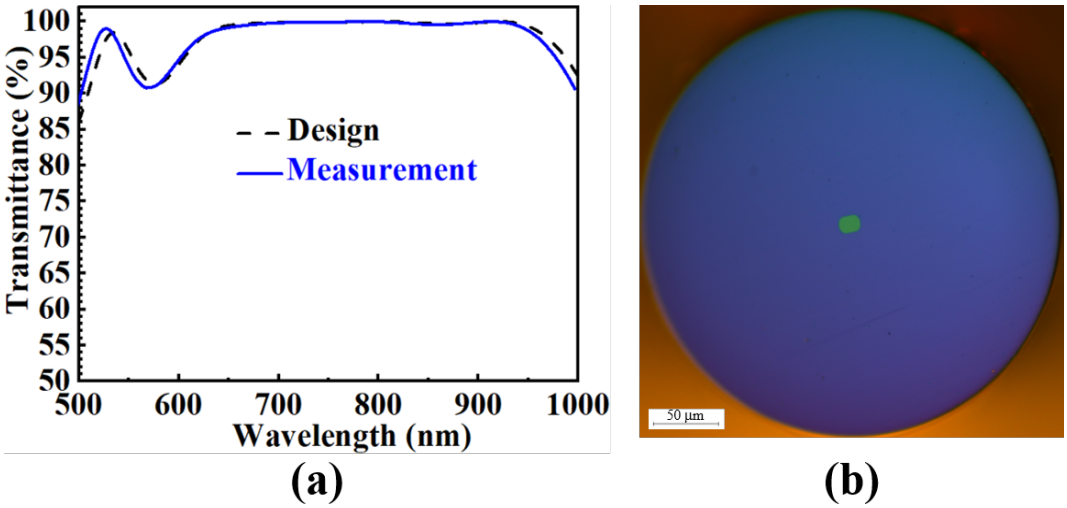

Fig. 4.10. (a) Transmission spectrum of the AR_1 coating. (b) The input end of CF (AR_1).

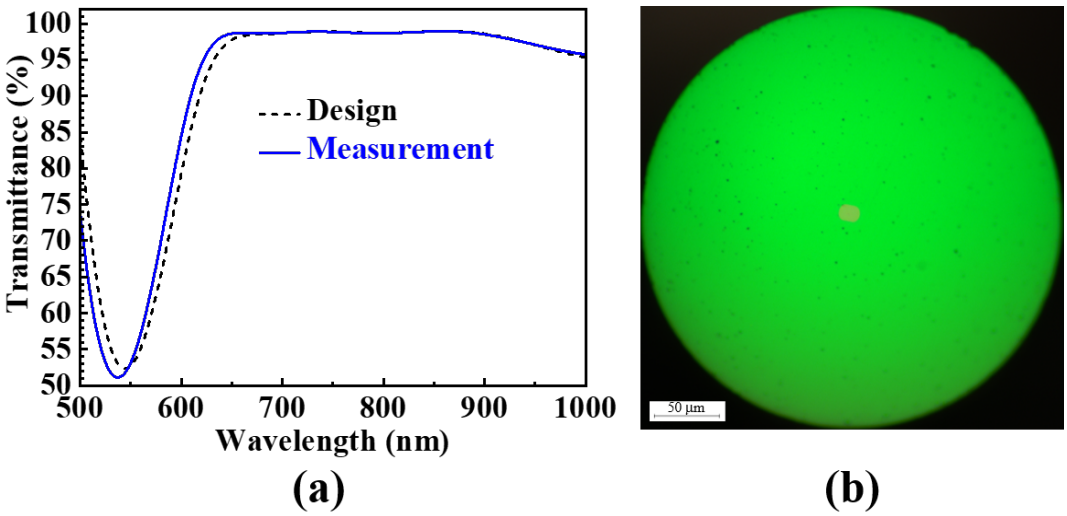

Fig. 4.11. (a) Transmission spectrum of the AR_2 coating. (b) The output end of CF (AR_2).

doi:10.6342/NTU202203086

The spectra of the AR_1 and AR_2 coatings on the CF end-faces are derived from the measured transmission spectra of the test glass plates, as shown in Fig 4.10(a) and Fig. 4.11(a). The transmission of the AR_1 coating in the 520-nm pump wavelength was as high as 99%, and the transmission in the 650 to 950 nm laser operation window was as high as 99%. The AR_2 coating has a transmittance of 55.4% at 520 nm and above 98.6% in the 700 to 900 nm wavelength range. The microscope photos of the coated fiber endfaces are shown in Fig. 4.10(b) and Fig 4.11(b).

In Fig. 4.12, the pump was focused into a Ti:sapphire CF with an aspheric lens (L_1, 5721-B-H, f = 2.8 mm, NA = 0.6, Newport). A 27-mm-long glass-clad Ti:sapphire CF with core diameter at 16 μm was employed as the gain medium, which has a single-pass pump absorption of ~90% at 520-nm pumps. The endfaces of the glass-clad Ti:sapphire CF were dielectric coated (input endface: AR_1; output endface: AR_2). An aspheric lens (L_2, 5723-B-H, f = 6.2 mm, NA = 0.4, Newport) was used to collect the CF output. A16× aspheric lens (L_3, 5726-B-H, f = 15.4 mm, NA = 0.16, Newport) was used to achieve mode matching with the OC_1. A 16× aspheric lens (L_4, 5726-B-H, f = 15.4 mm, NA = 0.16, Newport) is used to collect and collimate the laser output for measurement. The threshold of 274 mW is shown in Fig. 4.13. In order to form a resonant cavity, an additional lens and a mirror need to be added on the left side of the laser system, so the threshold of the laser is increased. However, such a system opens up more possibilities for future research, such as spatial filtering using single-mode fibers and fiber-ring lasers. Table 4.3 presents the parameters of fitted experiment results and simulation.

doi:10.6342/NTU202203086

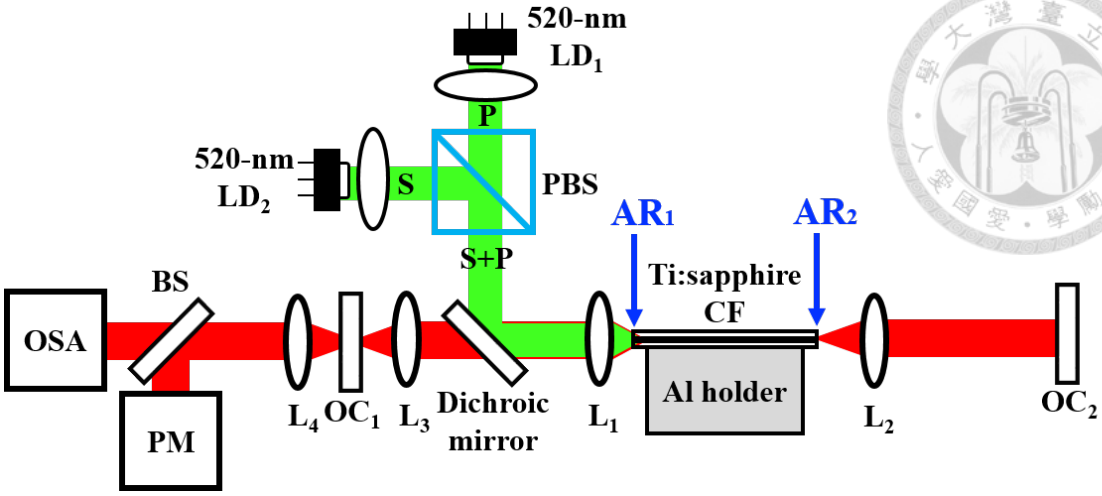

Fig. 4.12. Two 520-nm LDs pumped glass-clad Ti:sapphire CF laser with AR-AR coatings. OSA: optical spectrum analyzer. BS: beam splitter. PBS: polarizing beamsplitter. $OC_{1,2}$: output coupler. $L_{1,2,3,4}$: aspheric lens.

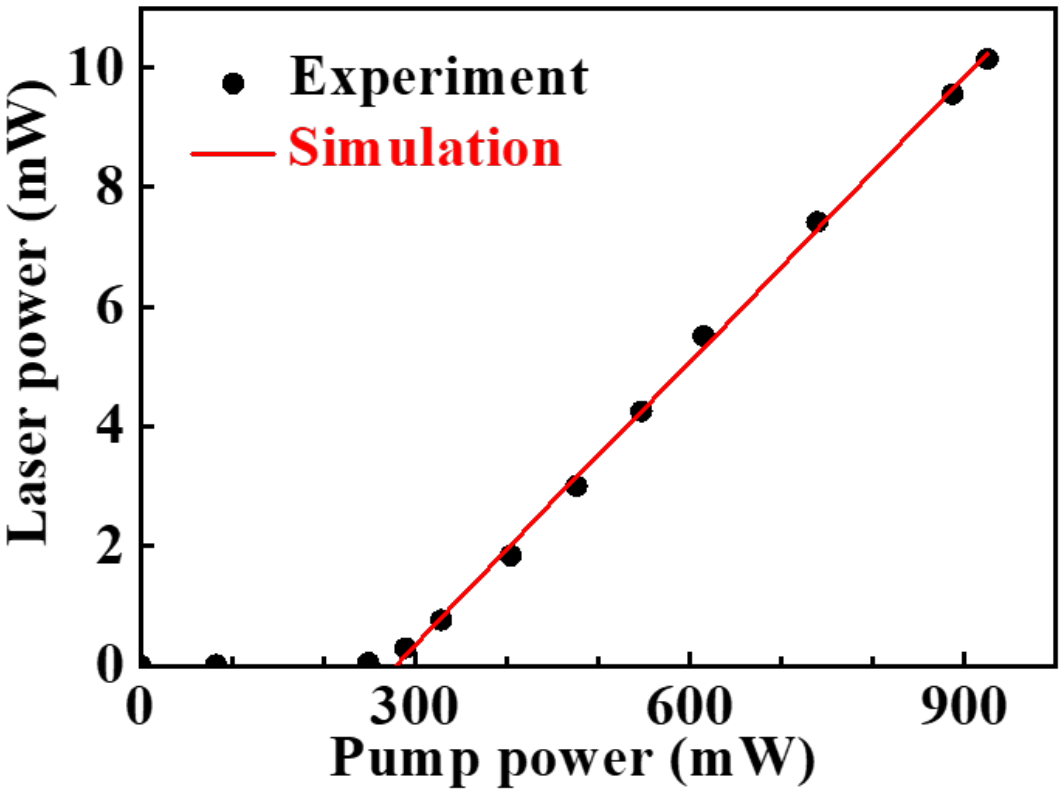

Fig. 4.13. L-I curve of two 520-nm LDs pumped glass-clad Ti:sapphire CF laser with AR-AR coatings

doi:10.6342/NTU202203086

Table 4.3. Simulation parameters of fitted Ti:sapphire CF lasers with AR-AR coatings.

	This work
Absorption cross section at 520 nm (cm^2)	5.7×10^{-20}
Emission cross section at 790 nm (cm^2)	2.4×10^{-19}
Lifetime thermal decay (μs/W)	-0.33
Average fluorescence lifetime (μs)	2.67
Attenuation coefficient at 520 nm (dB/cm)	3.112
Coupling efficiency of CF at 520 nm (%)	88
Propagation loss at lasing wavelength (dB/cm)	0.073
Reflectance of OC_1 at lasing wavelength (%)	98
Reflectance of OC_2 at lasing wavelength (%)	98
Ti^{3+} doped concentration (wt.%)	0.049

doi:10.6342/NTU202203086

4.2 Laser-diode Pumped Wavelength-tuning Ti:sapphire Crystal Fiber Laser with Grating

Figure 4.14 shows the experimental setup of the tunable laser with a diffraction grating, which is similar to the aforementioned setup, except that the output coupler is replaced by the blazed grating (53004BK02-351R, Richardson Grating). The polarization (short axis, c-axis) of the laser beam entering the cavity is the S-polarization of the grating. The diffraction grating used in this experiment is a plane ruled grating designed for use in the Littrow configuration, which means the 1st order diffraction light goes back in the direction reversed to the incident light. The grating has 600 grooves per mm and the area is 30×30 mm. The diffraction efficiency provided by the manufacturer is shown in Fig. 4.15. The diffraction grating was mounted with its groove in the vertical direction so that the intra-cavity laser beam was TM-polarized. The wavelength tuning was accomplished by rotating the grating in the table plane. The measured output power at the peak wavelength of 800 nm is shown in Fig. 4.16. The slope efficiency is 0.61% and the threshold pump power is 320 mW. Table 4.4 presents parameters of fitted experiment results and simulation. The wavelength tuning spectrum recorded by the "maximum hold" function of the optical spectrum analyzer is shown in Fig. 4.17. The wavelength-tuning Ti:sapphire CF laser has a tunable bandwidth of 260 nm (from 680 nm to 940 nm). Table 4.5 shows that this study successfully improved the tuning bandwidth to 260 nm.

doi:10.6342/NTU202203086

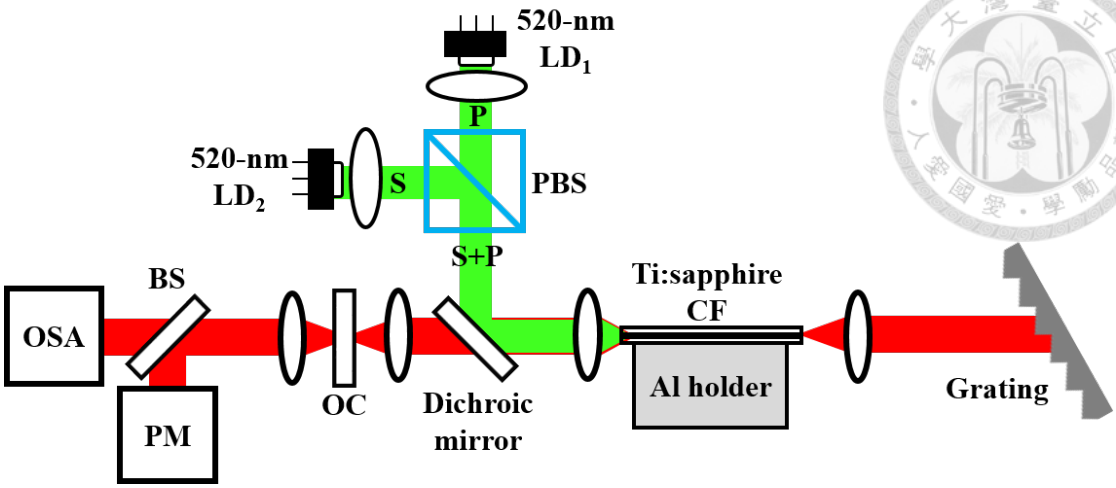

Fig. 4.14. Schematic of the LD-pumped tunable glass-clad Ti:sapphire CF laser with a Littrow-mounted blazed grating. BS: beam splitter. PBS: polarizing beamsplitter. PM: power meter; OSA: optical spectrum analyzer. OC: output coupler.

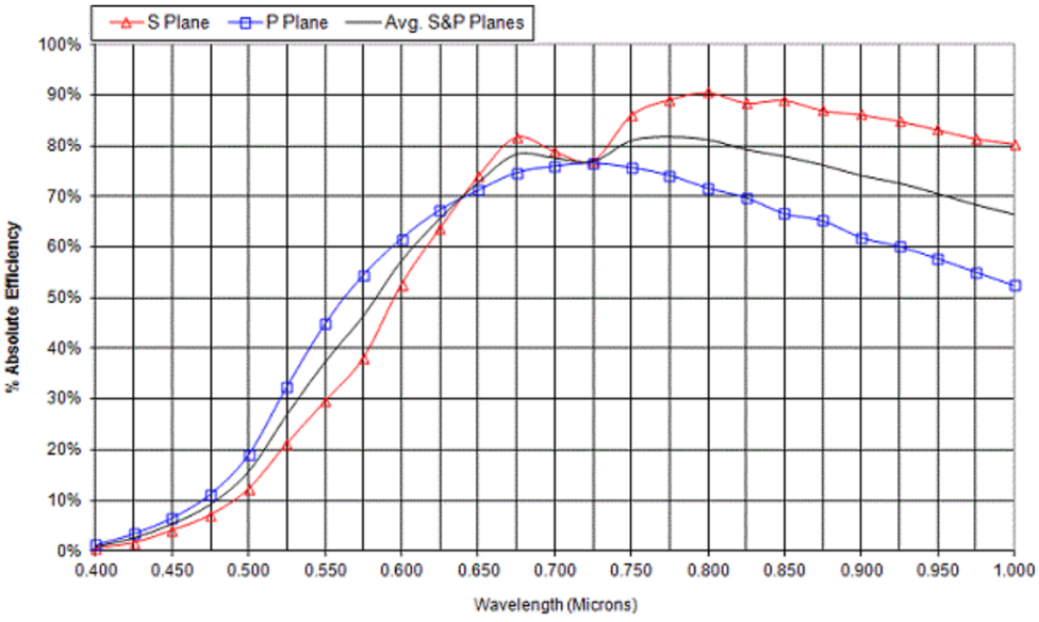

Fig. 4.15. The diffraction efficiency of the grating [98].

doi:10.6342/NTU202203086

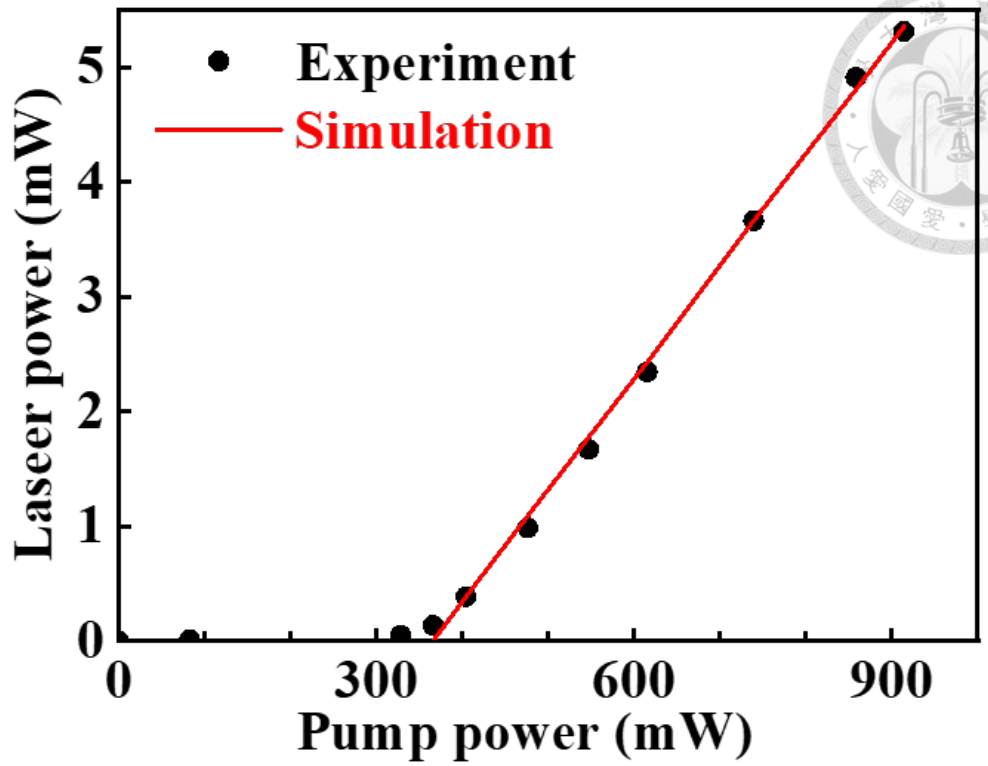

Fig. 4.16. L-I curve of wavelength-tuning Ti:sapphire CF laser with AR-AR coatings.

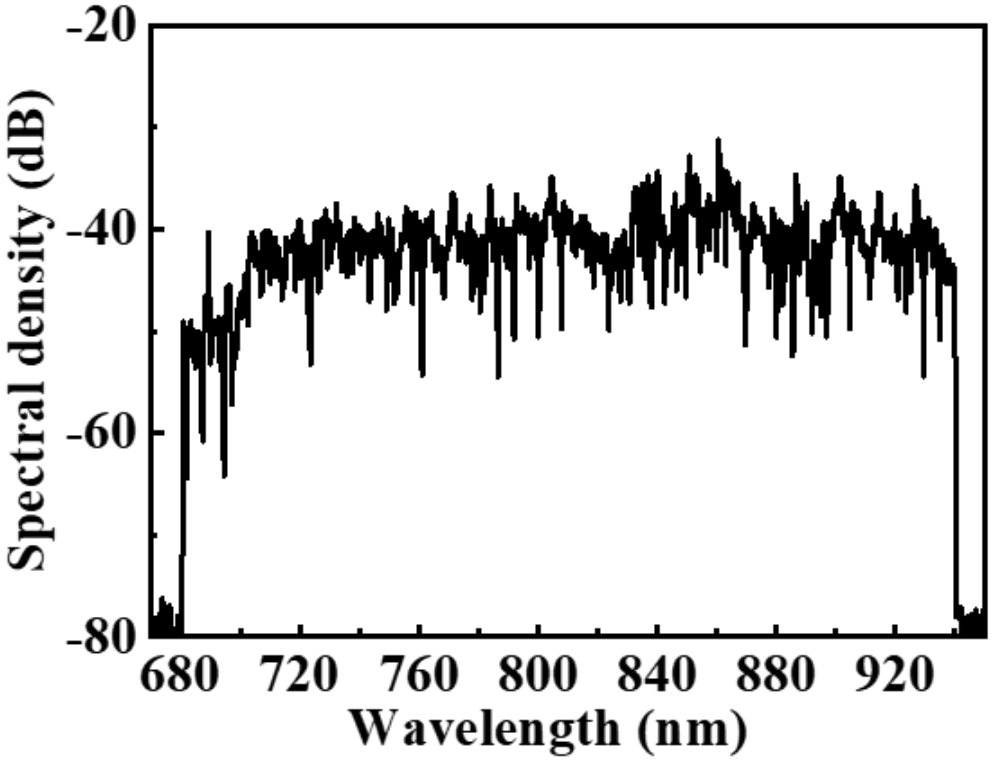

Fig. 4.17. The lasing spectrum of wavelength-tuning Ti:Sapphire CF laser.

doi:10.6342/NTU202203086

Table 4.4. Simulation parameters of fitted wavelength-tuning Ti:sapphire CF lasers with AR-AR coatings.

	This work
Absorption cross section at 520 nm (cm^2)	5.7×10^{-20}
Emission cross section at 790 nm (cm^2)	2.4×10^{-19}
Average fluorescence lifetime (μs)	2.67
Attenuation coefficient at 520 nm (dB/cm)	3.112
Coupling efficiency of CF at 520 nm (%)	88
Propagation loss at lasing wavelength (dB/cm)	0.073
Reflectance of OC at lasing wavelength (%)	98
Ti^{3+} doped concentration (wt.%)	0.049
Reflectance of blazed grating at 1st order (%)	88

Table 4.5. Comparison of wavelength-tuning Ti:sapphire lasers.

	This work	Previous work [99]	C. Grivas et al. [91]	J. F. Pinto et al.[59]
Gain medium	CF	CF	Channel waveguide	Bulk
Ti^{3+} doping concentration (wt.%)	0.049	0.0342	0.12	0.1
Threshold (mW)	320	421	200	750
Pump power (mW)	1600	1525	1000	5000
Tuning range (nm)	**260**	190.86	170	190

doi:10.6342/NTU202203086

4.3 Ultra-broadband Wavelength-swept Ti:sapphire Crystal Fiber Laser with Galvo Mirror

WSL is a new type of pulsed laser. It is neither a time-domain mode-locked laser nor a Q-switched laser. The pulses have different output wavelengths, unlike traditional pulsed lasers, each pulse in the time domain contains all wavelengths. The pulse time interval of the WSL is related to the modulation mechanism and the characteristics of the laser cavity. The output changes under different pump powers, followed by the analysis of the experimental results of the WSL.

The wavelength-swept Ti:sapphire crystal-fiber laser is shown in Fig. 4.18. After the collimating lens, a galvo scanner (GVS001, Thorlabs) and a Littrow-configuration diffraction grating (53004BK02-351R, 600 grooves/mm, Newport) were used as the wavelength selector. The collimated laser beam was reflected to the diffraction grating by the galvo scanner, and the 1st-order diffracted beam was directed back to the Ti:sapphire CF. The wavelength-selected laser passes through CF, dichroic mirror (DM), and output coupler (OC) with 2% reflectance. The emission spectra were monitored by an optical spectrum analyzer (MS9740A, Anritsu) and the laser temporal dynamics was measured by a photodiode (PDA36A, Thorlabs). The total cavity length from grating to OC is about 20 cm.

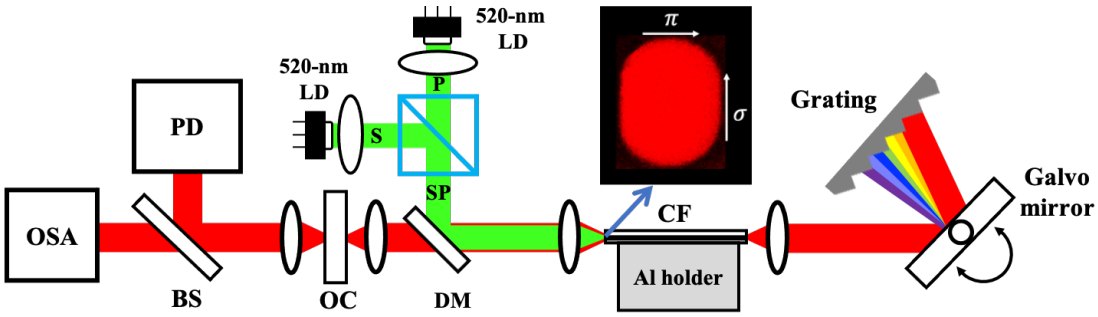

Fig. 4.18. Experimental setup of wavelength-swept Ti:sapphire CF laser [40].

With increasing tuning repetition rates from 10 Hz to 1200 Hz, the laser was able

doi:10.6342/NTU202203086

to maintain a broadband tuning range around 250 nm with no apparent trade-off between tuning range and repetition rate, as shown in Fig. 4.19. This means that the 1.6-W pump power could provide enough gain to compensate the population inversion loss up to at least 1200 Hz, which was limited by the Galvo rotation speed. However, the WSL output power decreases at high tuning speed because the laser built-up time decreases as the tuning speed increases. The laser output power of WSL is shown in Fig. 4.20. Figure 4.21 shows the measured instantaneous linewidth of the WSL. After deconvolution, it was 0.018 nm, which corresponds to a 3-dB coherence roll-off of 7 mm.

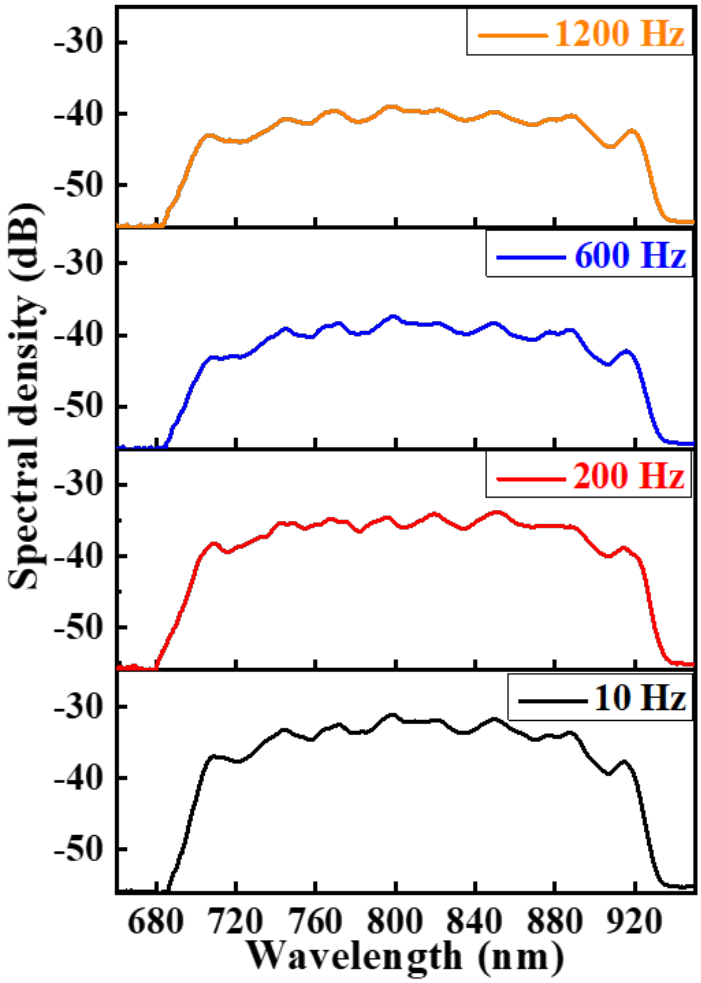

Fig. 4.19. The spectra of WSL at different repetition rates [40]. The WSL spectra were recorded using the “maximum hold” function of the OSA.

doi:10.6342/NTU202203086

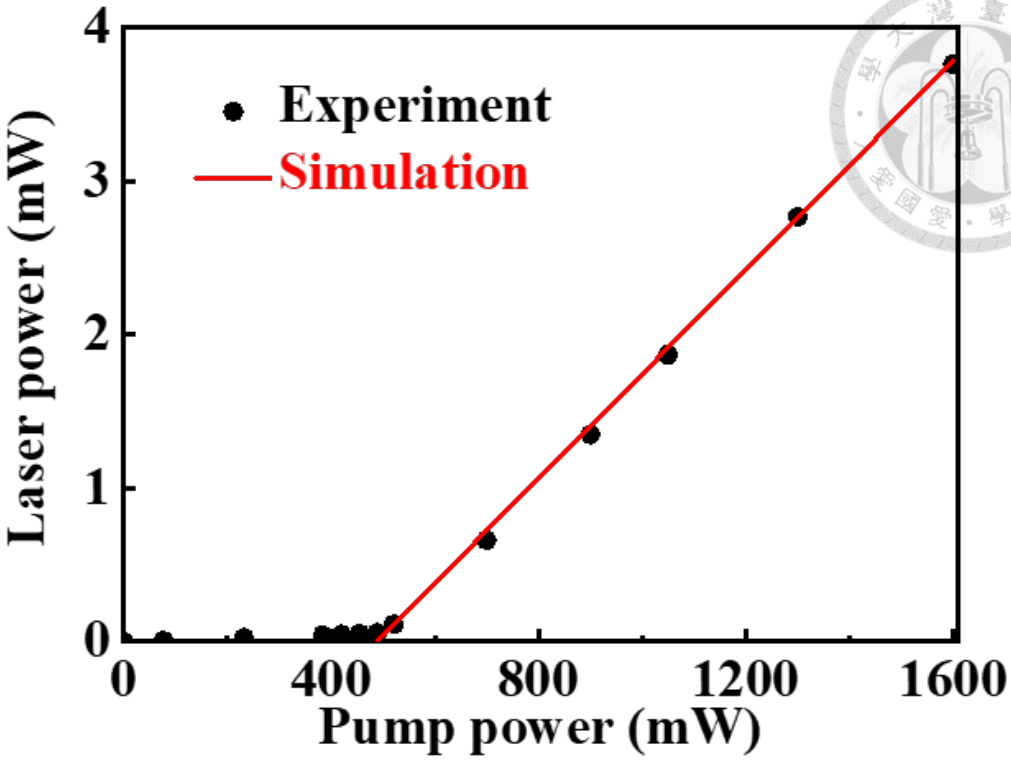

Fig. 4.20. The L-I curve of WSL by two 520-nm LDs pumping [40].

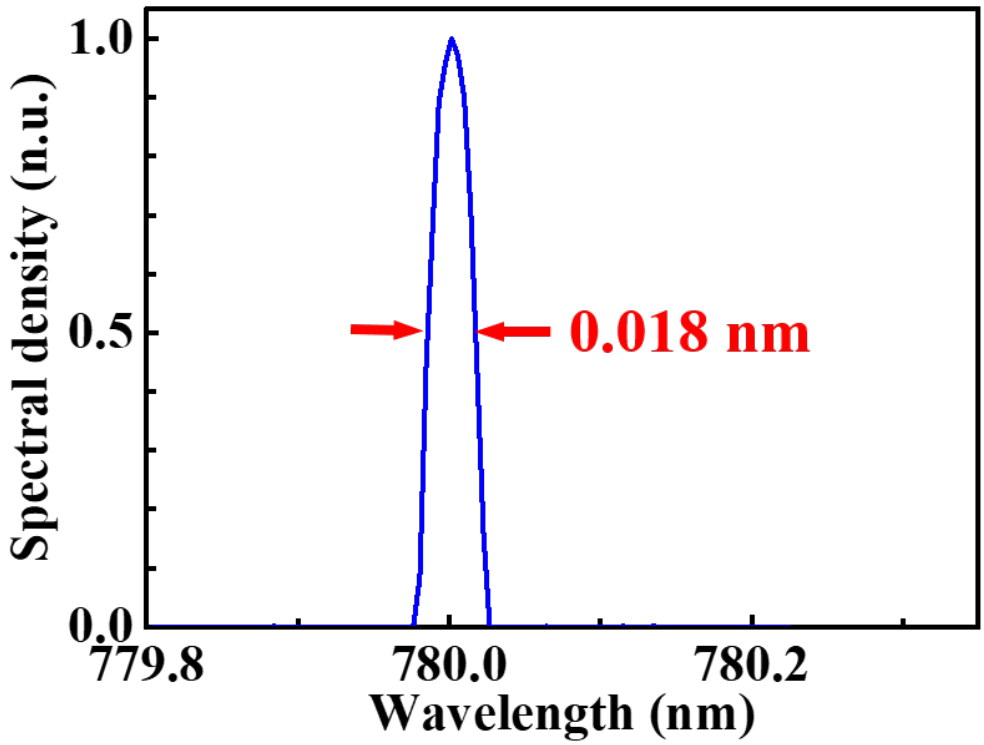

Fig. 4.21. The measured instantaneous linewidth of WSL [40].

doi:10.6342/NTU202203086

To study the swept laser steady-state performance, a distributed glass-clad Ti:sapphire CF model was utilized to fit the experimental result [100]. Considering the input face of the Ti:sapphire CF is at z=0, the distributed pump power, $P_p(z)$, and signal power, $P_s(z)$, can be expressed as

$$\pm\frac{dP_p^{\pm}(z)}{dz} = -\left[\Gamma_p N_g(z)\sigma_a + \alpha_{pl}^p\right] P_p^{\pm}(z), \tag{4.1}$$

$$\pm\frac{dP_s^{\pm}(\lambda_k,z)}{dz} = \left[N_2(z)\Gamma_s\sigma_e - \alpha_{pl}^s\right]P_s^{\pm}(\lambda_k,z) + N_2(z)A_{core}S_{sp}(\lambda)\Delta\lambda_k, \tag{4.2}$$

where $N_g(z)$ and $N_2(z)$ are the electron densities of the ground and excited states, respectively. σ_a and σ_e represent the absorption and emission cross-sections, respectively. α_{pl}^s and α_{pl}^p are the propagation losses at the signal and pump wavelengths, respectively. Γ_p and Γ_s are the pump and signal confinement factors, respectively. A_{core} is the core area of the Ti:sapphire CF. λ is the wavelength. $\Delta\lambda_k$ is the width of the ith wavelength slot centered at λ_k. The single-mode spectral power density of the spontaneous emission [101] can be expressed as,

$$S_{sp}(\lambda) = \frac{2hc^2}{\lambda^3 A_{core}}\sigma_e(\lambda). \tag{4.3}$$

where h is the Planck's constant. c is the speed of light in vacuum. σ_a is $5.7\times10^{-20}\text{cm}^2$, σ_e is $2.4\times10^{-19}\text{cm}^2$, α_{pl}^p is 0.26 dB/cm, and α_{pl}^s is 0.045 dB/cm. As shown in Fig. 4.20, the simulation result agrees well with the experiment. The simulation parameters are listed in Table 4.6. A pump coupling efficiency of 93% was obtained. The roundtrip loss of the laser cavity was 35.7% (1.93 dB). The highest gain coefficient of the Ti:sapphire CF is 0.7 cm^{-1}.

doi:10.6342/NTU202203086

Table 4.6. Loss of wavelength-swept Ti:sapphire CF laser [40].

Component/parameter	Loss (dB)	Loss (%)
Coupling efficiency of CF	0.31	7
Propagation losses of CF	0.14	3
Galvo mirror reflectance	0.18	4
Grating diffraction	0.56	12
Dichroic mirror reflectance	0.6	13
Lens	0.05	1
Output coupler transmission	0.09	2
Total roundtrip loss	1.93	35.7

To study the swept laser dynamics, the galvo mirror was operated at a 600-Hz frequency, which corresponds to a 1.2-kHz laser repetition rate, ± 0.6 V sinusoidal voltage driving, as shown in Fig. 4.22(a). The WSL pulsed behavior can clearly be seen in Fig. 4.22(b). It is associated with the low signal gain so that the laser build-up time cannot keep up with the wavelength sweeping by the galvo-grating configuration. Figure 4.22(c) shows the temporal output of the WSL at a pump power of 1.6 W with a repetition rate of 1.2 kHz.

doi:10.6342/NTU202203086

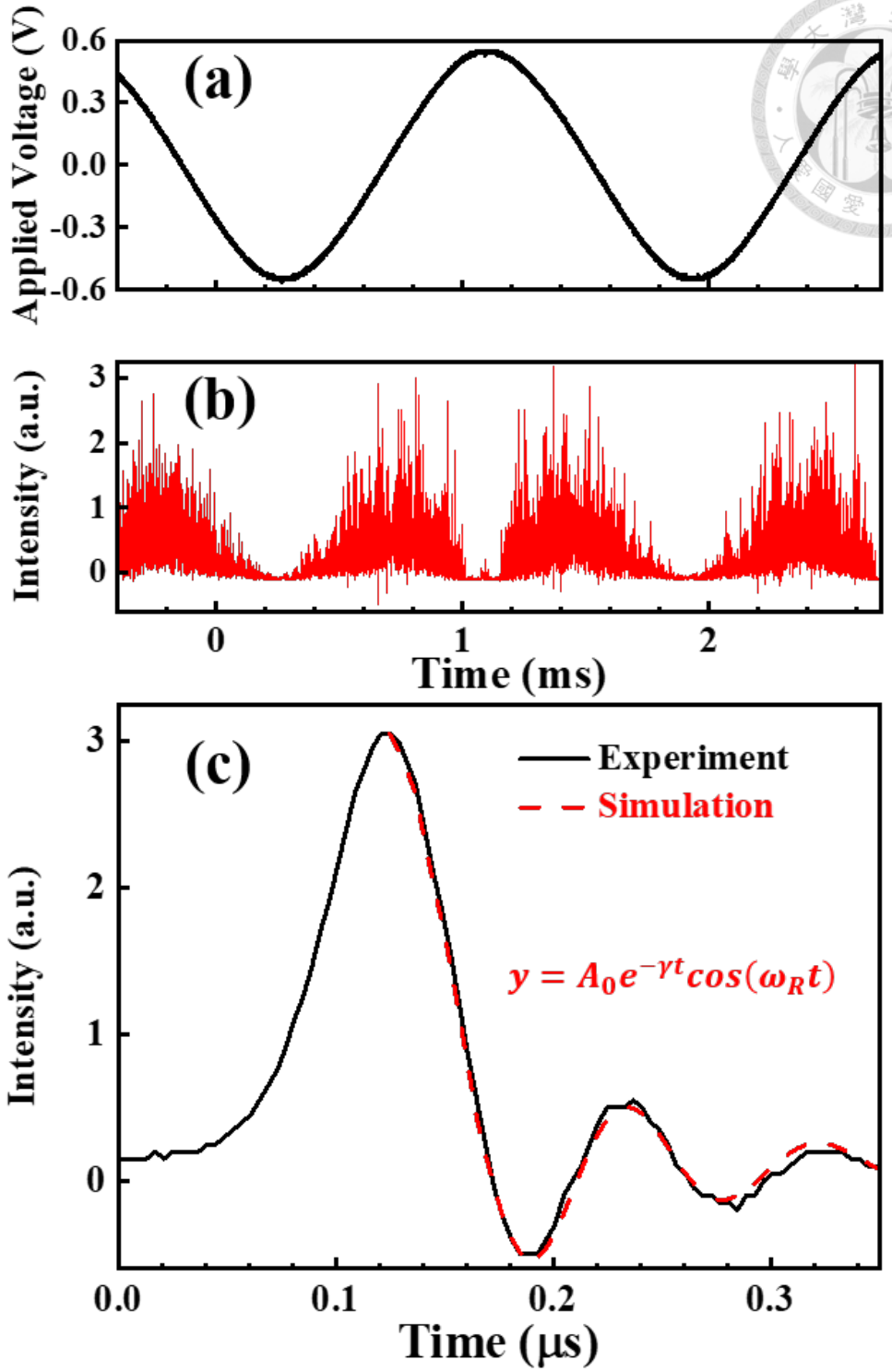

Fig. 4.22. (a) The applied voltage for galvo mirror, (b) The signal of wavelength-swept laser with 250-nm bandwidth, and (c) Extend and fit the signal of the wavelength-swept laser [40].

doi:10.6342/NTU202203086

The pulsed laser exhibits an oscillating tail with an 11.09-MHz frequency. Since the oscillating and trailing tail was a result of relaxation oscillation of the Ti:sapphire CF, the small-signal perturbation approach was used to obtain the internal carrier properties [102]. The complex relaxation oscillation frequency, S, can be expressed as

$$s = \frac{-r}{2\tau_f} \pm j\sqrt{\frac{r-1}{\tau_c\tau_f} - \left(\frac{r}{2\tau_f}\right)^2}, \tag{4.4}$$

where r is the ratio between the pump power and threshold power. τ_c is the photon lifetime, from which the cavity roundtrip time above cavity roundtrip loss can be approximated. The frequency of the damped sinusoid is the relaxation oscillation frequency, ω_R, which is then given by

$$\omega_R = \sqrt{\frac{r-1}{\tau_c\tau_f} - \left(\frac{r}{2\tau_f}\right)^2}. \tag{4.5}$$

As shown in Fig. 4.22(c), at a pump power of 1.6 W, the measured pulse damping behavior agrees well with the simulation. τ_f = 2.67 μs and r = 3.2 were used to fit Eqs. (4.4) and (4.5). The relaxation oscillation frequency increases at higher pump powers as shown in Fig. 4.23. And, the total roundtrip loss estimated based on the pulse dynamics is also consistent with that obtained from the steady-state rate equation fitting in Fig. 4.20. As mentioned earlier, the tuning speed is mainly limited by the galvo mirror. The number of pulses within the WSL comb-like spectra is dictated by the Ti:sapphire gain.

doi:10.6342/NTU202203086

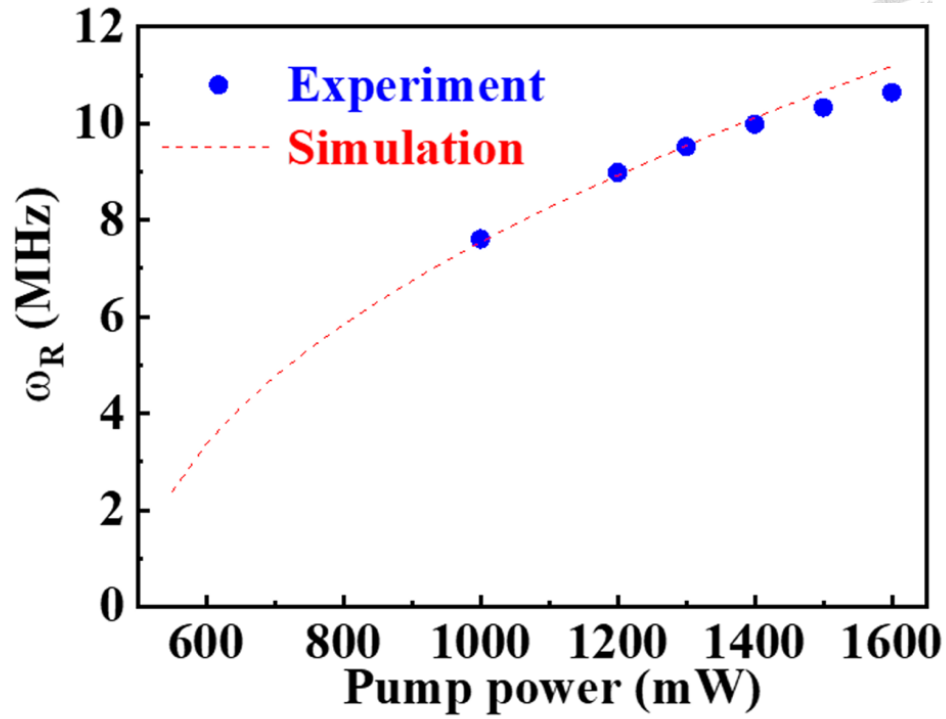

Fig. 4.23. Measure and fit the relaxation oscillation frequency of the wavelength-swept laser [40].

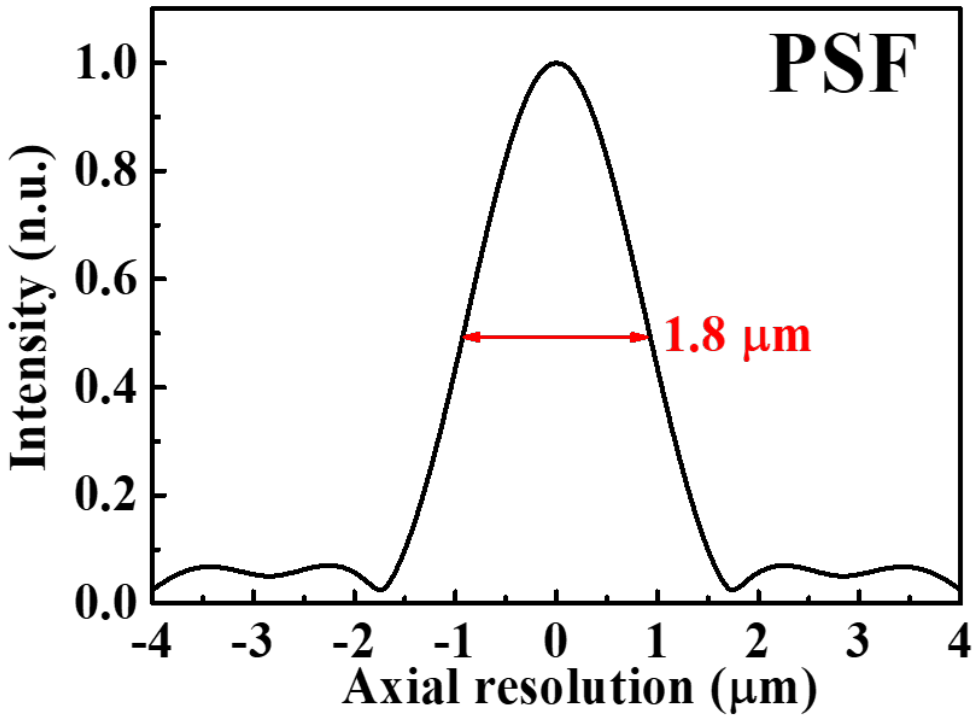

Fig. 4.24. The point spread function of wavelength-swept laser based SS-OCT [40].

doi:10.6342/NTU202203086

When using the Ti:sapphire swept laser as the light source of SS-OCT, the calculated PSF is shown in Fig. 4.24. The estimated axial resolution is 1.8 μm in air, which reveals our WSL could provide cellular resolution. The PSF side lobes are less than 10% (0.46 dB), which indicates low axial image pixel crosstalk. At a sweeping wavelength speed of 300 nm/ms with a repetition rate of 1200 Hz, the 0.018-nm instantaneous linewidth of the Ti:sapphire swept laser can achieve a 3-dB sensitivity roll-off of 7 mm.

4.4 Modeling of Wavelength-swept Ti:sapphire Crystal Fiber

The WSL in this study by using galvo mirror to change the incident angle of light on the grating, so different wavelengths can be output at different times. Each lasing laser starts to grow from small signal. In order to simulate the characteristics of the wavelength changing with time in the WSL, the time differential term is added in Eq. (4.1) and (4.2), the following expressions for the WSL:

$$\pm\left[\frac{\partial P_p^{\pm}(\lambda_k,z,t)}{\partial z} \pm \frac{n}{c}\frac{\partial P_p^{\pm}(\lambda_k,z,t)}{\partial t}\right] = -\left[\Gamma_p N_g(z,t)\sigma_a(\lambda_k) + \alpha_{pl}^{p}\right]P_p^{\pm}(\lambda_k,z,t), \tag{4.6}$$

$$\pm\left[\frac{\partial P_s^{\pm}(\lambda_k,z,t)}{\partial z} \pm \frac{n}{c}\frac{\partial P_s^{\pm}(\lambda_k,z,t)}{\partial t}\right]$$

$$= \left[N_2(z,t)\Gamma_s\sigma_e(\lambda_k) - \alpha_{pl}^{s}\right]P_s^{\pm}(\lambda_k,z) + 2N_2(z,t)A_{core}S_{sp}(\lambda_k)\Delta\lambda_k, \tag{4.7}$$

where $N_g\ (z)$ and $N_2\ (z)$ are the electron densities of the ground and excited states, respectively. σ_a and σ_e represent the absorption and emission cross-sections, respectively. α_{pl}^{s} and α_{pl}^{p} are the propagation losses at the signal and pump wavelengths, respectively. Γ_p and Γ_s are the pump and signal confinement factors, respectively. A_{core} is the core area of the Ti:sapphire CF. λ is the wavelength. $\Delta\lambda_k$ is the width of the ith wavelength slot centered at λ_k.

doi:10.6342/NTU202203086

$$\frac{dN_2(z,t)}{dt} = N_0(z,t)R_{03}(z,t) - N_2(z,t)\left[W_{21}(\lambda_k,z,t) + \frac{1}{\tau_f}\right]. \quad (4.8)$$

where R_{03} is the transition probability of the ground state absorption, and W_{21} is the transition probability stimulated emission at λ_k.

In the area where the laser threshold is relatively large, the time interval between two adjacent pulses is longer. In time domain, the time interval of adjacent pulses was affected by parameters such as laser threshold, half-width of grating filter, population inversion, spontaneous emission power spectral density, and stimulated transition probability. At a high repetition rate, the low gain coefficient of Ti^{3+} limits the number of lasing peaks within the tuning wavelength range. Eventually, the laser built-up time will limit the maximum repetition rate. In Fig. 4.25, the pulse time interval of WSL becomes larger as the repetition rate increases. Using WSL simulation, the pulse time intervals of WSL with different wavelengths are shown in Fig. 4.26. Since the gain of Ti:sapphire is a Gaussian distribution, the time interval of lasing wavelength, which is close to the center wavelength is shorter due to the higher gain. However, the time interval of lasing wavelength, which is far away from the center wavelength is longer due to the lower gain. Table 4.7 presents the parameters of fitted experiment results and simulation.

doi:10.6342/NTU202203086

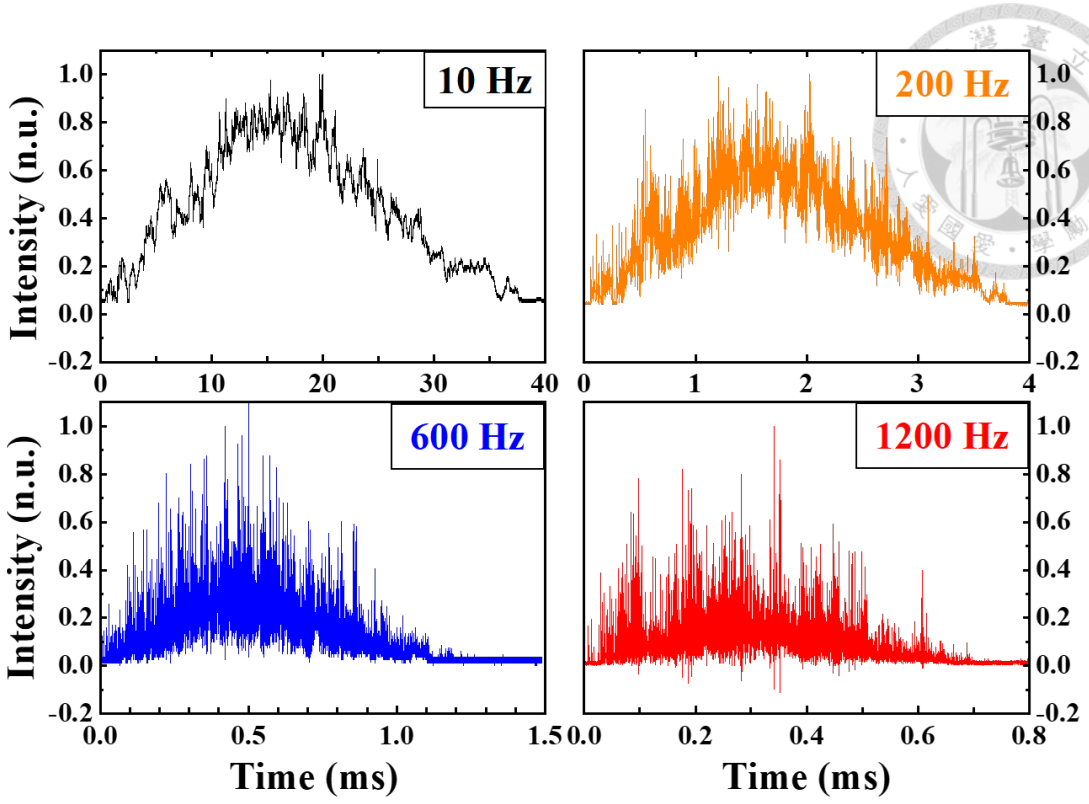

Fig. 4.25. The oscilloscope signals of WSL with different repetition rates.

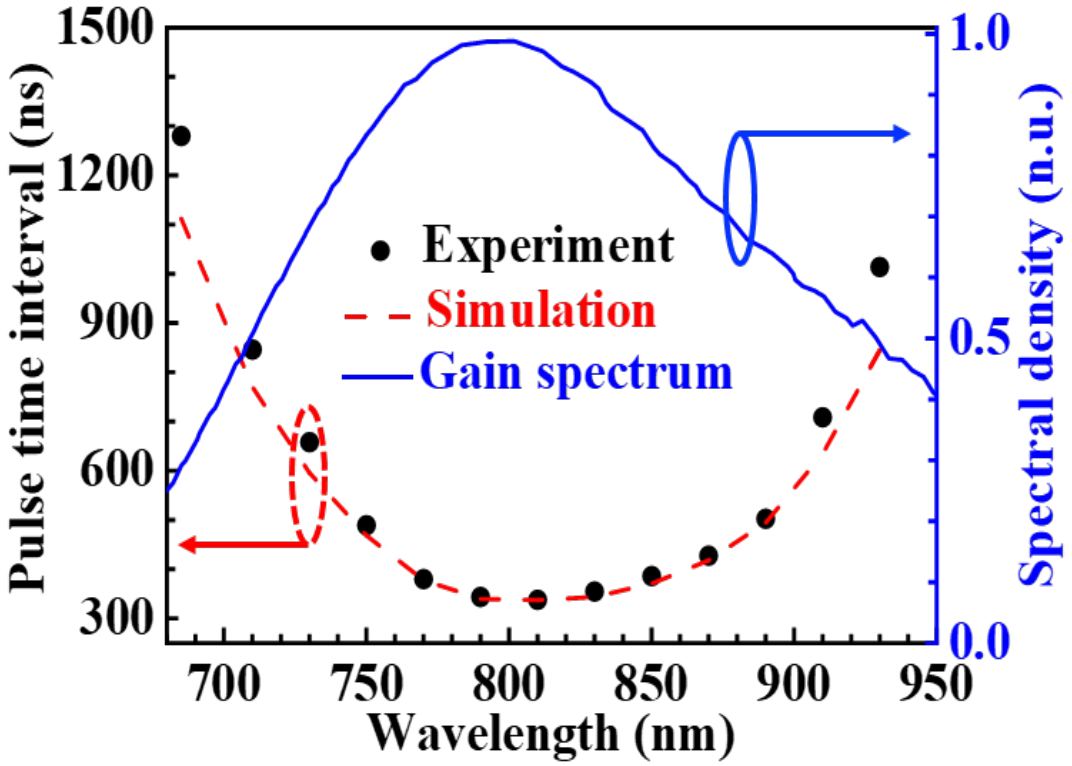

Fig. 4.26. The pulse time interval of WSL with different wavelengths.

doi:10.6342/NTU202203086

Table 4.7. Simulation parameters of fitted wavelength-swept Ti:sapphire CF lasers.

	This work
Tuning range (nm)	680~940
Absorption cross-section at 520 nm (cm^2)	5.7×10^{-20}
Emission cross section at 790 nm (cm^2)	2.4×10^{-19}
Lifetime decay (μs/W)	-0.33
Average fluorescence lifetime (μs)	2.67
Attenuation coefficient at 520 nm (dB/cm)	3.112
Coupling efficiency of CF at 520 nm (%)	88
Propagation loss at lasing wavelength (dB/cm)	0.073
Reflectance of OC at lasing wavelength (%)	98
Reflectance of blazed grating at 1st order (%)	88

doi:10.6342/NTU202203086

Chapter 5

Single-transverse Mode Ti:sapphire Crystal Fiber Laser

For laser applications, the size and location of the resonator mode are vital. Higher-order modes possess a higher threshold and are less efficient, but they can oscillate nonetheless if the resonator and pump optics are not designed properly. It is possible to generate high-order transverse modes by misaligning the end mirrors. In multimode operation, the characteristics of the output beam, such as divergence, focused spot size, and Rayleigh range, are poorly defined. For fundamental mode operation, there are numerous advantages that make it a desirable design goal. The divergence of a laser beam can be low, which keeps the laser with high power density over long propagation distances. The focused spot size can be smaller than that produced by higher-order modes. The high brightness and small spot size of this type of laser make it ideal for laser cutting [103], medical treatment [104], and other applications. In addition, because the output beam intensity is characterized by a uniform Gaussian profile, it is useful for many illumination and OCT applications [105].

5.1 Mode-field Analysis of Wavelength-swept Ti:sapphire Crystal Fiber Laser

The experimental setup is the same as Fig. 4.18. The transverse mode of WSL was imaged on a charge-coupled device (CCD) with an aspherical lens (L_4, 5726-B-H, f = 15.4 mm, NA = 0.16, Newport). Nevertheless, instantaneous CCD images are difficult to capture during wavelength sweeps. Therefore, the transverse modes at different wavelengths were analyzed by rotating the grating manually, as shown in Table 5.1.

doi:10.6342/NTU202203086

Table 5.1. The transverse modes of wavelength-tuning Ti:sapphire CF laser.

683.15 nm	703.5 nm	722 nm
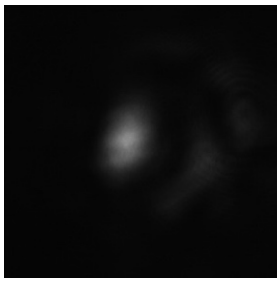	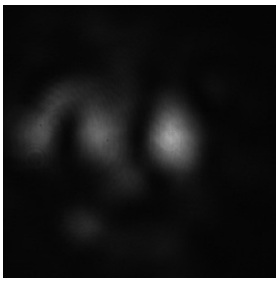	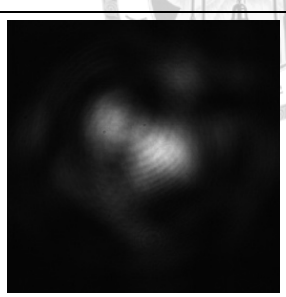
742.82 nm	**762.02 nm**	**782.78 nm**
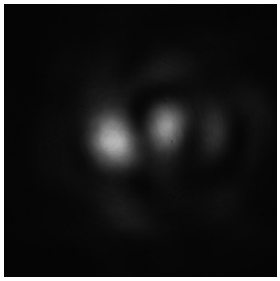	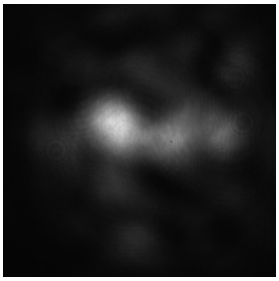	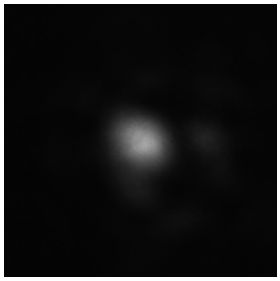
792.69 nm	**802.53 nm**	**822.13nm**
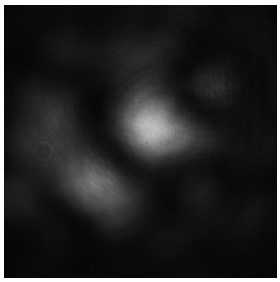	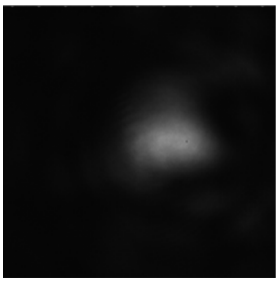	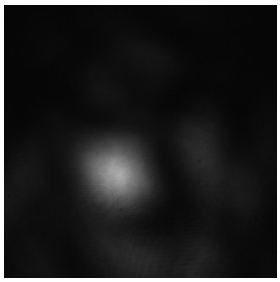
842.01 nm	**860.47 nm**	**882.58 nm**
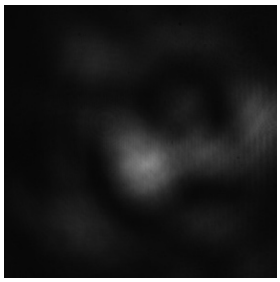	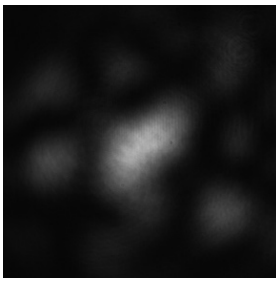	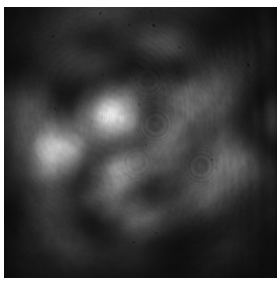
903.23 nm	**920.22 nm**	**937.07 nm**
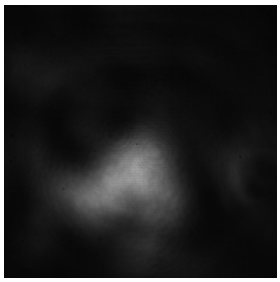	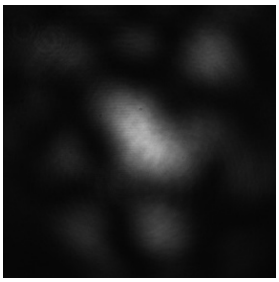	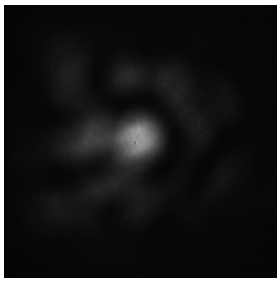

doi:10.6342/NTU202203086

The tuning range is from 683.15 nm to 937.07 nm. The transverse modes are highly wavelength-dependent, and exhibit typically few-mode patterns. When the tuning wavelength is close to the center wavelength (near 800-nm), the laser is more easily modulated into the fundamental mode due to the gain guiding effect.

In order to analyze the spatial distribution, the transverse modes for each wavelength, we calculate their center of intensity. , as shown in Fig. 5.1(a) and (b). The transmission distance form laser output coupler to CCD is 10 cm. Calculating the relationship between the spatial distribution of the center of intensity and transmission distance can further provide the pointing in the X- and Y-directions, as shown in Fig. 5.2. The standard deviation of the pointing in the X- and Y-directions is 877.7 μm and 987.7 μm, respectively. Through different analysis methods, it has been repeatedly shown that the number and spatial distribution of transverse modes formed by different wavelengths are random and difficult to control. As a result, this ultra-broadband WSL cannot be effectively used in various measurements, such as interferometry, because it shows that each wavelength cannot be fixed to measure the same position. For future applications, this result will make many unexpected erroneous measurements and analyses.

doi:10.6342/NTU202203086

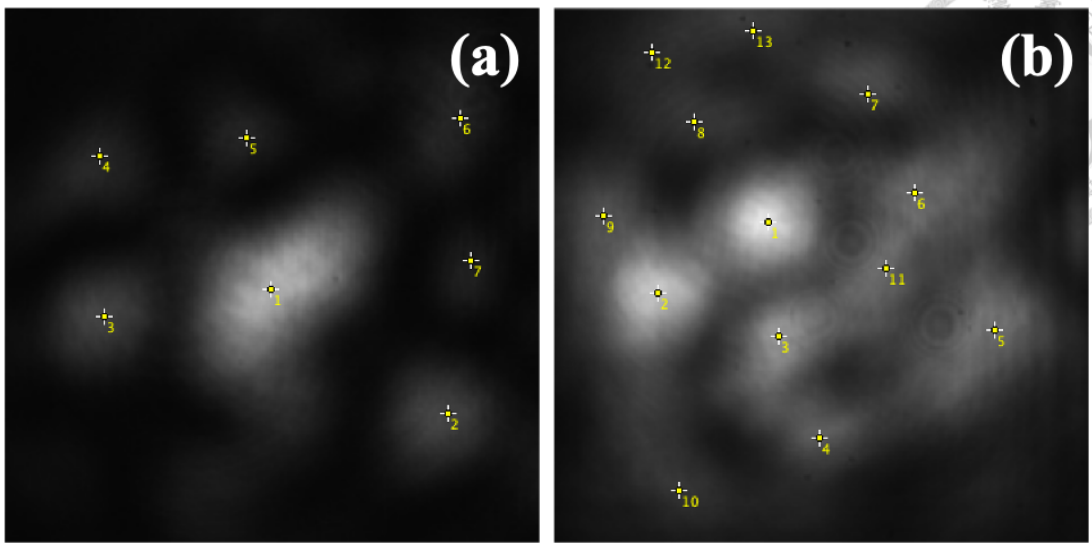

Fig. 5.1. The transverse mode pattern at (a) 860.47 nm, and (b) 882.58 nm. (Yellow dots indicate the coordinate and intensity of each transverse mode)

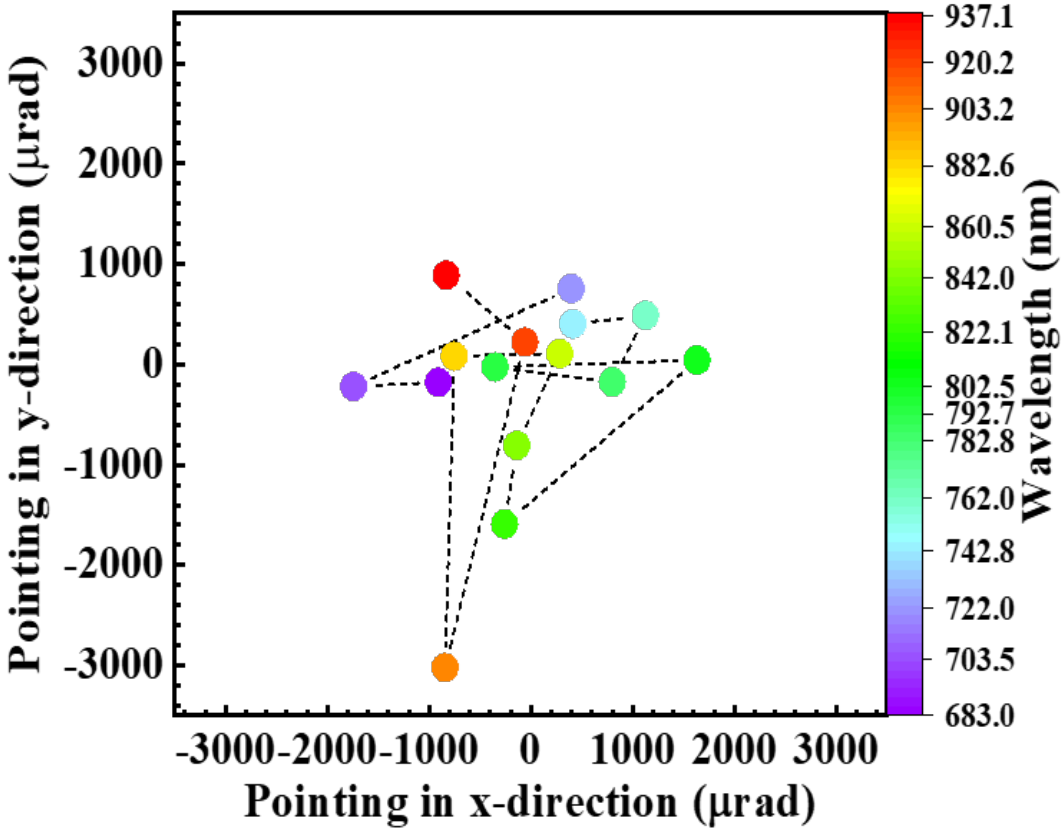

Fig. 5.2. Wavelength-dependent pointing stability.

doi:10.6342/NTU202203086

5.2 Analysis of Ti:sapphire Crystal Fiber Lasers with Single-mode Operation

5.2.1 Mode-field and Spectrum Analysis of Continuous-wave Ti:sapphire Crystal Fiber Laser

Since the spatial filtering technique can reduce transverse mode numbers, we decided to insert the single-mode fiber into the laser cavity. By using the spatial filtering method to generate the single-transverse-mode laser. The experimental setup is the same as Fig. 4.12. The CW laser was generated to analyze the output characteristics via CCD. A16× aspheric lens (L_3, 5726-B-H, f = 15.4 mm, NA = 0.16, Newport) was used to achieve mode matching with the OC_1. A 16× aspheric lens (L_4, 5726-B-H, f = 15.4 mm, NA = 0.16, Newport) is used to collect and collimate the laser output for measurement. The threshold of 255 mW is shown in Fig. 5.3. In Fig. 5.4, the spectrum became more complex as pump power increased from 476 mW to 1600 mW. There are three reasons by which the spectrum becomes complex: the ultra-broadband gain medium, the inhomogeneous broadening caused by the inhomogeneous gain medium, and the spatial hole burning effect caused by the spatial standing wave.

doi:10.6342/NTU202203086

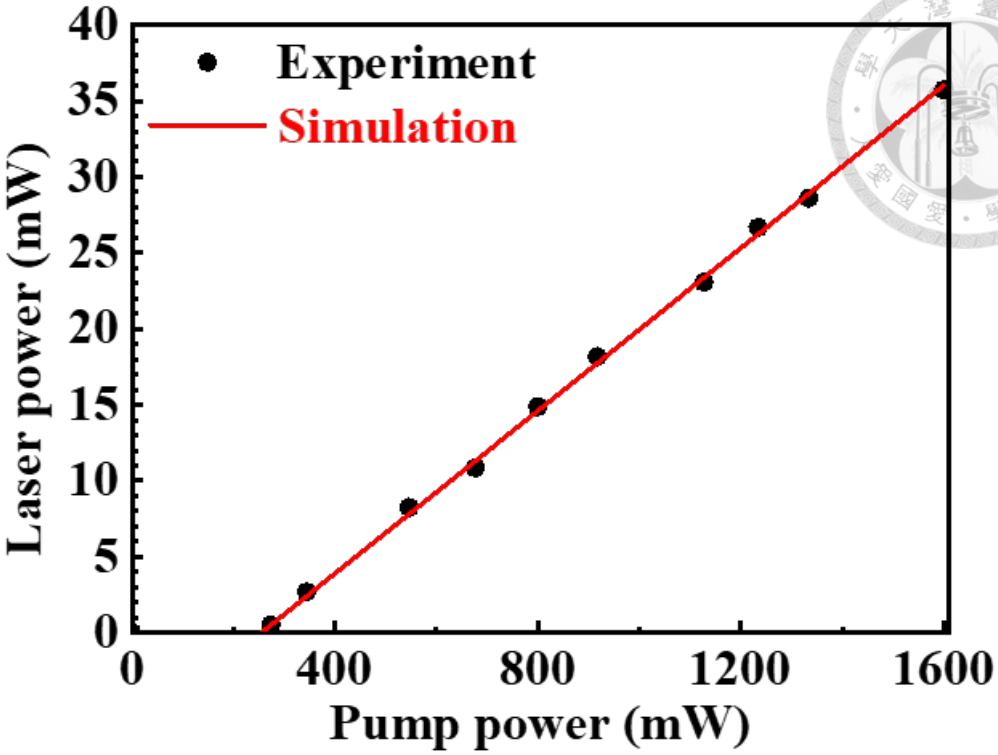

Fig. 5.3. L-I curve of Ti:sapphire CF laser.

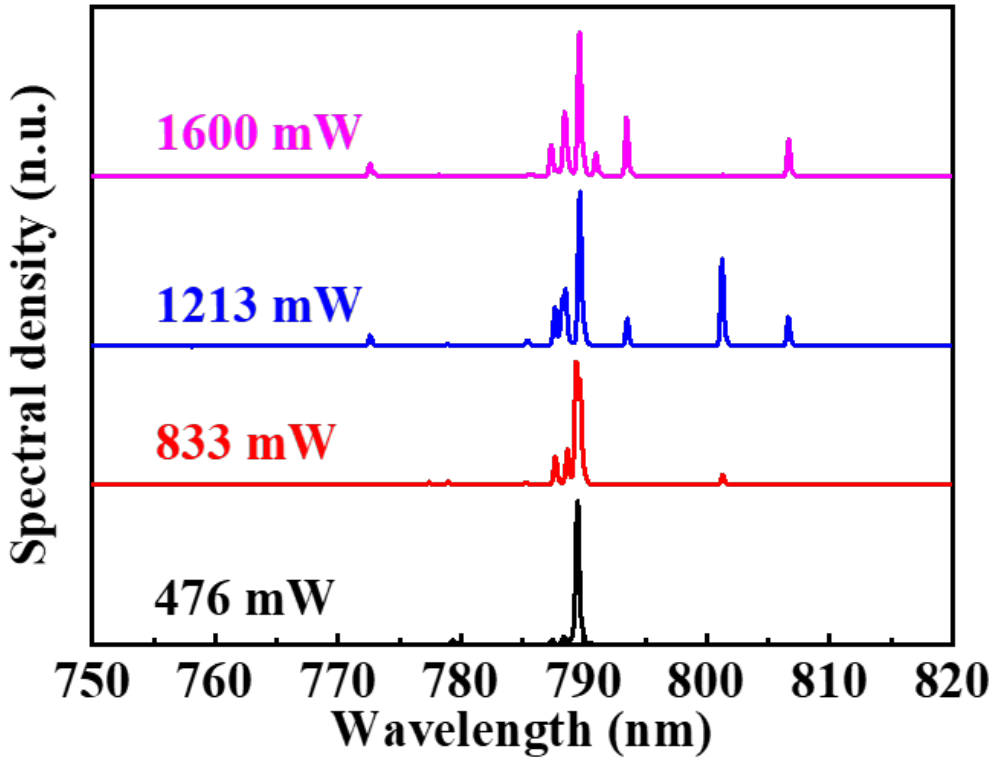

Fig. 5.4. Spectra of Ti:sapphire CF laser with different pump powers.

doi:10.6342/NTU202203086

The transverse modes of Ti:sapphire CF laser with different pump powers were imaged on a CCD, as shown in Fig. 5.5(a). With an increased pump power from 476 mW to 1600 mW, a complex CCD image was recorded due to the generation of multiple transverse mode. This is because the gain medium in this experiment is a multimode CF, so high-order transverse modes are likely to exist in the CF. When the pump power increases, the high-order transverse modes will have enough gain to overcome the laser threshold. By using ImageJ to establish the energy distribution of multiple transverse mode in three-dimensional (3D) graphics, it is easier to distinguish the distribution range of laser and ASE, as shown in Fig. 5.5(b).

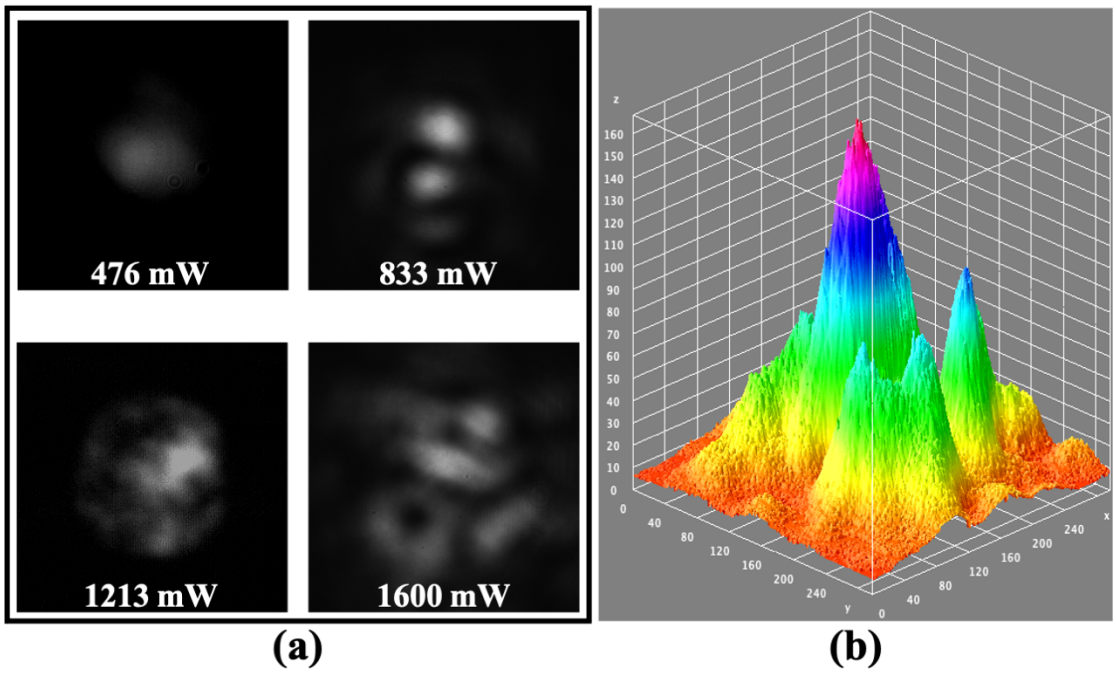

Fig. 5.5. (a) The transverse modes of two 520-nm LDs pumped glass-clad Ti:sapphire CF laser with different pump powers. (b) A 3D profile of the multi-transverse-mode intensity with 1600-mW pump power.

doi:10.6342/NTU202203086

5.2.2 Mode-field and Spectrum Analysis of Continuous-wave Ti:sapphire Crystal Fiber Laser with Single-mode Operation

For single-mode operation, the single-mode fiber (780HP, Thorlabs) was inserted into the CW laser system, as shown in Fig. 5.6. A16× aspheric lens (L_3, 5726-B-H, f = 15.4 mm, NA = 0.16, Newport) was used to couple the ASE into 780HP fiber. At the end of fiber, the butt-coupling method was used to achieve mode matching with the OC_1. A 16× aspheric lens (L_4, 5726-B-H, f = 15.4 mm, NA = 0.16, Newport) is used to collect and collimate the laser output for measurement. t. This configuration has a lasing threshold of 398 mW, as shown in Fig. 5.7. As a result of the spatial filtering, the spectrum maintains nearly single-transverse mode as pump power increased from 476 mW to 1600 mW, as shown in Fig. 5.8.

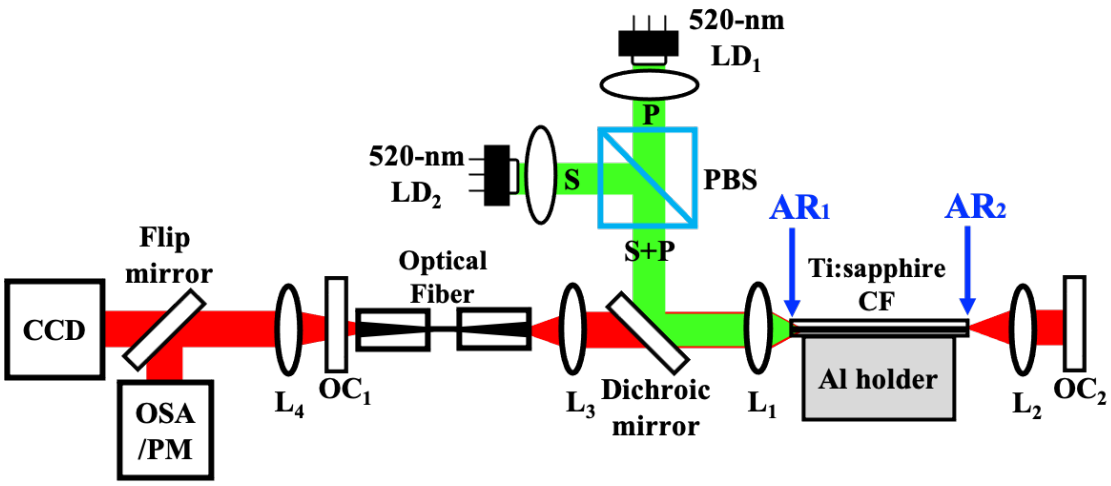

Fig. 5.6. Schematic of the LD-pumped glass-clad Ti:sapphire CF laser with an intracavity optical fiber (780HP).

doi:10.6342/NTU202203086

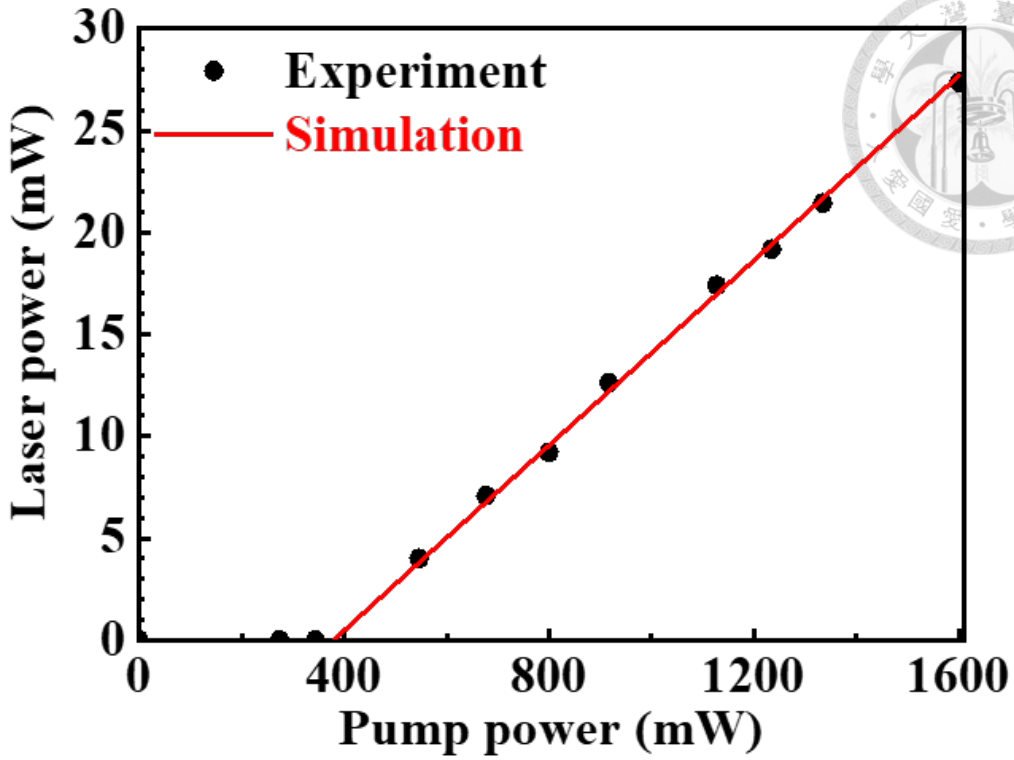

Fig. 5.7. L-I curve of the Ti:sapphire CF laser with intracavity optical fiber (780HP).

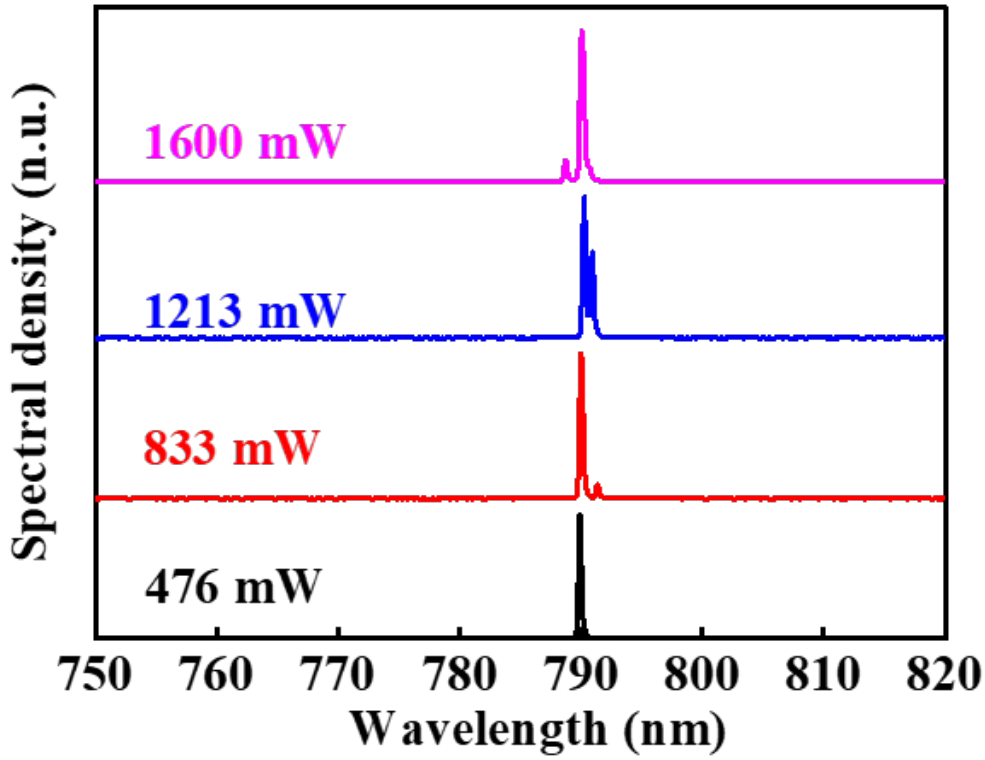

Fig. 5.8. The lasing spectrum of single-transverse-mode Ti:sapphire CF laser with intracavity optical fiber (780HP) for different pump powers.

doi:10.6342/NTU202203086

As a result, the multi-transverse mode will induce additional longitudinal modes, and, as a consequence, the lasing will be nearly single wavelength as the high-order modes were filtered, as show in Fig. 5.9. Some slight peaks can still lase near the main lasing wavelength, so we can speculate that produced by inhomogeneous broadening effect and ultra-broadband gain medium. From the results, it can be speculated that the multi-path characteristics of multi-transverse mode, that induce serious spatial hole burning effect.

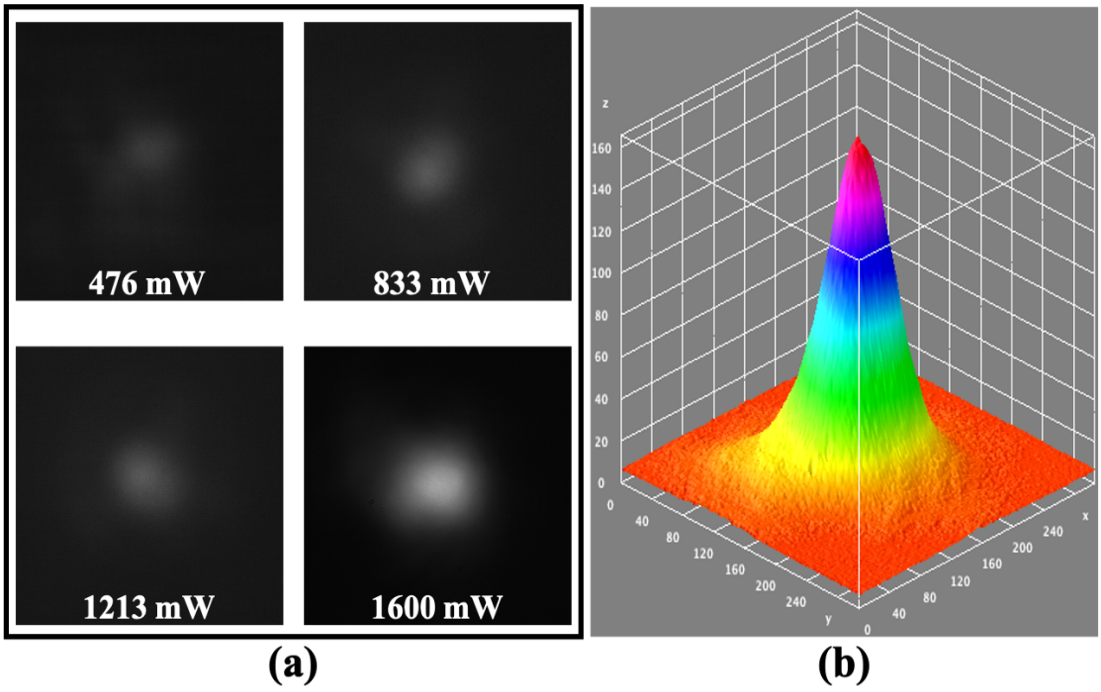

Fig. 5.9. (a) The single-transverse mode of Ti:sapphire CF laser with different pump powers. (b) A 3D profile of the single-transverse-mode intensity with 1600 mW pump power.

doi:10.6342/NTU202203086

5.3 Mode-field and Spectrum Analysis of Wavelength-swept Ti:sapphire Crystal Fiber Laser with Single-mode Operation

Two different types of optical fibers are inserted in the wavelength-swept Ti:sapphire crystal-fiber laser, as shown in Fig. 5.10. The emission spectra were monitored by an OSA (MS9740A, Anritsu) and the transverse mode of the laser was measured by a CCD. The total cavity length, including the optical fiber, is about 120 cm. A comparison of the L-I curves of the WSL, with and without fiber, is shown in Fig. 5.11. By inserting the SMF-28e optical fiber (Thorlabs), the threshold is increase from 346 mW to 464 mW. From the simulation results, we calculated that the loss of the WSL system has an insertion loss of 10% when using the SMF-28e optical fiber. However, comparing the insertion loss of the two fibers shows only a 5% difference. The threshold shifts from 346 mW to 512 mW when inserting the 780HP optical fiber.

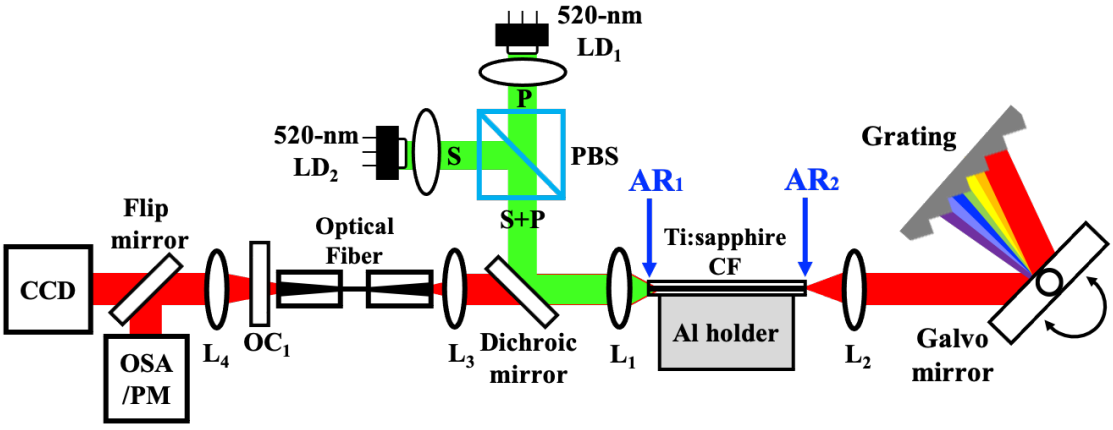

Fig. 5.10. Experimental setup of wavelength-swept Ti:sapphire CF laser with inserting different types of fibers.

doi:10.6342/NTU202203086

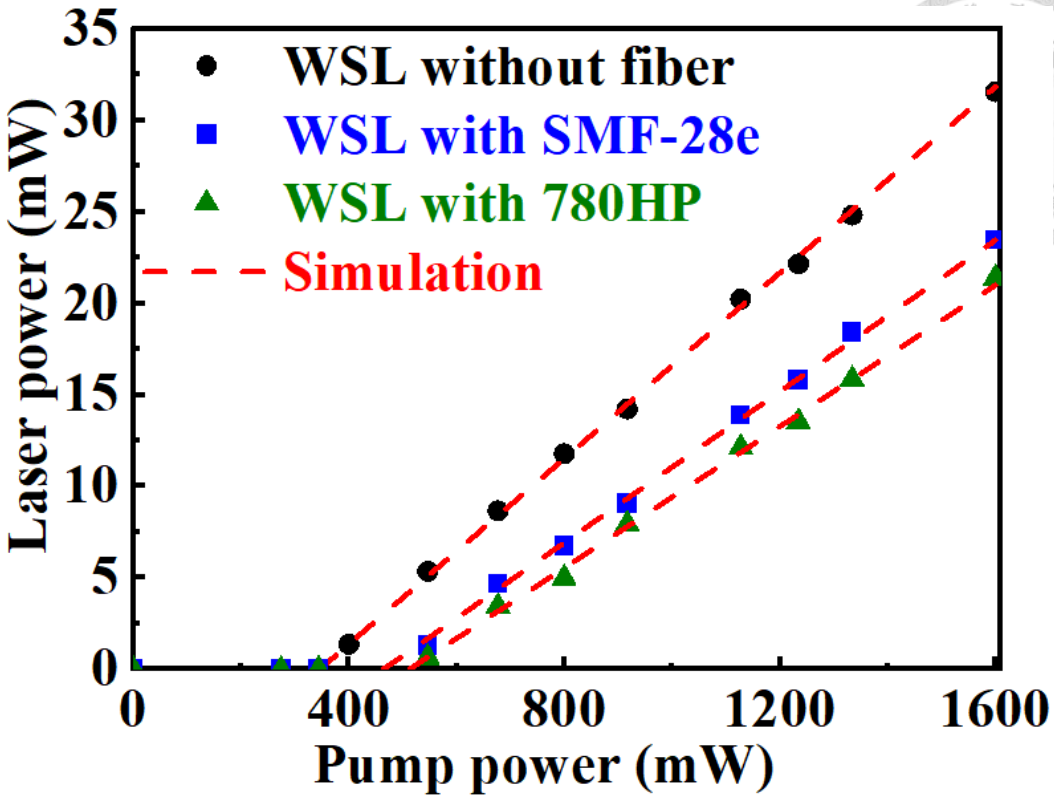

Fig. 5.11. The L-I curves of WSL with inserting different types of fibers.

Figure 5.12(a) shows the CCD image that represents the intensity profile of the WSL without inserting any fiber, which shows an obvious multi-transverse mode output. The 3D profile shows that in addition to the distribution of multi-transverse mode, and the laser still exhibits many stray lights, such as ASE. With the SMF-28e optical fiber filtering out most high-order transverse modes, the original multi-transverse mode of the WSL has been reduced significantly. From the CCD image and 3D intensity profile, it can be observed that the laser output has several transverse modes, as shown in Fig. 5.12(b). In Fig. 5.12(c), the single-transverse-mode WSL was obtained after spatial filtering with a 780HP optical fiber. By comparing Fig. 5.12(b) with Fig. 5.12(c), it can be observed that two transverse modes are only slightly different, which explains why the laser thresholds obtained when using both types of fibers are so close in Fig. 5.11. Table 5.2 presents the parameters of fitted experiment results and simulation.

doi:10.6342/NTU202203086

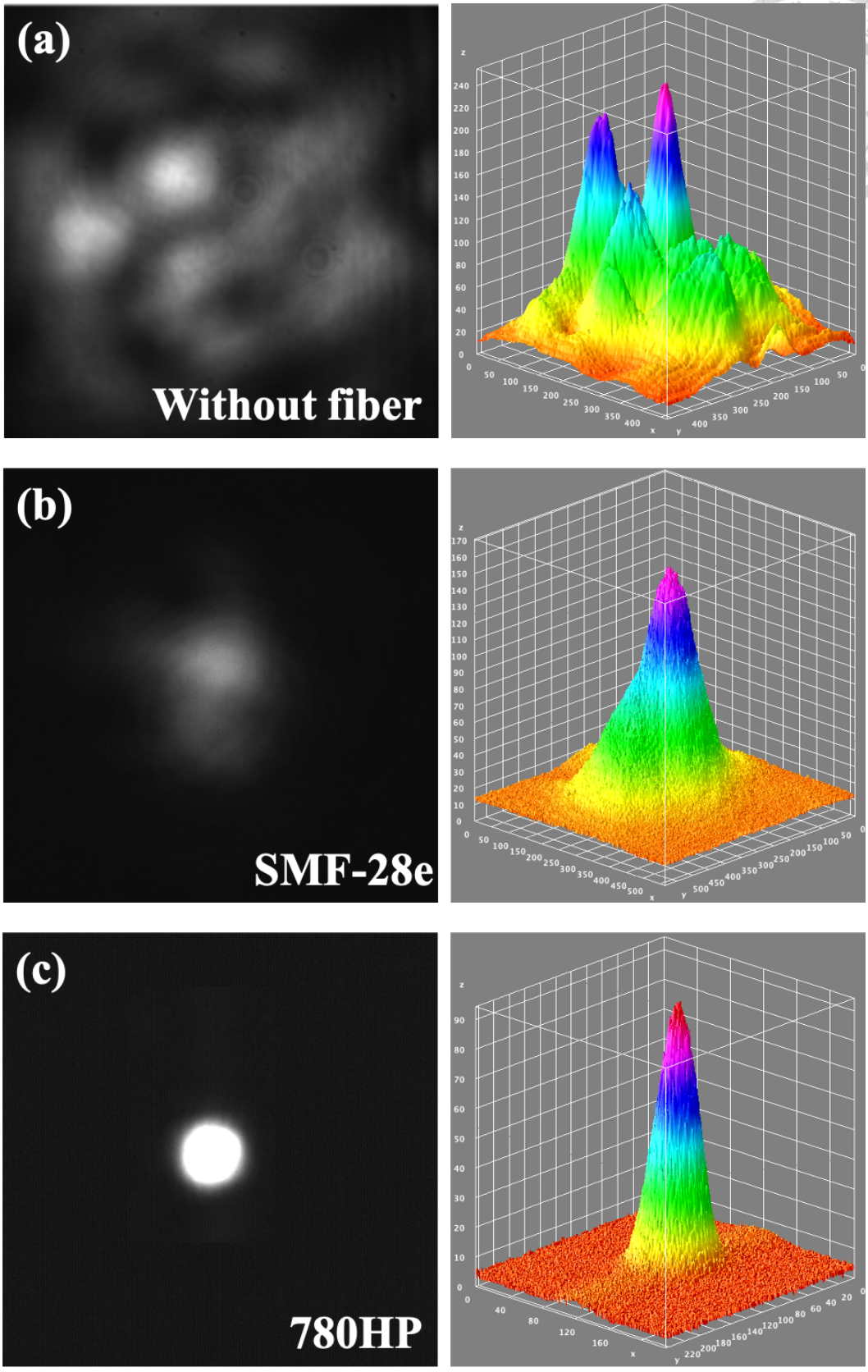

Fig. 5.12. Transverse modes of the WSL (a) without optical fiber, (b) with SMF-28e optical fiber, and (c) with 780HP optical fiber.

doi:10.6342/NTU202203086

Table 5.2. Simulation parameters of fitted wavelength-swept Ti:sapphire CF lasers with different types of optical fibers.

	This work
Tuning range (nm)	680~940
Absorption cross-section at 520 nm (cm^2)	5.7×10^{-20}
Emission cross section at 790 nm (cm^2)	2.4×10^{-19}
Lifetime decay (μs/W)	-0.33
Average fluorescence lifetime (μs)	2.67
Attenuation coefficient at 520 nm (dB/cm)	3.112
Coupling efficiency of CF at 520 nm (%)	88
Propagation loss at lasing wavelength (dB/cm)	0.073
Reflectance of OC at lasing wavelength (%)	98
Reflectance of blazed grating at 1st order (%)	88
Insertion loss of SMF-28e optical fiber (%)	10
Insertion loss of 780HP optical fiber (%)	15

doi:10.6342/NTU202203086

However, the spatial filtering technique makes the tuning range of WSL discontinue, since the multi-transverse-mode characteristics of Ti:sapphire CF are not optimized. Thus, the spectrum becomes more discrete as the spatial filtering effect is stronger, as shown in Fig. 5.13. Due to the increase of loss caused by single-mode fiber, the tuning bandwidth is reduced from 250 nm to 192 nm. Nevertheless, all the wavelengths generated are single transverse mode outputs, which improves the feasibility of applying this WSL in practical applications.

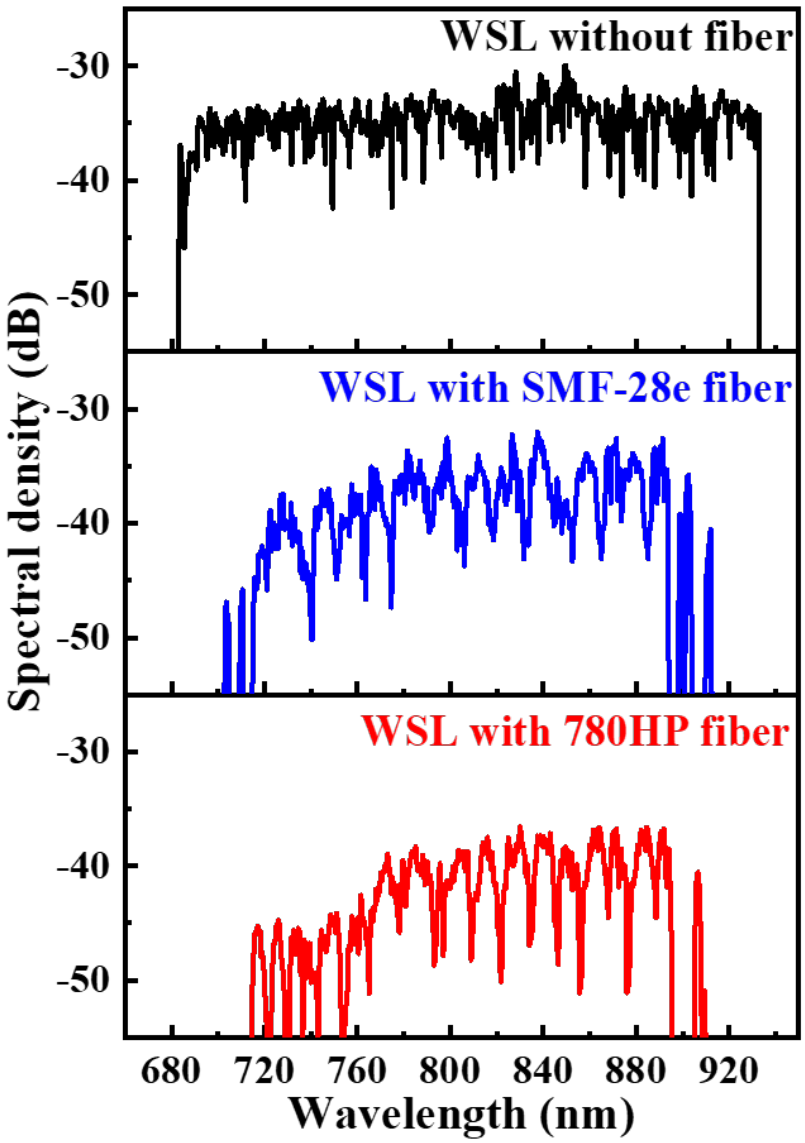

Fig. 5.13. The spectra of WSL with inserting different types of fibers. The resolution bandwidth of the OSA is 1 nm.

`

doi:10.6342/NTU202203086

Chapter 6

Conclusions and Future Work

6.1 Conclusions

In our laboratory, Ti:sapphire single CF grown by the laser-heated pedestal growth method significantly improves thermal dissipation and pump interaction length. The diameter of the Ti:sapphire single CF is 16 μm. The cladding process was produced by the glass cladding process. At 780 nm, the signal loss of glass-clad Ti:sapphire CF was 0.017 cm^{-1}, which includes the propagation loss and re-absorption of the Ti^{3+}–Ti^{4+} pair. The maximum temperature of crystal core is only up to 329 K with 1.6-W full pump power, and lifetime is 2.67 μs. It proves that the glass-clad CF has high heat dissipation capability. Using this glass-clad Ti:sapphire CF as the gain medium, there are three types of Ti:sapphire CF lasers were built up.

A. Continuous-wave Ti:sapphire crystal fiber laser with AR-AR coatings

In order to comprehensively use our crystal fiber, we designed anti-reflection coatings on both endfaces of CF, and set up a laser system with two output couplers with the threshold of 274 mW. Such a system opens up more possibilities for future research, such as spatial filtering using single-mode fibers and fiber-ring lasers.

B. Wavelength-tuning Ti:sapphire crystal fiber laser with grating

The wavelength tuning was accomplished by rotating the grating in the table plane. The slope efficiency is 0.61% and the threshold pump power is 320 mW. The wavelength-tuning Ti:sapphire CF laser has a tunable bandwidth of 260 nm (from 680 nm to 940 nm).

C. Ultra-broadband wavelength-swept Ti:sapphire crystal fiber laser with galvo mirror

A 250-nm-tuning-range WSL with a 1200-Hz repetition rate is successfully demonstrated. Both the steady-state performance and the pulsed dynamics well agree with our simulations.

`

doi:10.6342/NTU202203086

At a sweeping wavelength speed of 300 nm/ms with a repetition rate of 1200 Hz, the 0.018-nm instantaneous linewidth of the Ti:sapphire swept laser can achieve a 3-dB sensitivity roll-off of 7 mm. The estimated axial resolution is 1.8 μm in air, which reveals our WSL could provide cellular resolution. The PSF side lobes are less than 10% (0.46 dB), which indicates low axial image pixel crosstalk. Finally, a single-transverse mode WSL is successfully demonstrated by using the spatial filtering method. As a result, it improves the feasibility of applying this WSL in practical applications.

6.2 Future Work

For optimum use of this light source , a single-mode fiber structure of Ti:sapphire CF is necessary for improving single-transverse mode Ti:sapphire WSL. For matching broadband refractive indices, Al_2O_3 ceramic is a suitable cladding material for sapphire cores [51]. Combining the spatial filtering method used in this dissertation with the single-transverse mode Ti:sapphire CF, the single-transverse mode swept-frequency laser can be truly realized. Our group has demonstrated high-speed Mirau-based FF-OCT, which can provide high quality lateral and axial images. However, the scanning speed of most FF-OCT are too slow, because scanning depth is depended on PZT movement. So, the image quality may be worse by vibration from environment. In the future, the single-transverse mode WSL could be integrated with the Mirau-based FF-OCT for high en face imaging rates.

doi:10.6342/NTU202203086

References

[1] S. T. Sanders, J. A. Baldwin, T. P. Jenkins, D. S. Baer, and R. K. Hanson, "Diode-laser sensor for monitoring multiple combustion parameters in pulse detonation engines," Proc. Combust. Inst. **28**, 587 (2000).

[2] S. R. Chinn, E. A. Swanson, and J. G. Fujimoto, "Optical coherence tomography using a frequency-tunable optical source," Opt. Lett. **22**, 340 (1997).

[3] W. Drexler, M. Liu, A. Kumar, T. Kamali, A. Unterhuber, and R. A. Leitgeb, "Optical coherence tomography today: speed, contrast, and multimodality," J. Biomed. Opt. **19**, 071412 (2014).

[4] T. Klein and R. Huber, "High-speed OCT light sources and systems," Biomed. Opt. Express **8**, 828 (2017).

[5] R. Huber, M. Wojtkowski, K. Taira, J. G. Fujimoto, and K. Hsu, "Amplified, frequency swept lasers for frequency domain reflectometry and OCT imaging-design and scaling principles," Opt. Express **13**, 3513 (2005).

[6] H. Lee, G. H. Kim, M. Villiger, H. Jang, B. E. Bouma, and C. S. Kim, "Linear-in-wavenumber actively-mode-locked wavelength-swept laser," Opt. Lett. **45**, 5327 (2020).

[7] B. Potsaid, B. Baumann, D. Huang, S. Barry, A. E. Cable, J. S. Schuman, J. S. Duker, and J. G. Fujimoto, "Ultrahigh speed 1050nm swept source / Fourier domain OCT retinal and anterior segment imaging at 100,000 to 400,000 axial scans per second," Opt. Express **18**, 20029 (2010).

[8] W. Wieser, B. R. Biedermann, T. Klein, C. M. Eigenwillig, and R. Huber, "Multi-Megahertz OCT: High quality 3D imaging at 20 million A-scans and 4.5 GVoxels per second," Opt. Express **18**, 14685 (2010).

`

doi:10.6342/NTU202203086

[9] T. S. Kim, J. Joo, I. Shin, P. Shin, W. J. Kang, B. J. Vakoc, and W. Y. Oh, "9.4 MHz A-line rate optical coherence tomography at 1300 nm using a wavelength-swept laser based on stretched-pulse active mode-locking," Sci. Rep. **10**, 9328 (2020).

[10] Y. Okabe, Y. Sasaki, M. Ueno, T. Sakamoto, S. Toyoda, S. Yagi, K. Naganuma, K. Fujiura, Y. Sakai, J. Kobayashi, K. Omiya, M. Ohmi, and M. Haruna, "200 kHz swept light source equipped with KTN deflector for optical coherence tomography," Electron. Lett. **48**, 201 (2012).

[11] G.H. Lee, S. Ahn, J. Gene, and M.Y. Jeon, "1.1-μm band extended wide-bandwidth wavelength-swept laser based on polygonal scanning wavelength filter," Sensors **21**, 3053 (2021).

[12] K. F. Wall, and A. Sanchez, "Titanium sapphire lasers," Linc. Lab. j. **3**, 447 (1990).

[13] S. Karp and B. Jalali, "Frequency-doubled FDML-MOPA laser in the visible," Opt. Lett. **44**, 5913 (2019).

[14] https://www.thorlabs.com/catalogpages/547.pdf.

[15] J. Cao, P. Wang, Y. Zhang, G. Shi, B. Wu, S. Zhang, and Y. Liu, "Methods to improve the performance of the swept source at 1.0 μm based on a polygon scanner," Photonics Res. **5**, 245 (2017).

[16] P. Qiao, K. T. Cook, J. Qi, L. A. Coldren, and C. J. Chang-Hasnain, "Wide, continuously swept VCSEL using a novel air-cavity-dominant design," OFC Conference, 1 (2018).

[17] K. Li, C. Chase, P. Qiao, and C. J. Chang-Hasnain, "Widely tunable 1060-nm VCSEL with highcontrast grating mirror," Opt. Express **25**, 11844 (2017).

[18] H. Sunaga, K. Endo, T. Ogawa, M. Shinagawa, S. Toyoda, M. Ueno, Y. Sasaki,

doi:10.6342/NTU202203086

M. Chen, and T. Sakamoto, “Voltage noise and jitter analysis for swept source optical coherence tomography using $KTa_{1-x}Nb_xO_3$ deflector,” Measurement **135**, 753 (2019).

[19] https://www.santec.com/en/products/oct/lasers-for-swept-source-oct.html#hsl-21.

[20] R. Huber, M. Wojtkowski, and J. G. Fujimoto, “Fourier domain mode locking: A new laser operating regime and applications for optical coherence tomography,” Opt. Express **14**, 3225 (2006).

[21] https://www.optores.com/index.php/products/31-next-generation-fdml-laser.

[22] C. Jun, M. Villiger, W.-Y. Oh, and B. E. Bouma, “All-fiber wavelength swept ring laser based on Fabry-Perot filter for optical frequency domain imaging,” Opt. Express **22**, 25805 (2014).

[23] https://www.excelitas.com/product/high-speed-ss-oct-tunable-laser-engines.

[24] D. C. Adler, Y. Chen, R. Huber, J. Schmitt, J. Connolly, and J. G. Fujimoto, “Three-dimensional endomicroscopy using optical coherence tomography,” Nat. Photonics **1**,709 (2007).

[25] J. Xu, X. Wei, L. Yu, C. Zhang, J. Xu, K. K. Y. Wong, and K. K. Tsia, “High-performance multi-megahertz optical coherence tomography based on amplified optical time-stretch,” Biomed. Opt. Express **6**, 1340 (2015).

[26] J. Kang, P. Feng, X. Wei, E. Y. Lam, K. K. Tsia, and K. K. Y. Wong, “Ultrafast and broadband inertia-free swept source for optical coherence tomography,” Asia Communications and Photonics Conference (2017).

[27] H. Chen, Y. Li, D. Huang, F. Li, C. Lu, and P. K. A. Wai, “114 nm broadband all-fiber nonlinear polarization rotation mode locked-laser and time-stretch optical coherence tomography,” Opt. Express **29**, 33322 (2021).

doi:10.6342/NTU202203086

[28] B. R. Biedermann, W. Wieser, C. M. Eigenwillig, and R. Huber, "Recent developments in Fourier Domain Mode Locked lasers for optical coherence tomography: Imaging at 1310 nm vs. 1550 nm wavelength," J. Biphotonics **2**, 357 (2009).

[29] S. Tan, L. Yang, X. Wei, C. Li, N. Chen, K. K. Tsia, and K. K. Y. Wong, "High-speed wavelength-swept source at 2.0 μm and its application in imaging through a scattering medium," Opt. Lett. **42**, 1540 (2017).

[30] R. I. Woodward, M. R. Majewski, D. D. Hudson, and S. D. Jackson, "Swept-wavelength mid-infrared fiber laser for real-time ammonia gas sensing," APL Photonics 4, 020801 (2019).

[31] S. L. Jacques, "Optical properties of biological tissues: a review," Phys. Med. Biol 58, R37 (2013).

[32] W. Drexler, U. Morgner, F. X. Kärtner, C. Pitris, S. A. Boppart, X. D. Li, E. P. Ippen, and J. G. Fujimoto, "In vivo ultrahigh-resolution optical coherence tomography," Opt. Lett. 24, 1221 (1999).

[33] M. Wojtkowski, V. J. Srinivasan, T. H. Ko, J. G. Fujimoto, A. Kowalevicz, and J. S. Duker, "Ultrahigh-resolution, high-speed, Fourier domain optical coherence tomography and methods for dispersion compensation," Opt. Express **12**, 2404 (2004).

[34] S. Wada, K. Akagawa, and H. Tashiro, "Electronically tuned Ti:sapphire laser," Opt. Lett. **21**, 731 (1996).

[35] V. M. Kodach, D. J. Faber, and T. G. Van Leeuwen, "Wavelength swept Ti:sapphire laser," Opt. Commun. **281**, 4975 (2008).

`

doi:10.6342/NTU202203086

[36] M. M. Fejer, J. L. Nightingale, G. A. Magel, and R. L. Byer, "Laser-heated miniature pedestal growth apparatus for single-crystal optical fibers," Rev. Sci. Instrum. **55**, 1791 (1984).

[37] K. Y. Hsu, D. Y. Jheng, Y. H. Liao, T. S. Ho, C. C. Lai, and S. L. Huang, "Diode-laser-pumped glass-clad Ti:sapphire crystal-fiber-based broadband light source," IEEE Photon. Technol. Lett. **24**, 854 (2012).

[38] S. C. Wang, C. Y. Hsu, T. T. Yang, D. Y. Jheng, T. I. Yang, T. S. Ho, and S. L. Huang, "Laser-diode pumped glass-clad Ti:sapphire crystal fiber laser," Opt. Lett. **41**, 3217 (2016).

[39] T. T. Yang, T. I. Yang, R. Soundararajan, P. S. Yeh, C. Y. Kuo, S. L. Huang, and S. Donati, "Widely tunable, 25-mW power, Ti:sapphire crystal-fiber laser," IEEE Photon. Technol. Lett. **31**, 1921 (2019).

[40] Y. C. Lin, T. T. Yang, and S. L. Huang, "Ultra-broadband wavelength-swept Ti:sapphire crystal fiber laser," Opt. Lett. **47**, 2778 (2022).

[41] W. J. Choi, D. I. Jeon, S. Ahn, J. Yoon, S. Kim, and B. H. Lee, "Full-field optical coherence microscopy for identifying live cancer cells by quantitative measurement of refractive index distribution," Opt. Express **18**, 23285 (2010).

[42] T. Gambichler, S. Boms, M. Stücker, A. Kreuter, G. Moussa, M. Sand, P. Altmeyer, and K. Hoffmann, "Epidermal thickness assessed by optical coherence tomography and routine histology: preliminary results of method comparison," J. Eur. Acad. Dermatol. Venereol. **20**, 791 (2006).

[43] W. J. Choi, K. S. Park, T. J. Eom, M. K. Oh, and B. H. Lee, "Tomographic imaging of a suspending single live cell using optical tweezer-combined full-field optical coherence tomography," Opt. Lett. **37**, 2784 (2012).

`

doi:10.6342/NTU202203086

[44] T. S. Ho, M. R. Tsai, C. W. Lu, H. S. Chang, and S. L. Huang, "Mirau-type full-field optical coherence tomography with switchable partially spatially coherent illumination modes," Biomed. Opt. Express **12**, 2670 (2021).

[45] Y. T. Chen, C. Y. Tsai, Y. K. Chiu, T. W. Hsu, L. W. Chen, W. L. Chen, and S. L. Huang, "En face and cross-sectional corneal tomograms Using sub-micron spatial resolution optical coherence tomography," Sci. Rep. **8**, 14349 (2018).

[46] B. Povazay, A. Unterhuber, B. Hermann, H. Sattmann, H. Arthaber, and W. Drexler, "Full-field time-encoded frequency-domain optical coherence tomography," Opt. Express **14**, 7661 (2006).

[47] T. Bonin, G. Franke, M. Hagen-Eggert, P. Koch, and G. Hüttmann, "In vivo Fourier-domain full-field OCT of the human retina with 1.5 million A-lines/s," Opt. Lett. **35**, 3432 (2010).

[48] E. Auksorius, "Light-efficient beamsplitter for Fourier-domain full-field optical coherence tomography," Opt. Lett. **45**, 1240 (2020).

[50] E. R. Dobrovinskaya, L. A. Lytvynov, and V. Pishchik, Sapphire: Material, Manufacturing, Applications (Springer, New York, 2009).

[51] T. I. Yang, H. T. Liu, S. C. Wang, K. H. Chuang, T. C. Chou, and S. L. Huang, "Formation of ceramic and crystal claddings for a Ti:sapphire crystalline fiber core," Opt. Mater. Express **10**, 1215 (2020).

[52] http://refractiveindex.info/?shelf=main&book=Al2O3&page=Malitson-o.

[53] H. H. Telle and Á. G. Ureña, "Laser Spectroscopy and Laser Imaging: An Introduction," CRC Press (2018).

[54] E. D. Nelson, J. Y. Wong, and A. L. Schawlow, "Far infrared spectra of Al_2O_3:Cr^{3+} and Al_2O_3:Ti^{3+}," Phys. Rev. **156**, 298 (1967).

[55] P. F. Moulton, "Spectroscopic and laser characteristics of Ti:Al_2O_3," J. Opt. Soc.

doi:10.6342/NTU202203086

Amer. **3**, 125 (1986).

[56] R. L. Aggarwal, A. Sanchez, M. M. Stuppi, R. E. Fahey, A. J. Strauss, W. R. Rapoport, and C. P. Khattak, "Residual infrared absorption in as-grown and annealed crystals of Ti:Al_2O_3," IEEE J. Quantum Elect. **24**, 1003 (1988).

[57] M. Yamaga, T. Yosida, S. Hara, N. Nodama, and B. Henderson, "Optical and electron spin resonance spectroscopy of Ti^{3+} and Ti^{4+} in Al_2O_3," J. Appl. Phys. **75**, 1111 (1994).

[58] A. Sanchez, A. J. Strauss, R. L. Aggarwal, and R. E. Fahey, "Crystal growth, spectroscopy, and laser characteristics of Ti:Al_2O_3," IEEE J. Quantum Elect. **24**, 995 (1988).

[59] J. F. Pinto, L. Esterowitz, G. H. Rosenblatt, M. Kokta, and D. Peressini, "Improved Ti:sapphire laser performance with new high figure of merit crystals," IEEE J. Quantum Elect. **30**, 2612 (1994).

[60] R. Uecker, D. Klimm, S. Ganschow, P. Reiche, R. Bertram, M. Roßberg, and R. Fornari, "Czochralski growth of Ti:sapphire laser crystals," Proc. SPIE **5990**, 599006-1 (2005).

[61] T. Danger, K. Petermann, and G. Huber, "Polarized and time-resolved measurements of excited-state absorption and stimulated emission in Ti:$YAlO_3$ and Ti:Al_2O_3," Appl. Phys. **57**, 309 (1993).

[62] P. Albers, E. Stark, and G. Huber, "Continuous-wave laser operation and quantum efficiency of titanium-doped sapphire," J. Opt. Soc. Am. **3**, 134 (1986).

[63] B. E. A. Saleh and M. C. Teich, "Fundamentals of Photonics," 1st ed, Hoboken, NJ: John Wiley & Sons, Inc., 438 (1991).

[64] A. Cucinotta, S. Selleri, L. Vincetti, and M. Zoboli, "Numerical and experimental analysis of erbium-doped fiber linear cavity lasers," Opt. Commun.

doi:10.6342/NTU202203086

156, 264 (1998).

[65] H. H. Kusuma, Z. Ibrahim, and M. K. Saidin, "Optical energy gap of Ti:Al2O3 single crystals," J. Appl. Sci. **11**, 888 (2011).

[66] S. E. Demina, E. N. Bystrova, V. S. Postolov, E. V. Eskov, M. V. Nikolenko, D. A. Marshanin, V. S. Yuferev, and V. V. Kalaev, "Use of numerical simulation for growing high-quality sapphire crystals by the Kyropoulos method," J. Cryst. Growth **310**, 1443 (2008).

[67] A. Nehari, A. Brenier, G. Panzer, K. Lebbou, J. Godfroy, S. Labor, H. Legal, G. Chériaux, J. P. Chambaret, T. Duffar, and R. Moncorgé, "Ti-doped sapphire (Al_2O_3) single crystals grown by the Kyropoulos technique and optical characterizations," Cryst. Growth Des. **11**, 445 (2011).

[68] D. Viechnicki and F. Schmid, "Growth of large monocrystals of Al_2O_3 by a gradient furnace technique," J. Crystal Growth **11**, 345 (1971).

[69] C. P. Khattak and F. Schmid, "Growth of the world's largest sapphire crystals," J. Cryst. Growth **225**, 572 (2001).

[70] E. A. Ghezal, A. Nehari, K . Lebbou, and T. Duffar, "Observation of gas bubble incorporation during micropulling-down growth of sapphire," Cryst. Growth Des. **12**, 5715 (2012).

[71] A. Nehari, T. Duffar, E.A. Ghezal, and K. Lebbou, "Chemical segregation of titanium in sapphire single crystals grown by micro-pulling-down technique: analytical model and experiments," Cryst. Growth Des. **14**, 6492 (2014).

[72] D. H. Zhou, C. T. Xia, Y. Guyot, J. P. Zhong, X. D. Xu, S. L. Feng, W. Q. Lu, J. H. Song, and K. Lebbou, "Growth and spectroscopic properties of Ti-doped sapphire single-crystal fibers," Opt. Mater. **47**, 495 (2015).

[73] C. A. Burrus and J. Stone, "Single-crystal fiber optical devices," Appl. Phys.

doi:10.6342/NTU202203086

Lett. **26**, 318 (1975).

[74] M. M. Fejer, J. L. Nightingale, G. A. Magel, and R. L. Byer, "Laser-heated miniature pedestal growth apparatus for single-crystal optical fibers," Rev. Sci. Instrum. **55**, 1791 (1984).

[75] T. I. Yang, "The Study of Near-Infrared Broadband Single Mode Crystal Fiber Light Sources," Ph.D. Dissertation, National Taiwan University, Taiwan (2021).

[76] R. S. Feigelson, "Pulling optical fibers," J. Cryst. Growth **79**, 669 (1986).

[77] K. Y. Hsu, D. Y. Jheng, Y. H. Liao, T. S. Ho, C. C. Lai, and S. L. Huang, "Diode-laser-pumped glass-clad Ti:sapphire crystal fiber based broadband light source," IEEE Photon. Technol. Lett. **24**, 854 (2012).

[78] L. Wu, A. Wang, J. Wu, L. Wei, G. Zhu, and S. Ying, "Growth and laser properties of Ti:sapphire single crystal fibres," Electron. Lett. **31**, 1151 (1995).

[79] M. R. Kokta, "Process for enhancing Ti:Al_2O_3 tunable laser crystal fluorescence by annealing," US Patent No. 4,587,035 (1986).

[80] M. R. Kokta, "Process for enhancing fluorescence of Ti:Al_2O_3 tunable laser crystals," US Patent No. 4,836,953 (1989).

[81] S. C. Wang, "Development and Applications of Glass-clad Ti:Al_2O_3 Crystal Fiber," Ph.D. Dissertation, National Taiwan University, Taiwan (2016).

[82] K. Y. Hsu, M. H. Yang, D. Y. Jheng, C. C. Lai, S. L. Huang, K. Mennemann, and V. Dietrich, "Cladding YAG crystal fibers with high-index glasses for reducing the number of guided modes," Opt. Mater. Express **3**, 813 (2013).

[83] C. Y. Lo, K. Y. Huang, J. C. Chen, S. Y. Tu, and S. L. Huang, "Glass-clad Cr^{4+}:YAG crystal fiber for the generation of superwideband amplified spontaneous emission," Opt. Lett. **29**, 439 (2004).

[84] S. C. Wang, T. I. Yang, D. Y. Jheng, C. Y. Hsu, T. T. Yang, T. S. Ho, and S. L.

doi:10.6342/NTU202203086

Huang, “Broadband and high-brightness light source: glass-clad Ti:sapphire crystal fiber,” Opt. Lett. **40**, 5594 (2015).

[85] A. A. Anderson, R. W. Eason, L. M. B. Hickey, M. Jelinek, C. Grivas, D. S. Gill, and N. A. Vainos, “Ti:sapphire planar waveguide laser grown by pulsed laser deposition,” Opt. Lett. **22**, 1556 (1997).

[86] M. Pollnau, R. P. Salath, T. Bhutta, D. P. Shepherd, and R. W. Eason, “Continuous-wave broadband emitter based on a transition-metal-ion-doped waveguide,” Opt. Lett. **26**, 283 (2001).

[87] A. Crunteanu, M. Pollnau, G. Jänchen, C. Hibert, P. Hoffmann, R. P. Salathé, R. W. Eason, C. Grivas, and D. P. Shepherd, “Ti:sapphire rib channel waveguide fabricated by reactive ion etching of a planar waveguide, ” Appl. Phys. B **75**, 15 (2002).

[88] L. M. B. Hickey, V. Apostolopoulos, R. W. Eason, and J. S. Wilkinson, “Diffused Ti:sapphire channel-waveguide lasers,” J. Opt. Soc. Am. B **21**, 1452 (2004).

[89] C. Grivas, D. P. Shepherd, T. C. May-Smith, and R. W. Eason, “Single-transverse-mode Ti:sapphire rib waveguide laser,” Opt. Express **13**, 210 (2005).

[90] C. Grivas, D. P. Shepherd, R. W. Eason, L. Laversenne, P. Moretti, C. N. Borca, and M. Pollnau, “Room-temperature continuous-wave operation of Ti:sapphire buried channel-waveguide lasers fabricated via proton implantation,” Opt. Lett. **31**, 3450 (2006).

[91] C. Grivas, C. Corbari, G. Brambilla, and P. G. Lagoudakis, “Tunable, continuous-wave Ti:sapphire channel waveguide lasers written by femtosecond and picosecond laser pulses,” Opt. Lett. **37**, 4630 (2012).

[92] C. Grivas, T. C. May-Smith, D. P. Shepherd, R. W. Eason, M. Pollnau, and M. Jelinek, “Broadband single-transverse-mode fluorescence sources based on ribs

doi:10.6342/NTU202203086

fabricated in pulsed laser deposited Ti:sapphire waveguides," Appl. Phys. A **79**, 1195 (2004).

[93] L. Laversenne, P. Hoffmann, M. Pollnau, P. Moretti, and J. Mugnier, "Designable buried waveguides in sapphire by proton implantation," Appl. Phys Lett. **85**, 5167 (2004).

[94] V. Apostolopoulos, L. Laversenne, T. Colomb, C. Depeursinge, R. P. Salathé, and M. Pollnau, "Femtosecond-irradiation-induced refractive-index changes and channel waveguiding in bulk Ti^{3+}:sapphire," Appl. Phys Lett. **85**, 1122 (2004).

[95] D. Y. Jheng, K. Y. Hsu, Y. C. Liang, and S. L. Huang, "Broadly tunable and low-threshold Cr^{4+}:YAG crystal fiber laser," IEEE J. Sel. Top. Quantum Electron. **21**, 0900608 (2015).

[96] P. Albers, E. Stark, and G. Huber, "Continuous-wave laser operation and quantum efficiency of titanium-doped sapphire," J. Opt. Soc. Am. B **3**, 134 (1986).

[97] A. Sennaroglu, "Broadly tunable Cr^{4+}-doped solid-state lasers in the near infrared and visible, " Prog. Quantum Electron. **26**, 287 (2002).

[98] https://www.gratinglab.com/Products/Product_Tables/Efficiency/Efficiency.aspx?print=true&efficiency=1410.

[99] C. Y. Kuo, "The study of high-speed ultra-broadband Ti:sapphire crystal fiber based wavelength swept laser," Master Thesis, National Taiwan University, Taiwan (2020).

[100] G. P. Agrawal and N. K. Dutta, Semiconductor Lasers, 2nd ed. (Van Nostrand Reinhold, New York, 1993).

`

doi:10.6342/NTU202203086

[101] B. E. A. Saleh and M. C. Teich, “Fundamentals of Photonics,” 1st ed, Hoboken, NJ: John Wiley & Sons, Inc., 438 (1991).

[102] K. J. Weingarten, B. Braun, and U. Keller, “In situ small-signal gain of solid-state lasers determined from relaxation oscillation frequency measurements,” Opt. Lett. **19**, 1140 (1994).

[103] A. Riveiro , F. Quintero, M. Boutinguiza, J. del Val, R. Comesaña, F. Lusquiños, and J. Pou, “Laser cutting: A Review on the influence of assist gas,” Materials, **12**, 157 (2019).

[104] S. M. Moore, and D. L. Chaob, “Application of subthreshold laser therapy in retinal diseases: a review,” Expert Rev. Ophthalmol., **13**, 311 (2018).

[105] G. Song, E. T. Jelly, K. K. Chu, W. Y. Kendall, and A. Wax, “A review of low-cost and portable optical coherence tomography,” Prog. Biomed. Eng., **3,** 032002 (2021).

doi:10.6342/NTU202203086

Appendix

A. Ti:sapphire Fiber-ring Laser with SMF-28e Optical Fiber

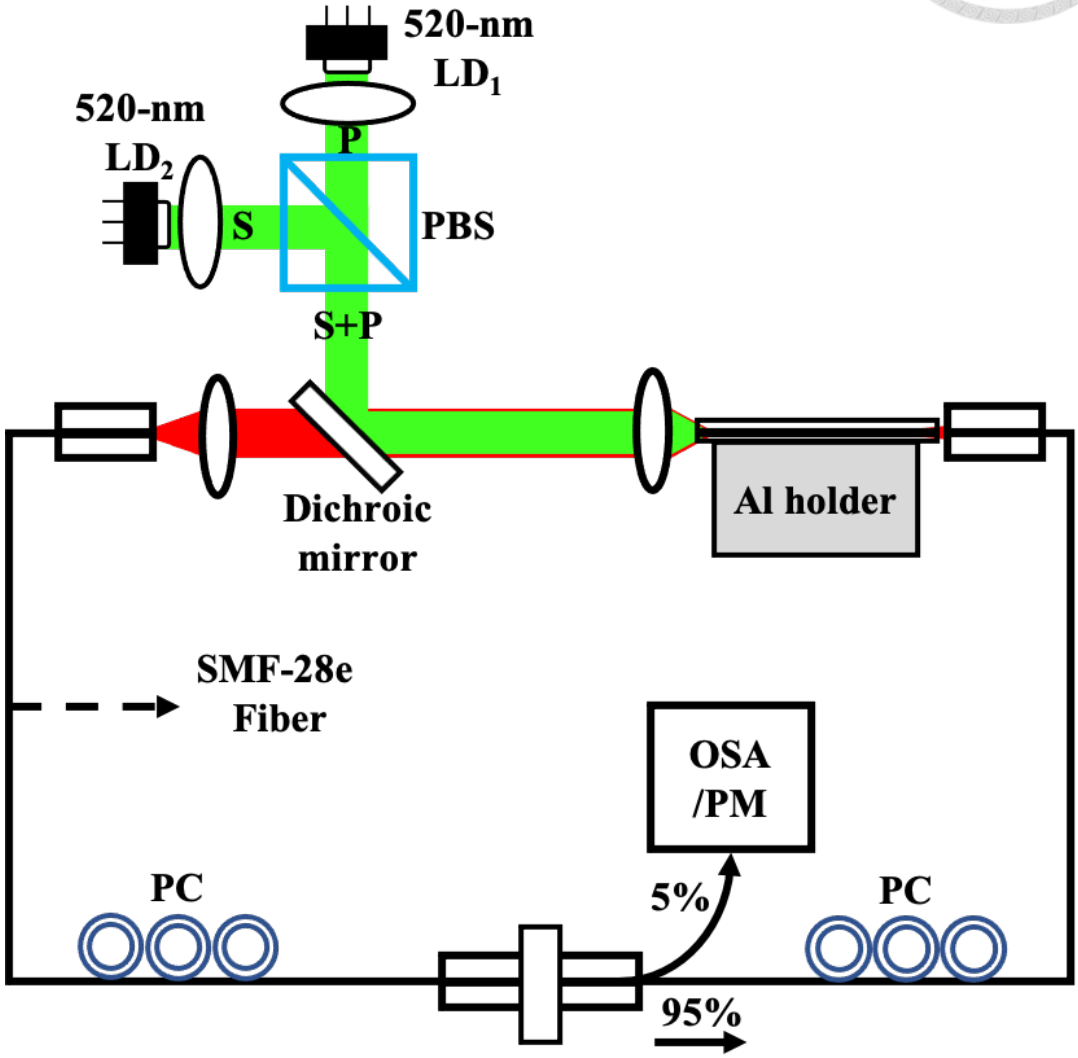

Schematic of Ti:sapphire fiber-ring laser with SMF-28e fibers. PBS: polarizing beamsplitter. PM: power meter; OSA: optical spectrum analyzer. PC: polarization controller.

doi:10.6342/NTU202203086

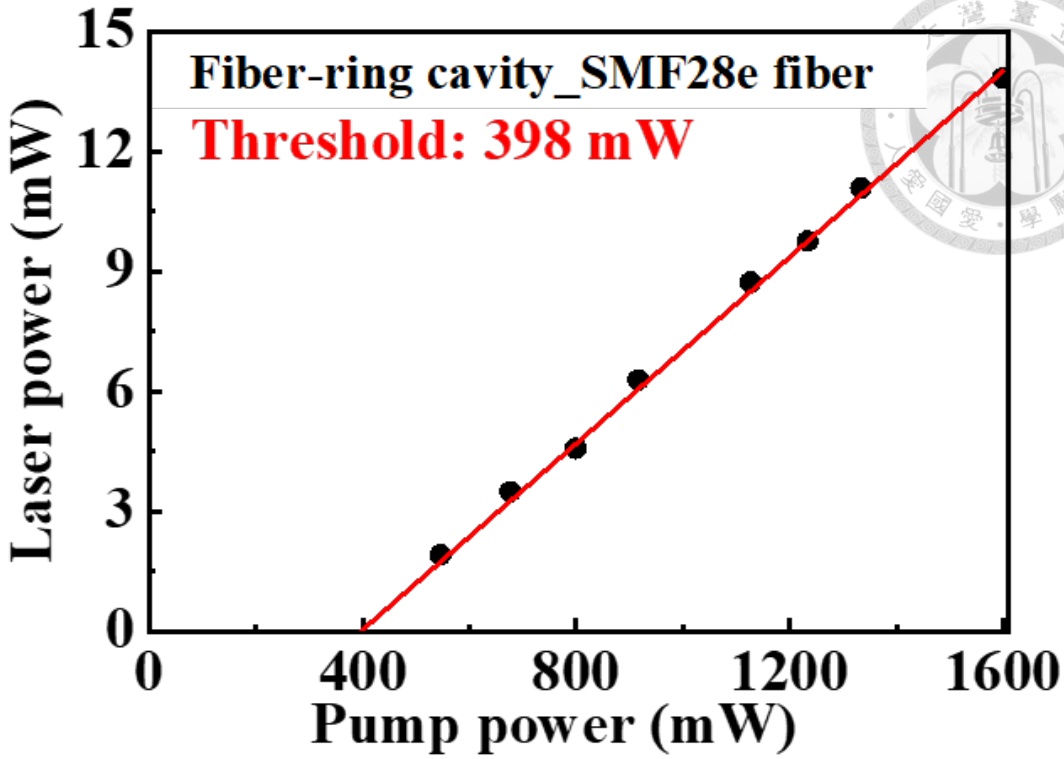

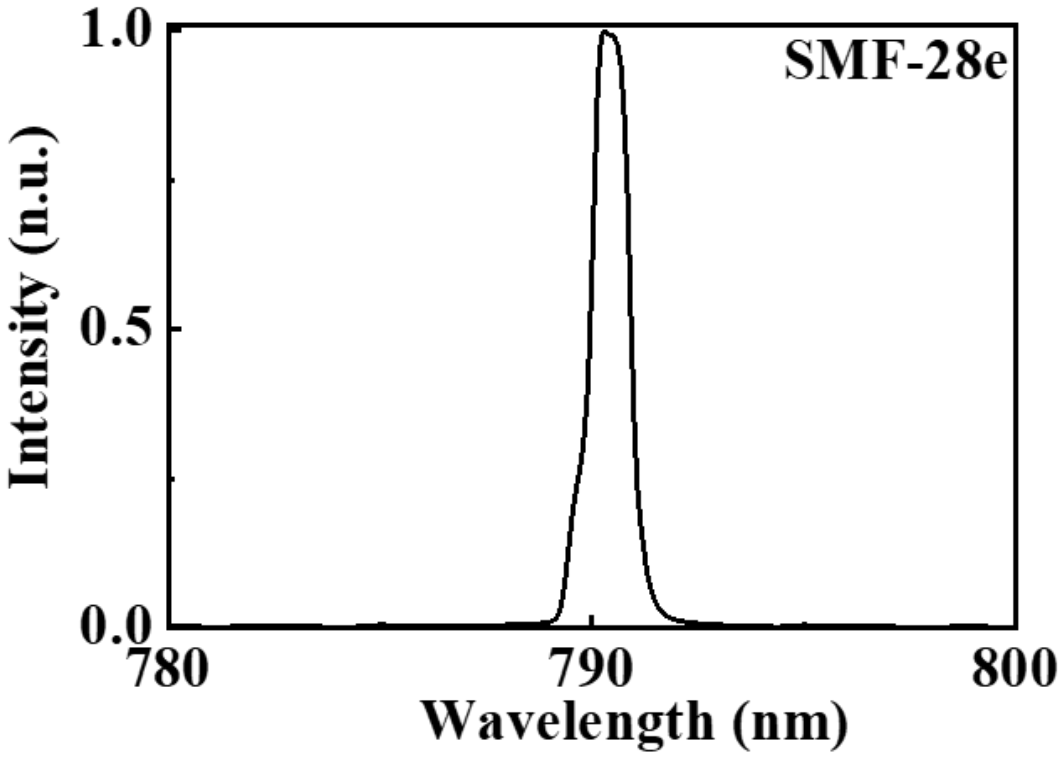

doi:10.6342/NTU202203086

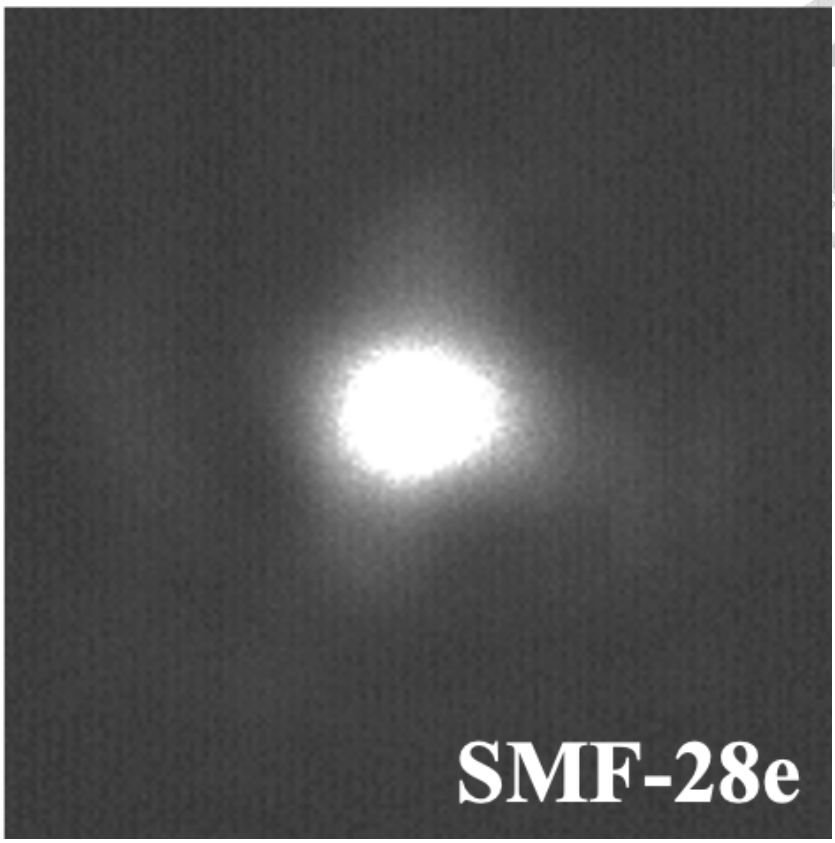

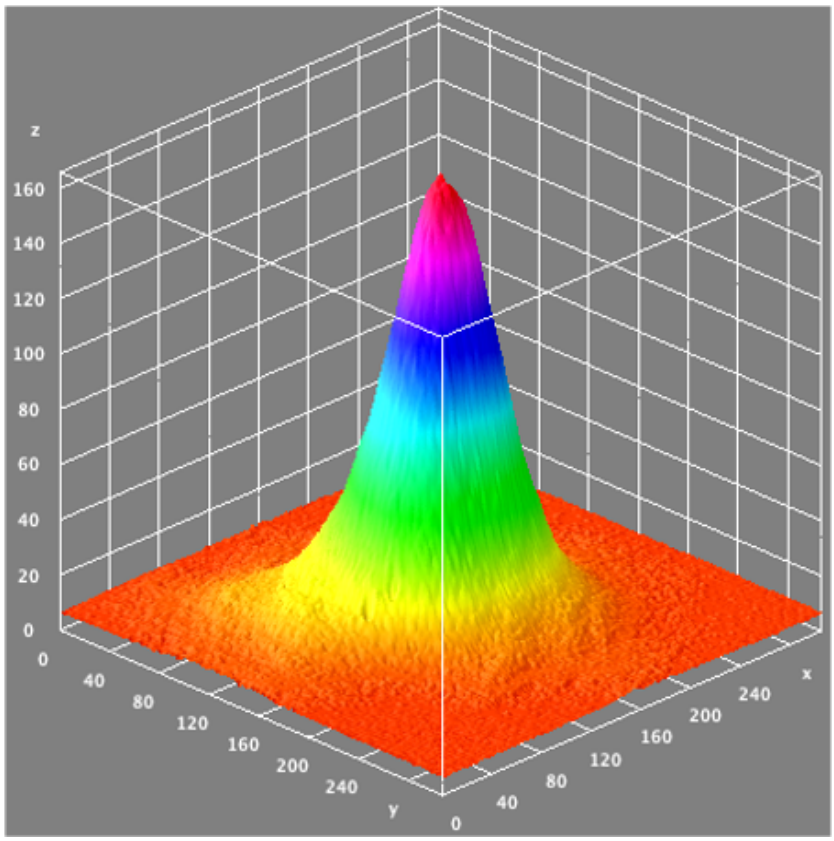

doi:10.6342/NTU202203086

B. Ti:sapphire Fiber-ring Laser with 780HP Optical Fiber

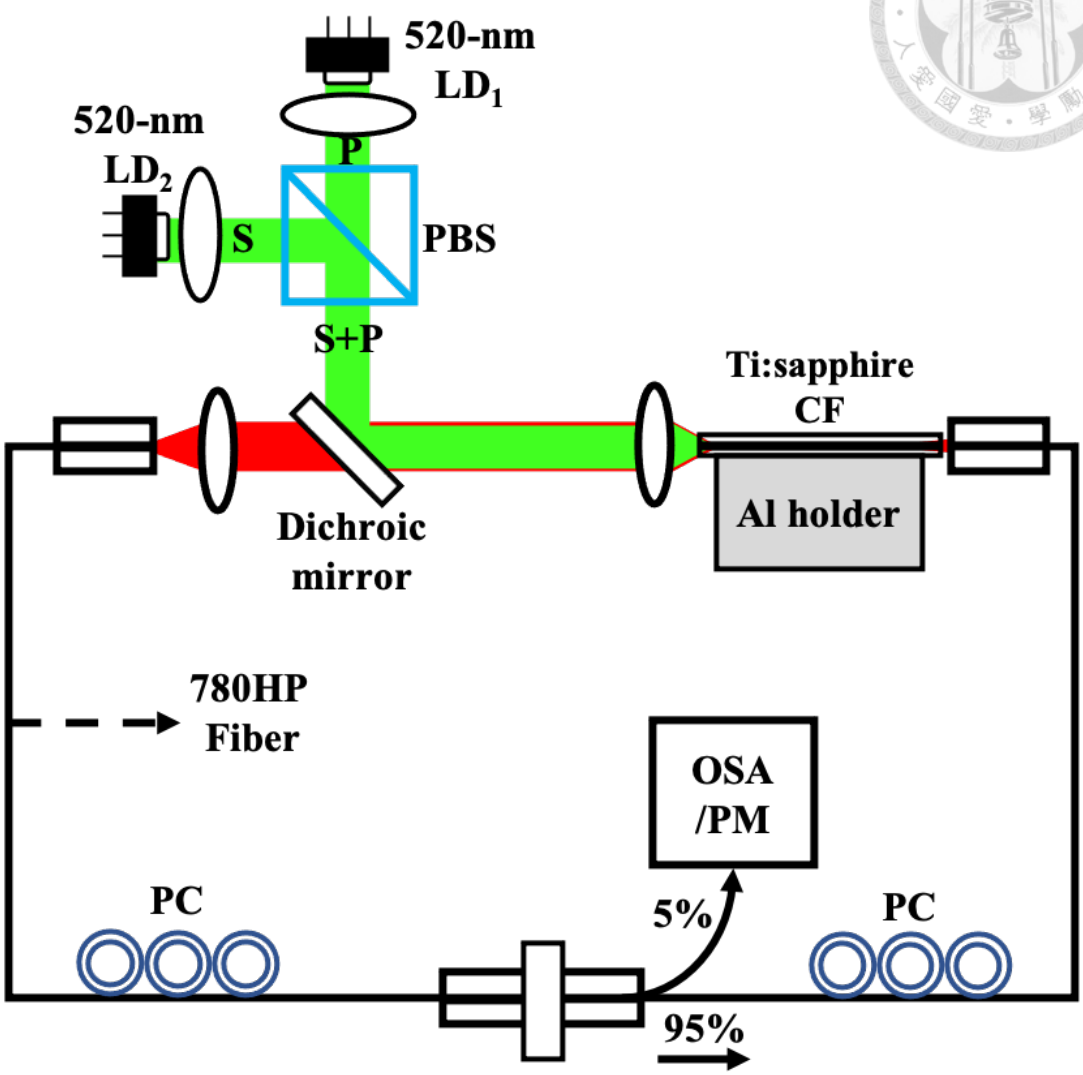

Schematic of Ti:sapphire fiber-ring laser with 780HP fibers. PBS: polarizing beamsplitter. PM: power meter; OSA: optical spectrum analyzer. PC: polarization controller.

doi:10.6342/NTU202203086

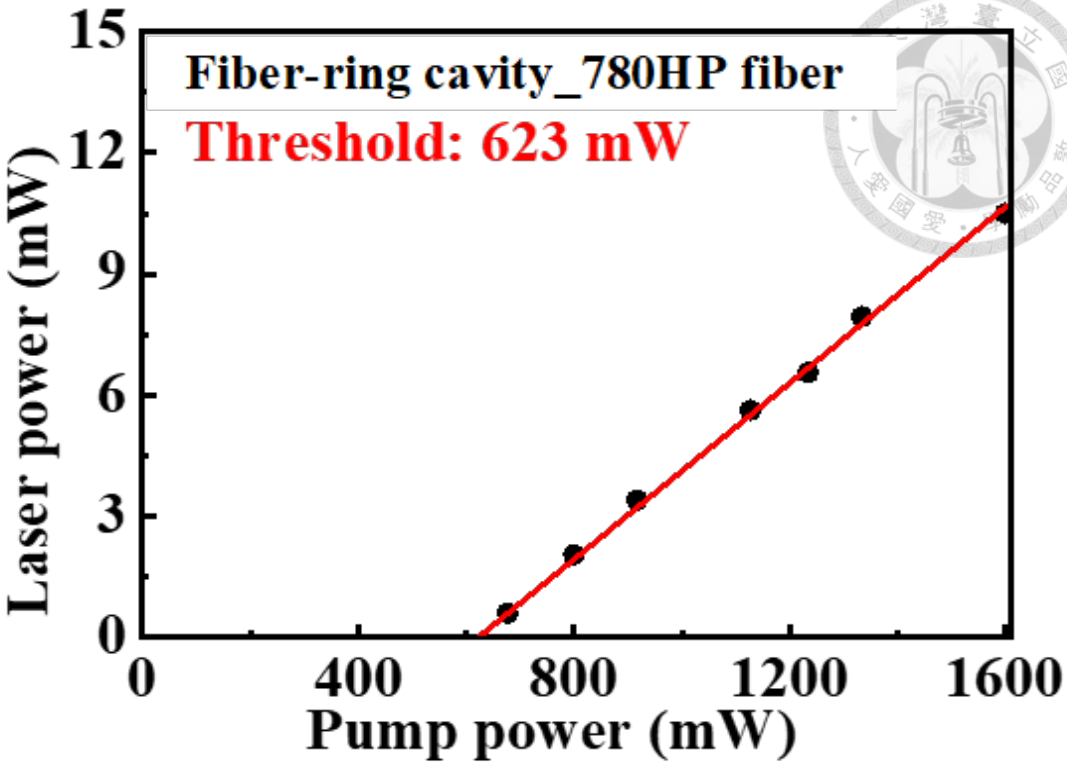

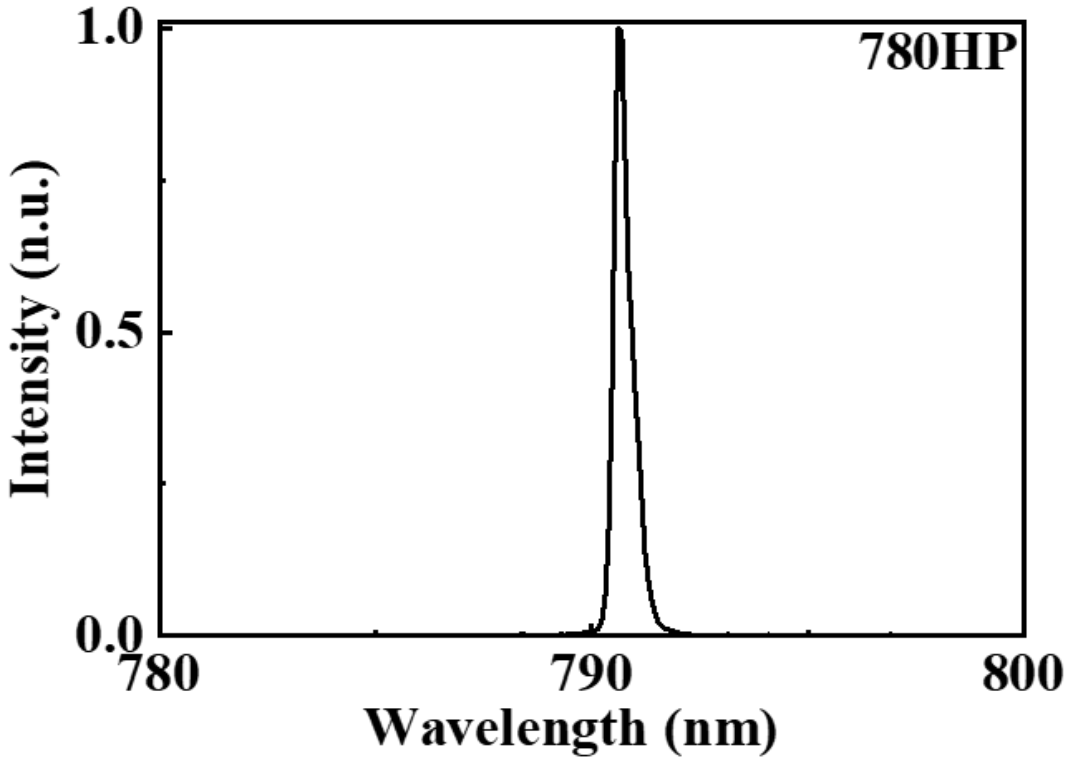

doi:10.6342/NTU202203086

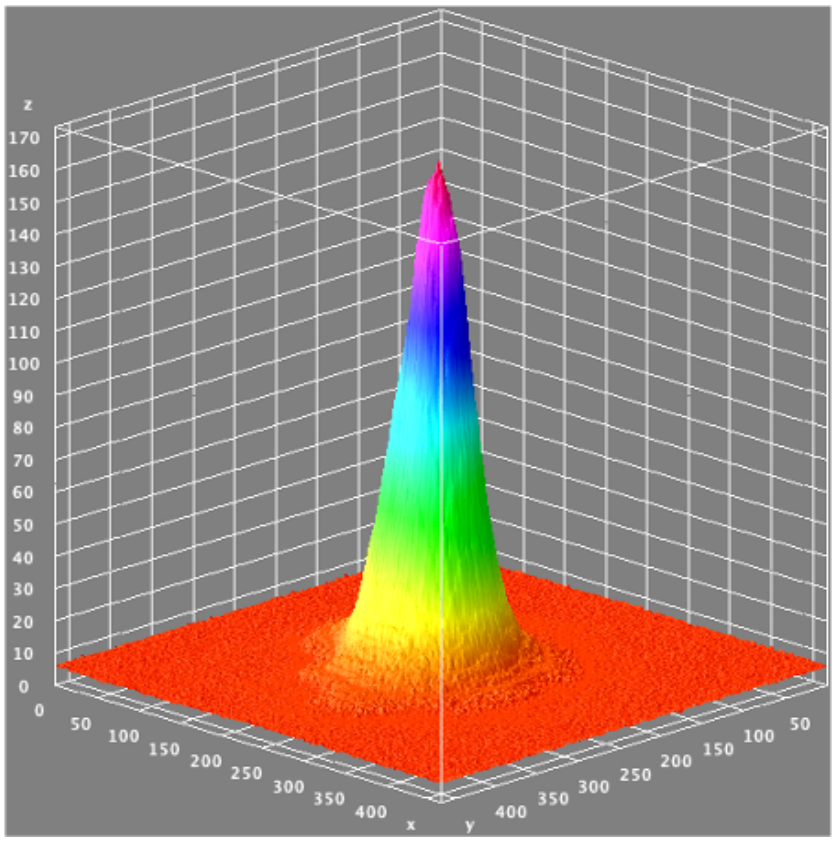

doi:10.6342/NTU202203086